TAMPEREEN TEKNILLINEN YLIOPISTO
TAMPERE UNIVERSITY OF TECHNOLOGY

MADAN PATNAMSETTY

ANNEALING TREATMENTS AND HIGH STRAIN RATE TESTING OF HIGH ENTROPY ALLOYS

Master of Science thesis

Examiners: Assoc. Prof. PASI PUERA and University Lecturer Dr. MIKKO HOKKA
Examiner and topic approved by the
Faculty Council of the Faculty of ENGINEERING AND NATURAL SCIENCES

on 23rd November 2016

ABSTRACT

MADAN PATNAMSETTY: Annealing treatments and High strain rate testing of High Entropy Alloys
Tampere University of Technology
Master of Science Thesis, 91 pages,
23rd November 2016
Master's Degree Program in Material Science Engineering
Major: Metallic and Ceramic Materials
Examiners: Professor Pasi Peura and University lecturer Mr. Mikko Hokka

Keywords: High Entropy Alloys, Annealing, High Strain-Sate Testing, Thermodynamics, Phases, Corrosion, X-ray Diffraction, Energy Dispersion Spectroscopy, Scanning Electron Microscopy

High Entropy alloys (HEAs) are a new class of materials that are referred as the resurgence of physical metallurgy in the materials research. The properties generated by these unconventional compositions are astonishing, which could potentially replicate many materials in the industrial applications. The main motto of this thesis is to study the properties of two different HEAs after annealing treatments and high strain rate testing.

The theoretical description of the four core effects, properties and a detailed description of thermodynamics influencing the phase formation of HEAs are included in the theory. The annealing treatment of the induction melted $Al_{0.5}CoCrCuFeNi$ and $Al_{0.5}CoCrCuFeNiMo_{0.25}$ HEAs was carried out. The annealing treatments included quenching and normalizing in the furnace. The microstructural characterization was done by using the optical microscopy and scanning electron microscopy (SEM). Additionally, elemental mapping was done by EDS and phase recognition was done by X-ray diffraction. The high strain rate properties were investigated for the induction melted samples and an arc melted $Al_{0.5}CoCrCuFeNi$ HEA sample (received from high entropy alloy research group, Chalmers university of technology), which was the reference material for comparison of properties. The technique used was Hopkinson split bar (HSB) compression testing. Finally, the corrosion tests were done in diluted acidic medium in comparison with TWIP steel to check the passivation.

The Optical microscopy, SEM and EDS had given a brief idea about the phases formed in the induction melted $Al_{0.5}CoCrCuFeNiMo_{0.25}$ and $Al_{0.5}CoCrCuFeNi$ HEAs. The comparison of $Al_{0.5}CoCrCuFeNi$ HEA with arc furnace casted $Al_{0.5}CoCrCuFeNi$ reference sample has shown new phases. The annealing treatment was done for 3 days for each induction furnace casted sample. These samples were subsequently quenched or cooled (normalizing). The annealed alloys were inspected with SEM and also elemental distribution was analyzed to confirm the presence of different phases. The final confirmation of phases was done with X-ray diffraction measurements. The $Al_{0.5}CoCrCuFeNi$ had formed totally different phases compared to reference material due to inclusions. The $Al_{0.5}CoCrCuFeNiMo_{0.25}$ had formed a copper rich and molybdenum rich phases with minor amount of inclusions or amorphous precipitates. This molybdenum addition had increased the hardness. High strain rate testing proved that $Al_{0.5}CoCrCuFeNiMo_{0.25}$ is ductile, whereas $Al_{0.5}CoCrCuFeNi$ (induction cast) is very brittle because of new phase formation. The corrosion tests of $Al_{0.5}CoCrCuFeNiMo_{0.25}$ proved that it is more noble than the reference TWIP steel sample in acidic aqueous solution.

PREFACE

This project was carried at the Department of Material Science of Tampere University of Technology during 2016. I am very grateful for the research and thesis work carried during this time. It was very exciting for me to think about thermodynamics and play with new format of alloy designs.

Firstly, I would like to present my strong gratitude and best regards to Professor Pasi Peura for proposing me this interesting research topic and giving me a change to accomplish my dreams in the field of material science research. Also, I would like to express my deepest gratitude to the University Lecturer, Dr. Mikko Hokka, for being my second examiner and guiding me to do mechanical testing of High Entropy Alloys.

A special regard to Professor Sheng Guo of High entropy alloys group, Chalmers University of Technology, Sweden, for providing me the reference sample.

Dr. Mari Honkanen deserves my greatest gratitude and respect for the most important help for the scanning electron microscope analysis and Mr. Jussi Laurila for corrosion experiments.

A special regard to the lab assistants Ms. Kati Mökkönen and Ms. Merja Ritola for supporting me without which I could not have done the experiments. Additionally, a special addressing to my fellow colleagues of my research group, Mr. Henri Järvinen and Ms. Minna Viinanen for helping during the experiments.

To all colleagues of my department who had supported me and had created a friendly environment which made me work with pleasure.

My deepest and strongest gratitude to my parents who had supported me and encouraged me throughout my life. Finally, to all my friends of Tampere who made me feel like a family.

Tampere 14.11.2016

MADAN PATNAMSETTY

CONTENTS

LIST OF FIGURES

LIST OF TABLES

LIST OF SYMBOLS AND ABBREVIATIONS

HEAs	High entropy alloys
BCC	Body Centered Cubic
FCC	Face Centered Cubic
BMGs	Bulk metallic glasses
LPE	lattice potential energy
XRD	X-ray diffraction
VEC	Valence electronic configuration
DR	Dendritic
IR	Inter-dendritic
FESEM	Field emission scanning electron microscope
EDS	Energy dispersive spectroscope
HSB	Hopkinson split bar

S	Entropy
H	Enthalpy
G	Gibb's free energy
k	Boltzmann constant
Ω	The number of ways in which energy is distributed among the particles
R	Gas constant
N_A	Avogadro's number
X_i	Atomic fraction of i^{th} elemental component
X_A	mole fraction of element A
X_B	mole fraction of element B
ΔS_{mix}	Mixing entropy
ΔS_{conf}	Configurational entropy
ΔS_{ther}	Thermal entropy
N	equi-atomic combinations
n	Total number of principle elements
C	number of components
F	degree of freedom
P	Number of Phases
A2	BCC structure of one (same) element at center and corner
B2	BCC structure with 2 elements at center and corner
r_i	atomic radius of i^{th} elemental component
ΔGmix	Gibb's free energy for mixing
ΔH_{mix}	mixing enthalpy
(ST)	total mixing entropy
δ	atomic size factor
Ω_{ij}	interaction parameter between i^{th} and j^{th} element
$(T_m)_i$	melting point of element i
ΔS_{IM}	entropy of formation of intermetallic compound
ΔH_{IM}	heat of formation of intermetallic phase
$k1^{cr}(T)$	criteria of intermetallic phase formation at temperature T

1. INTRODUCTION

From the ancient times, humans have tried to improve material properties for various applications. This led to the discovery of many metals. Alloying was an accidental discovery [1]. The base element(s) paradigm was the basic concept of alloy design. This was introduced since Bronze Age. The theme was, one or two elements are used as principal alloying elements, such as iron in steels or nickel in super alloys. The micro alloying of many elements is used in improving the alloy properties [2]. Several alloys were developed for various engineering applications for specific structural and mechanical properties [1].

Since the 1970s, the metal matrix composites and intermetallic compounds were considered as prime research topics. During this time, enhanced properties were observed with fine microstructure, improved solubility, or amorphous phases [3]. A new group of alloying elements was produced at California Institute of Technology by research group of Pol Duwez. In this process the liquid state of alloys were cooled at a rate of 10^6 K/s producing glass like structure to avoid the crystallization mechanism [1]. But this alloy design of multiple alloying elements was based on principal element(s). In 2004 a novel paradigm of alloy design was developed which involves mixing of multiple elements in nearly equimolar composition. These multi-component alloy systems were named after 'High Entropy alloys' (HEAs). The name was coined by Yeh et al [3]. This is because the larger number of components as principal elements produces solid solutions. The solid solutions with many elements will tend to be more stable due to larger mixing entropy (ΔS_{mix}) in which the configurational entropy (ΔS_{conf}) is the major part. The invention of HEAs has been referred as "renaissance in physical metallurgy"[4] based on the new dimensions of alloy designs. There are many reported HEAs which have exciting properties such as high strength and toughness, good wear/corrosion resistance, high thermal stability, and special electrical or magnetic properties. These are worth mentioning because many are achieved without careful optimization of composition and/or microstructures [5]

The high entropy alloys are considered as a new class of metallic alloy systems with the unique properties, which had raised interest in basic sciences and applications. HEAs can be potentially used for advanced or structural applications. However, there are many studies for different mechanical behaviors at different temperatures. The current study focuses on annealing and high strain rate deformation behaviors of HEAs (casted in induction furnace) $Al_{0,5}CoCrCuFeNi$ (HEA1) and $Al_{0,5}CoCrCuFeNiMo_{0,25}$ (HEA2) comparing with arc melted sample $Al_{0,5}CoCrCuFeNi$ (received from High entropy alloy research group, Chalmers University of Technology).

The annealing treatment gives an idea about the phase stabilities or formation of equilibrium phases. The annealing tests are performed to know the influence of thermodynamic factors such as entropy and enthalpy on the phase formation. Since the alloys were cast in induction furnace the effect of impurities are also studied.

The micro-mechanisms of plastic deformations are known to be strain-rate dependent. Thus the high strain rate plastic deformation behavior is critical to for structural and high strength applications [6]. The scope of the high strain rate testing is to see the deformation mechanism and thus to know the probability of twin formation. The change in yield strengths of induction melted samples are compared with arc melted reference sample. Microstructural changes of the deformed sample are studied.

Molybdenum is added as one of alloying element for the future research on wear properties and high temperature applications. The addition of molybdenum as alloying element inhibits the copper segregation and also forms a molybdenum rich phase which increases the yield strength and compressive fracture strength [7].

2. THEORITICAL BACKGROUND

High Entropy Alloys (HEAs) is an innovative topic which has many prospective applications. In 1788 the first form of multi component equi-mass alloys was studies by a German scientist Franz Karl Archard, which was later brought to light in 1963 by Professor Cyril Stanley Smith et al [1]. Later in 1981 the first work on exploring this great field was done by Brian Cantor of United Kingdom. J.W. Yeh et al in the year of 1995 independently started research about multicomponent alloys and finally in the year of 2004. Yeh introduced the concept of HEAs based on the mixing entropy factor which influenced by the increase of configurational entropy and decrease in number of phases, and thus render unique properties [1], [3]. However according to Ranganath et al. [8] there have been proofs that ancient Indian metallurgists had produced 'panchaloha' and 'asta dhatu' (alloys of 5 and 8 elements respectively) of unparalleled accuracy by becoming skilled at wax casting [8], but they may not be called as high entropy alloys due to nonmatching the criteria of HEAs definition as mentioned in section 2.1.

2.1 The Concept of HEAs

For the alloy designing a small portion of corners of the phase diagram was concentrated by most of the researchers, as illustrated in Figure 2.1 [9], but the HEAs arrival had shifted the research focus to center area. For the conventional alloys using base elemental approach, only n different base elements can give rise to 'n' types of alloys. However, if 'p' elements were selected from n base elements to make equiatomic alloys (p = 2, 3, 4, 5…., n), the possibility of number of equiatomic alloys (N) is increased from n to $N = 2^n - n - 1$. When n < 3 the probability will not hold good as seen in Figure 2.1, from Figure 2.1 it can be seen that the total number of equiatomic compositions are increased with increase in total number of principal elements.

2.1.1 Configuration or Mixing Entropy

The relation between degree of mixing or randomness and entropy of a system can be known from Boltzmann's equation

$$S = k \ln \Omega \tag{2.1}$$

Where S is entropy, k is Boltzmann constant and Ω is number of ways in which energy is distributed among the particles [10].

The total entropy of a system is simply the sum of thermal entropy ΔS_{ther} and configurational entropy ΔS_{conf}. The entropy is

$$\Delta S_{total} = \Delta S_{conf} + \Delta S_{ther} \tag{2.2}$$

ΔS_{ther} arises due to total number of ways in which the components share the thermal energy. ΔS_{conf} arises with respect to the number of ways in which the particles are arranged [10].

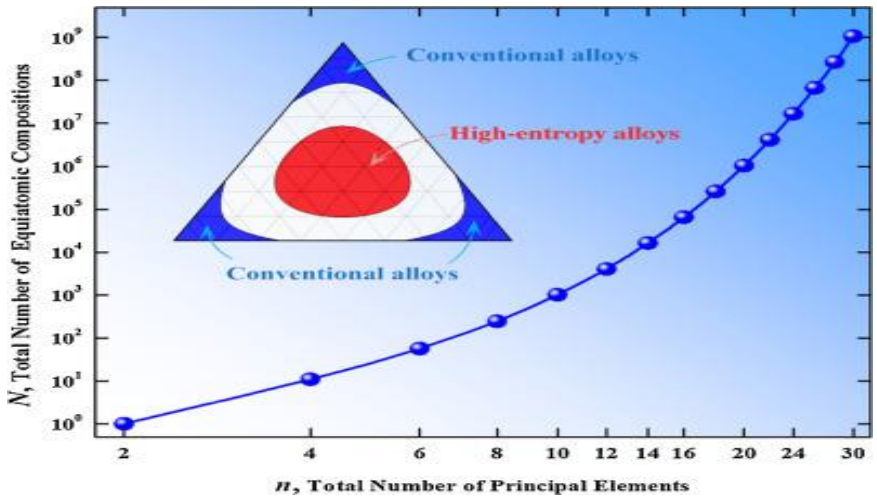

Figure 1. *The critical area for design of conventional alloys and high-entropy alloys on a ternary phase diagram is shown in the inset. The exponential raise of equiatomic combinations (N) Vs total number of principle elements (n)* [9].

Considering a binary alloy system with n_a as atoms of 'A' element and n_b as atoms of 'B' element, the configurational entropy after mixing can be defined as [3, 6]

$$\Delta S_{conf} = k \ln \frac{(n_a+n_b)!}{n_a! n_b!} \tag{2.3}$$

By substituting the relation in equation (2.3)

$$R = k N_A \tag{2.4}$$

(Where R is the gas constant and N_A is Avogadro's number) we get configurational entropy in terms of mole fractions.

Thus the relation of configuration entropy converts to

$$\Delta S_{conf} = -R(X_A \ln X_A + X_B \ln X_B) \tag{2.5}$$

Where X_A is the mole fraction of element A and X_B is the mole fraction of element B, from the equation 2.5 the maximum configurational entropy is possible only at equal atomic quantities, where the mole fractions must be equal.

The configurational entropy had another name which could be called as mixing entropy, so by definition $\Delta S_{conf} = \Delta S_{mix}$ (mixing entropy). Thus the mixing entropy of the multi component system per mole could be expressed as

$$\Delta S_{mix} = -R \sum_{i=1}^{n} X_i \ln X_i \quad (2.6)$$

Where X_i is the mole fraction of i^{th} element for 'n' number of elements.

The Gibb's free energy of mixing can be express as

$$\Delta G_{mix} = \Delta H_{mix} - T\Delta S_{mix} \quad (2.7)$$

Where ΔG_{mix} is Gibb's free energy for mixing and ΔH_{mix} is mixing enthalpy, so the equation shows that increase in mixing entropy will decrease the free energy value, which means the alloy system becomes more stable.

2.1.2 Definition of HEAs

The standard definition of HEA is an alloy with minimum of five principal metallic elements, each with atomic concentration between 5 - 35 atomic percent [9], [11]–[13]. When the mixing entropy is increased, the randomness or disorder solid solutions remain stable compared to ordered intermetallic compounds [13]. This started the interest in designing of alloys with high entropy.

By substituting the mole fraction values for equi-molar alloys with 3, 5, 6, 9 constituent elements in Equation (2.6), the mixing entropy value arrives at 1.1R, 1.61R, 1.79R, 2.2R respectively [3]. By Richard's rule [10] which states that "the entropy of fusion is a constant for metals and nearly equal to 2.2 cal K^{-1} mol^{-1}, which shows the relationship between the entropy of fusion and the phase transition for most of metals"[14] , the entropy changes in fusion of metals. This is equal to 'R' value at their melting point. So comparably the mixing entropy value is increased to 1.1R with 3 alloying elements of equal quantity. Thus the mixing entropy value increases for equi-molar alloys with simply increasing number of components [3], [9]. Additionally, some factors like vibrational, electronic and magnetic randomness increases the entropy values compared to the theoretical mixing entropy. This consequently decreases the ordering and segregation with increase in principal elements and increases the stability of alloy system [3].

A second definition is a classified concept, which states that the HEAs are having mixing entropy greater than or equal to 1.5R in a random solution (no need to be equiatomic). This can be calculated by equation (2.6). The classification is illustrated as given in Figure 2 [1], [3].

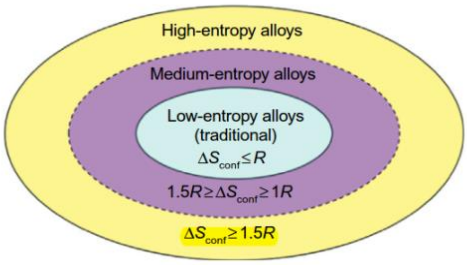

Figure 2. *Classification of alloys based on entropy value* [1]

2.2 Core Effects

The variation in properties of HEAs from conventional alloys is due to the complex compositions with equi-molar masses of each component [15]. Yeh et al [15] has explained about four core effects, which show the unique properties of HEAs. Figure 3 shows the core effects with respect to physical metallurgy.

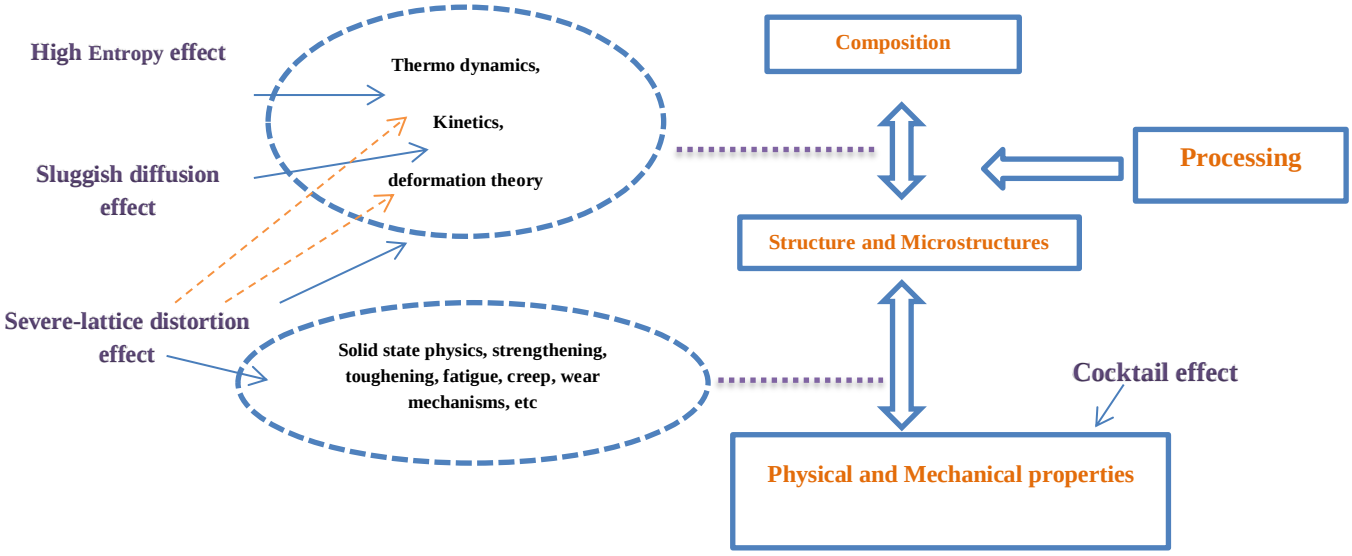

Figure 3. *Physical Metallurgy of HEAs* [16]

From the Figure 3 it is clear that high entropy effects depend on thermodynamics. The sluggish diffusion depends on kinetics of diffusion. The lattice severe distortion not only effects the deformation of the structure, but also slightly effects kinetics and thermodynamics. Finally the physical and mechanical properties effects the cocktail effect [16]. Thus every property and physical metallurgy of HEAs is dependent on these core effects. These effects also influence every alloy, but the complex composition of the HEAs had a greater effect on these factors which influenced the properties and phase formation. The exclusive properties of HEAs are define using core effects. These effects are discussed in detailed below.

2.2.1 High entropy effect

The high entropy effect improves the tendency of multi-element solid solution phases. This effect is very important in order to avoid the intermetallic compound formation. Otherwise, the microstructure with intermetallic phases would become brittle and can't be controlled. This effect reduces the intermetallic compound formation even at low temperature [16]. According to Gibb's phase rule, at equilibrium the number of phases (P) at constant pressure for a given alloy is

$$P = C + 1 - F \tag{2.8}$$

Where C is number of components and F is degree of freedom in the system [10]. For a 6 component system there exist maximum of 7 equilibrium phases at an invariant reaction (eg: eutectoid, eutectic…. etc. reactions). The HEAs form solid solution phases instead of intermetallic phases, but only certain multi-component equi-molar compositions form HEAs with multi-principal solid solutions instead of intermetallic compounds [15].

Basically a solid solution (alloy), has a solute which is dominant and minor additions of other elements. But in case of HEAs it is complicated to differentiate between solute and solvent. According to many researchers, in HEAs the solid solutions are defined as 'multi-principal-element-solid solutions' which can form simple phases of Body Centered Cubic (BCC) and Face Centered Cubic (FCC). The number of phases formed are very less compared to the maximum phases formed by Gibb's phase rules (equation 2.8). This also infers that high entropy effect increases the solubility limit [15].

By thermodynamic laws, the entropy of mixing of a phase could be related to mixing enthalpy as in the Equation 2.7. The equilibrium state has the lowest free energy of mixing according to the second law of thermodynamics. The enthalpy of mixing ΔH_{mix} has an influence in the Gibb's free energy. The smaller difference in mixing enthalpies of unlike atomic pairs such as CoCrFeMnNi or Refractory HfNbTaTiZr HEAs can form simple FCC and BCC phases respectively [1].

Conversely, if there is a larger difference in the enthalpies(ΔH_{mix}) there might be two phases generated. For example, the aluminum addition in CoCrCuFeNi-HEA forms multi-component FCC and multi-component BCC (A2) at high temperatures (nearly 600^0C). Additionally, the same HEA has precipitates of B2 in copper-rich FCC and spinodally decomposed A2 and B2 phases from A2 phase during cooling. The HEAs have some intermediate phases because of the equi-molar mass of each component and the high mixing enthalpy values. Overall, the Gibb's free energy of mixing is lowered to form stable state multi principal solid solutions [1]. It is suggested that addition of significant amount of aluminum, titanium, and /or copper almost always results in the formation of more than one phase[17]–[19].

However, in a recent review [20] it was suggested that there is a little evidence of the entropic stabilization showing a comprehensive effect on the microstructural stability. It can be shown that in rare cases that the HEAs can be stable single phase solid solutions, such as an initial report suggested that $Al_{0,5}CrCoCuFeNi$ was a single phase (FCC) solid solution.

The annealing studies on $Al_{0,5}CrCoCuFeNi$ has shown formation of multiple phases including intermetallic phases at like Ni-Al-based B2, Ni-Al-L12 and Cr-Co-Fe-based σ precipitates. [21]. This shows that enthalpy is more significant in phases/intermetallic compound formation when compared to entropy in some conditions.

Atomic size factor also influences the mixing enthalpy and mixing free energy which is explained in Chapter 2.3.

2.2.2 Sluggish diffusion effect

The diffusion and phase transformation kinetics are slow in HEAs compared to conventional alloys, because of two main reasons. Firstly, in HEAs the neighboring atomic sizes are different. Thus the diffusion mechanism of atoms into vacancies is different [9]. The HEAs have slower diffusion rate and higher activation energy due to larger fluctuation of lattice potential energy (LPE) between lattice sites [22]. The abundance in low – LPE sites restrict the diffusion of atoms [10]. This leads to the sluggish diffusion in HEAs. In diffusion couple experiment by Tsai et al [22], it is shown that the activation energy of diffusion in CoCrFeMnNi alloy is higher compared to other ternary alloys (Fe-Cr-Ni) and pure metals such as Co, Ni, γ-Fe. From Figure 4 it is shown that the diffusivity of Ni at melting temperature of the respective ternary alloys and pure metals is greater compared to CoCrFeMnNi alloy. This is because of LPE difference from one lattice site to another such as from L to M as mentioned [1], [9], [22].

Secondly, the diffusion rate is different for different components (elements) in the HEAs. So, there is lower success rate of jumping of an atom into vacancies of other elements. However, a new phase formation requires redistribution of all elements to meet the target composition. Grain growth also requires the diffusional coordination of all elements. So, the slow diffusing elements become rate controlling factors which hamper the transformation [9].

In comparison with other core effects, sluggish diffusion is very important due to its structural stability over a high temperature range and formation of nanostructures, which makes it more demanding for applications based on low diffusion kinetics [22]. It has also been observed in the reference [20] that some HEAs show recrystallization resistance, which is a clear indication of sluggish diffusion kinetics. But in reality the presence of dislocations greater than the grain sizes increases the rate of diffusion, and presence of second phases or inhomogeneities increase or decrease the rate of diffusion. Thus it is

evident that the presence of inhomogeneities affect the rate of atomic diffusion. So HEAs are unlikely to be anomalously slow. The proof is shown in Figure 5, where the activation energy is considerably high in HEAs when compared to normal alloys.

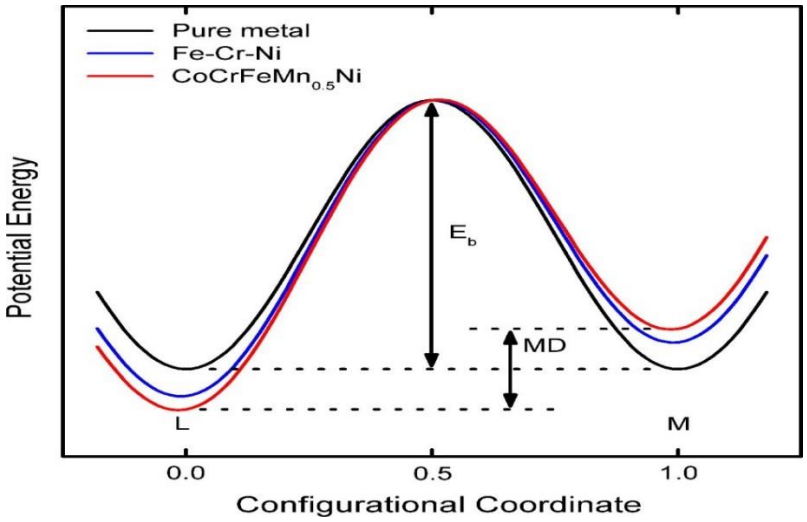

Figure 4. *The Lattice potential energy difference of Ni atom during diffusion along pure metal, Fe-Cr-Ni alloy, CoCrFeMnNi HEA from L to M* [22]

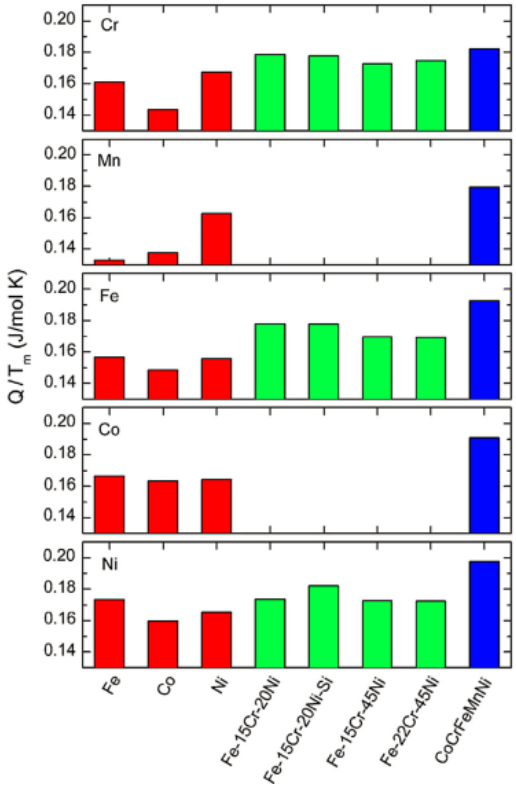

Figure 5. *Normalized activation energies of diffusion for Cr, Mn, Fe Co and Ni in different matrices* [22]

2.2.3 Severe lattice-distortion effect

Normally for the traditional alloys the severe lattice-distortion effect is compared with dominant alloys (one or two alloys), but in HEAs every element has same probability to occupy the lattice site. Here each alloying element is varied, with different sizes. Thus we can see lattice distortion effect [15]. Yeh et al. [23] in his study of X-Ray diffraction analysis of 'AlCoCrCuNiFeSi' HEAs showed that the intensities had dropped compared to less component alloying elements.

There were mainly two factors affecting the decrease in X-ray diffraction (XRD) intensities. Firstly, the temperature effect which relates to the vibrational amplitude of the atoms, where the atoms deviate from the rest position due to increase in temperature [23]. Secondly, the intrinsic lattice distortion effect which is caused by the addition of multiple components [15]. Figure 6 shows the relative changes in diffraction angles with respect to incidence of X-ray beams over different atomic sites. Since, the crystal structures of roughened planes were distorted, the X-ray beams were scattered and thus the detected signals were weakened. The lattice distortion factor was formulated mathematically similar to thermal factor [23]. However, it should also be noted that influence on peak intensity and diffuse scattering in diffraction pattern includes crystallographic texture, thermal vibrations and fluorescence. Thus it is suggested that for a high quality data the experiments should be assessed attentively [20].

The lattice strain is increased due to increase in number of component alloys as described in Figure 7 [23]. Besides atomic size difference, we have bond energy differences and different crystal structures i.e. the non-symmetrical binding and electronic structure of the atoms, and the non-symmetrical variations which additionally cause lattice distortion [1]. A schematic illustration of strained lattices is shown in Figure 6d. [20]

Severe lattice-distortion explains the hardness and strength of HEAs. The HEAs with FCC are less hard (solution hardening) compared to BCC. The probable reason may be due to the coordination number of FCC (12) and BCC (8). This shows that FCC has smaller fraction of unlike atoms compared to BCC, thus FCC might have less lattice distortions compared to BCC. Similarly, the electrical and thermal conductivity are decreased due to phonon and electron scattering [1].

After many experimental evidences and prediction of results based on modelling, it has been seen that there is not much lattice distortion (greater than 5% of lattice parameter) as expected. There is however some uncertainty in manifestation of distortions from the diffraction data (X-ray diffraction). This topic needs a further detailed investigation [20].

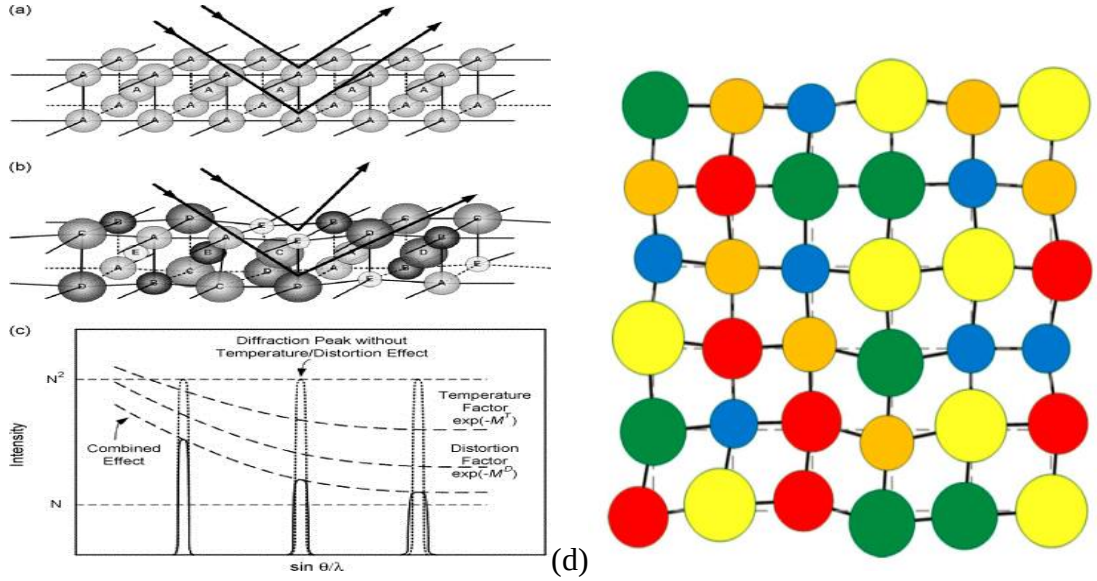

Figure 6. *Schematic illustration of intrinsic lattice distortion effect on Bragg diffraction: (a) perfect lattice with the same atoms; (b) distorted lattice with solid-solution of different-sized atoms which are expected to randomly distribute in the crystal lattice according to a statistical average probability of occupancy; (c) temperature and distortion effects on XRD intensity* [23] *.(d) The schematic representation of strained lattices* [20]

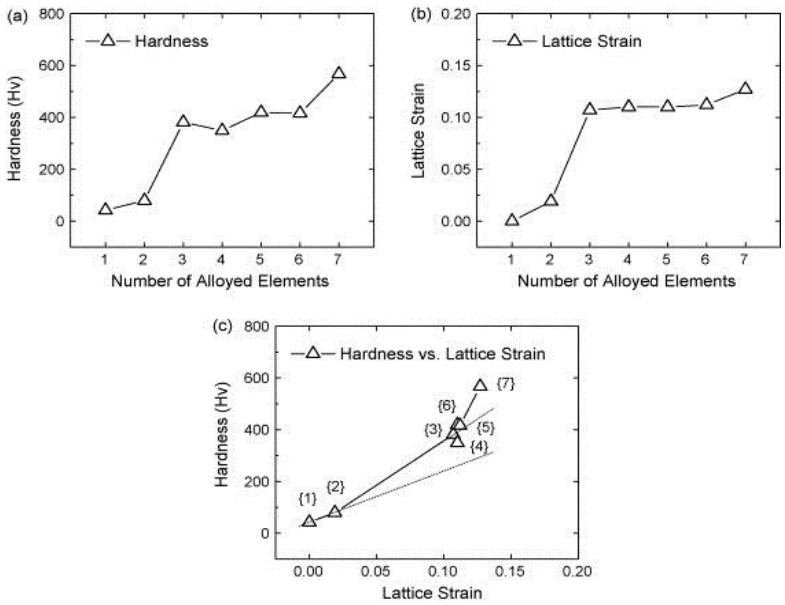

Figure 7. *Schematic illustration of hardness and lattice parameter with increase in alloying elements (a) Experimentally measured hardness and (b) theoretically predicted overall lattice strain of Cu–Ni–Al–Co–Cr–Fe–Si alloy series with increasing number of incorporated principal elements; (c) correlation of hardness vs. overall lattice strain of the alloy series (the quoted number {*n*} denotes the number of incorporated elements)* [23].

2.2.4 Cocktail effect

The mixing of many elements can give unexpected properties, which can't be achieved even by individual elements, this effect is known as 'Cocktail effect'. The effect was mentioned by Ranganathan et al [8], which was inferred by subsequent mechanical and physical properties. The cocktail effect is an overall contribution of component elements. This is in relation with individual phases formed inside the HEAs.

The phase size and shape, distribution, boundaries and their individual properties makes the overall effect. This is similar to the extraordinary properties of composites which are not possible by individual components. Thus HEAs can also be termed as composites ranging from atomic scale to multiphase scale [1].

Yeh introduced the 'cocktail effect' with $Al_xCoCrCuFeNi$ HEAs. The change in aluminum composition leads to the change in FCC to BCC with FCC + BCC as mix phases with particular aluminum concentrations [3]. As explained in reference [3] the increase in aluminum concentration increases the hardness as phase is changed from FCC to BCC. The hardness increased is explained in section 2.2.3 (lattice distortion effect). Figure 8 explains the increase in hardness values due to increase in Aluminum content and similarly increase in lattice constants of FCC and BCC phases in those particular compositions [3], [15]. In comparison with Figures 8 and 9, the hardness value in the FCC + BCC (two phase region) of in $CoNiCrAl_xFe$ (Cu free alloy) alloys has increased narrowly as aluminum concentration is increased. The copper stabilizes FCC phase (which is less hard) by forming isomorphous solid solution with nickel, and sometimes forms intermetallic compound with aluminum. This shows the cocktail effect due to variation in alloy compositions [15]. Some of the suggested properties from literature reviews by Yeh at el [1] and Lu et al [15] is lattice parameter which is a derivation from rule of mixture. An additional property might be increased wear resistance due to development of hard microstructure through precipitation.

However, it is not clear that this effect is the only property of HEAs, because the rule of mixture is applicable for many alloys and new properties are derived by alloying elements. Perhaps the best way to describe the cocktail effect is mentioning the surprising properties derived from HEAs due to their complex compositions [20].

2.3 Thermodynamics and Phase selections in HEAs

HEAs are also known as multicomponent alloys with equi-atomic or nearly equiatomic compositions. These compositions might end as solid solutions which includes partially ordered or random solid solutions, sometimes amorphous alloys are formed. Basically, we consider Hume-Rothery rules to control alloy behavior based on solubility factors which are influenced by atomic structure, crystal structure, valence and electronegativity.

These rules are mostly focused on binary alloy systems. There should be new rules to define the multicomponent solid solutions [1].

The alloy designing by Huang and Yeh in 1996 has a special set of alloying elements targeted to be mixed or designed. The selection of some chemically incompatible elements (Pb, Sn and Bi) was eliminated. Expensive rare elements and volatile elements were also deleted from designing. There were three categories of alloys tried, such as copper containing alloys as it has weaker bonding energy with some transition metals like chromium, iron and cobalt. Aluminum containing alloys as it has greater bonding energy with transition elements. Molybdenum containing alloys as it increases the Young's modulus value [1].

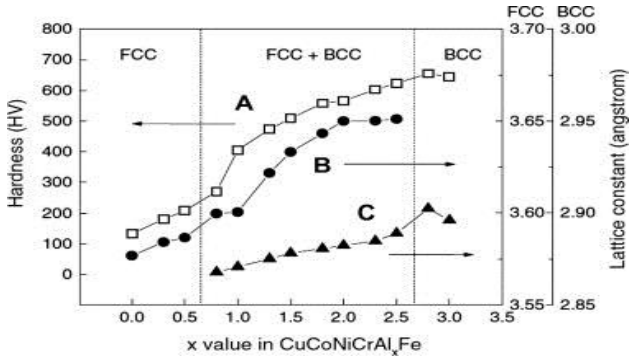

Figure 8. *Hardness and lattice constants of a CuCoNiCrAl$_x$Fe alloy system with different* x *values: (A) hardness of CuCoNiCrAl$_x$Fe alloys, (B) lattice constants of an FCC phase, (C) lattice constants of a BCC phase [3]*

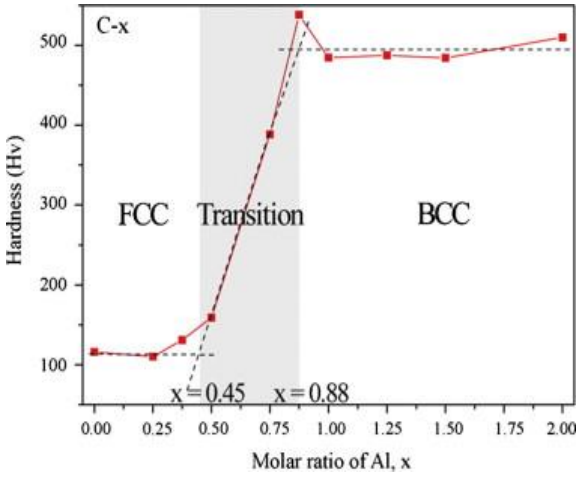

Figure 9.*Hardness of a CoNiCrAl$_x$Fe alloy system with different x values, the Cu-free alloy has lower hardness than that of the CuCoCrAl$_x$Fe alloy*[15]

From the study it was found that the high entropy effect was increasing the mixing probability of alloys [1]. Later studies found that not only entropy of mixing influences the formation of HEAs but some more parameters such as enthalpy of mixing and atomic size difference values also have an influence [2]. In an endeavor to know about conditions required to form Bulk Metallic Glasses (BMGs), Inoue (1996) had suggest empirical rules that a multicomponent alloy should have at least three elements, the mixing enthalpies of constituent elements should be negative and finally the atomic size difference should be greater than 12 %, which clearly are the inverse of Hume-Rothery rules. Among these rules about BMGs, the first rule of the multicomponent alloys is resembling the HEAs criteria. [1].

Ideally, the theory based assumptions of HEAs are explained through equation (2.6), for which all atoms are assumed to be identical in size and are loosely arranged. However, we know that in HEAs the atomic sizes vary. Therefore, the mixing entropy not only depends on chemical compositions but also depends on atomic size and packing density[2], [15]. According to the Mansoori et al. [24] theory in 1971 about thermodynamics of hard sphere system with different particles, the total entropy of mixing (S_T) is expressed as sum of configurational entropy (S_C) and excessive entropy of mixing (S_E) (which is a function of atomic composition X_i, atomic radius r_i and overall packing density ξ) [2], [25]. The expression is as follows

$$S_T(X_i, r_i, \xi) = S_{conf}(X_i, r_i, \xi) + S_E(X_i, r_i, \xi) \tag{2.11}$$

S_C is similar to equation 2.6 the configuration entropy of mixing (ΔS_{conf}) of an ideal solution. Normally S_E values are negative, thus the total mixing entropy S_T after considering S_E values is less than S_C values [2]. The excessive entropy value tends to zero with decrease in packing density, which hypothetically, infers that the increase in temperature tends S_E value to zero. This makes the configurational entropy ($S_C = \Delta S_{conf}$) equal to total mixing entropy (S_T). Thermodynamically, at a given temperature T, the entropic dominance for the stability of phases, the following criteria should be achieved.

$$|TS_T| \gg |H_{mix}| \tag{2.12}$$

Where H_{mix} is enthalpy of formation of phases. So considering the equations (2.11) and (2.12) we end with criterion for entropic dominance as (S_E is considered with negative sign as per above explanation)

$$\frac{|S_E|}{S_C} \ll 1 - \frac{|H_{mix}|}{TS_{conf}} \tag{2.12}$$

By above expressions it is clear that to match the original criteria of HEAs, inequality is satisfied by increase in temperature or increase in the configurational entropy (S_{Conf}). But the enthalpy is dependent on the phase which is defined after the casting of alloys, thus the enthalpy values also define the phase stability of the HEAs [25].

Zhang et al [15], [26] has proposed that, the phase stability of HEAs can be predicted by two additional parameters other than mixing entropy. They are atomic size factor (δ) and enthalpy of mixing (ΔH_{mix}). These factors are extracted from Hume-Rothery rules. The two parameters are defined as [2]

$$\delta\% = 100\% \sqrt{\sum_{i=1}^{n} X_i \left(1 - r_i \Big/ \left(\sum_j^N X_j r_j\right)\right)^2} \tag{2.9}$$

$$\Delta H_{mix} = \sum_{i=1, i\neq j}^{n} \Omega_{ij} X_i X_i = \sum_{i=1, i\neq j}^{n} 4\Delta H_{ij}^{mix} X_i X_j \tag{2.10}$$

Where ΔH_{ij}^{mix} is the mixing enthalpy of a binary of ith and jth elements with equi-atomic composition, r_j is the atomic radius of element j, X_i is the atomic fraction of element i, and Ω_{ij} is the interaction parameter between ith and jth element [2]. After collecting data of multicomponent systems, a graph is plotted with the values of δ vs ΔH_{mix} as shown in Figure 10.

From the Figure 10, it's clear that HEA generally tend to from single phased solid solutions at low mixing enthalpy and atomic size difference (delta), i.e. in the range of −15kJ/(mol. K) < ΔH_{mix} < 5 kJ/(mol. K) and 0 < δ < 5% [2]. Under the fulfillment of criteria of simple solid solutions with mixing entropy value greater than 1.5R, the simple solid formation is possible when ΔS_{mix}>13.38kJ/(mol.K), −15kJ/mol < ΔH_{mix} < 5 kJ/mol and δ < 5.

Zhang et al summarized from his results [26] that with further increase in δ (>8) and decrease in the negative ΔH_{mix} value (<−15 kJ), gives out amorphous phases, which is like the as-cast production of the Metallic glasses (shown as the blue region in Figure 2.9). Thus it is clear that mixing enthalpy and atomic size factor (δ) explains the HEAs properly than mixing entropy values[2], [15], [26].

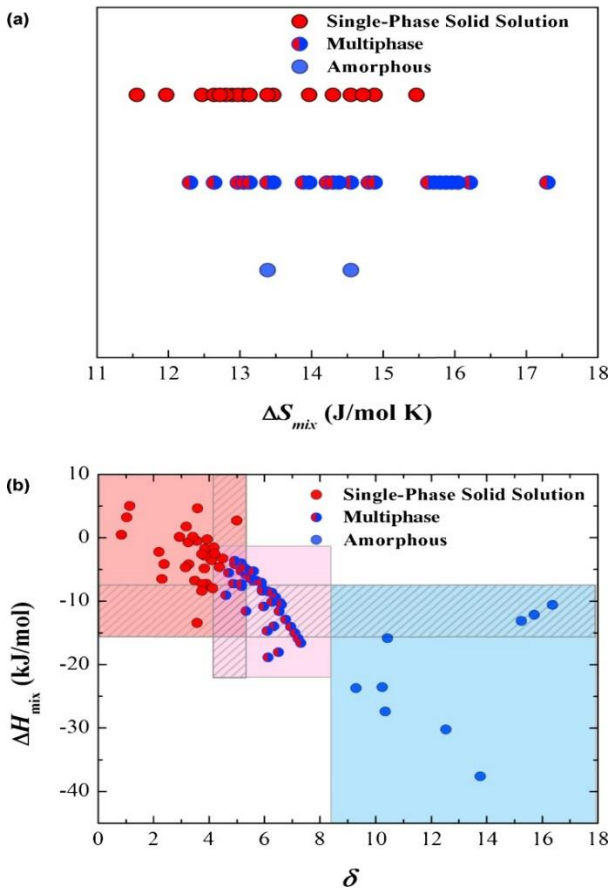

Figure 10. *A phase transformation map of as-cast HEAs based on mixing enthalpy ΔH_{mix} vs atomic size difference δ (delta)*[2].

However, the ΔH_{mix} value overlaps with the solid solution and intermetallic phases in HEAs as shown in Figure 10b. Thus in defining a new way to separate intermetallic and solid solution phases, Yang and Zhang [27] have proposed a parameter Ω, which contains both ΔH_{mix} and ΔS_{mix},

$$\Omega = \frac{T_m \Delta S_{mix}}{|\Delta H_{mix}|} \qquad T_m = \sum_{i=1}^{n} X_i (T_m)_i \tag{2.11}$$

$(T_m)_i$ is the melting point of element i, X_i is the atomic fraction. From Figure11 it is clear that only solid solution phases are found in as-cast HEAs for $\Omega \geq 1.1$ and $\delta < 3.6$ %. Similarly solid solution and intermetallic phases are found in range of $3.6 \leq \delta \leq 6.6\%$ and $1.1 \leq \Omega \leq 10$ [27]. But these conditions are only limited to as-casted HEAs. The stability of solid solutions and intermetallic compounds in HEAs are calculated by comparing with mixing entropy of for solid solution alloys and enthalpy of formation of binary compounds. It was assumed that the mixing enthalpy $\Delta H_{mix} = 0$ and entropy of formation of intermetallic compound $\Delta S_{IM} = 0$. In reality ΔH_{mix} is negative in some cases. ΔS_{IM} and ΔS_{mix} are comparable in ordered structures, where number of alloying elements is greater than number of sub lattices [28].

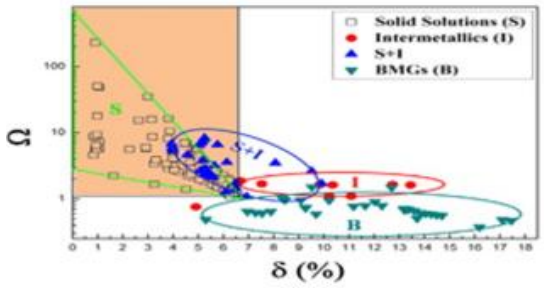

Figure 11. *Relationship between Ω and δ%* [27]

In a new approach for phase selection criteria Seknov et al [28] has considered both enthalpy and entropy terms in competing phases such as intermetallic and solid solution phases. The proposed new criterion is

$$k_1 = \frac{\Delta H_{IM}}{\Delta H_{mix}} < -\frac{T\Delta S_{mix}}{\Delta H_{mix}}(1 - k_2) + 1 \equiv {k_1}^{cr}(T) \tag{2.12}$$

Where $k_1 > 1$ and $0 \leq k_2 < 1$ is the thermodynamic condition for the formation of solid solution phases. ΔH_{IM} is the heat of formation of intermetallic phase, and ${k_1}^{cr}(T)$ is a criteria where the intermetallic phase formation is suppressed at temperature T if

$${k_1}^{cr}(T) > \frac{\Delta H_{IM}}{\Delta H_{mix}} \tag{2.13}$$

Thus, a simple thermodynamic criterion is proposed as in Equation 2.13 where the equilibrium phases can be predicted. So far the modeling of HEAs has not considered this criterion. Figure 12 shows a clear variation in predicting phases and the easiest way can be described by newly proposed thermodynamic criterion [28]. In the Figure 12 δr% = δ% as described in equation 2.9.

Valence electron concentration (VEC) rule

An additional rule or parameter is proposed by Guo [29] for the prediction of phases such as FCC, BCC and HCP (Hexagonal closed packed). According to Hume-Rothery rule, the valence electron concentration can strongly influence the formation of different crystal structures in a solid phase in the absence of a strong atomic size influence. When the total number of electrons in the valence band are included with d-electrons, the average VEC value is defined as

$$VEC = \sum_{i=1}^{n} X_i (VEC)_i \tag{2.14}$$

According to Guo [29] the VEC rule can quantitatively predict the phase stability of FCC and BCC in HEAs. At 6.87< VEC < 8.0, mixed FCC and BCC phases exists (except one alloy group $Al_xCoCrCu_{0.5}FeNi$ which has BCC as a sole stable phase). At VEC < 6.87 the stable phase is BCC and VEC > 8.0 the stable phase is FCC. The same is shown in fig. 13 [29].

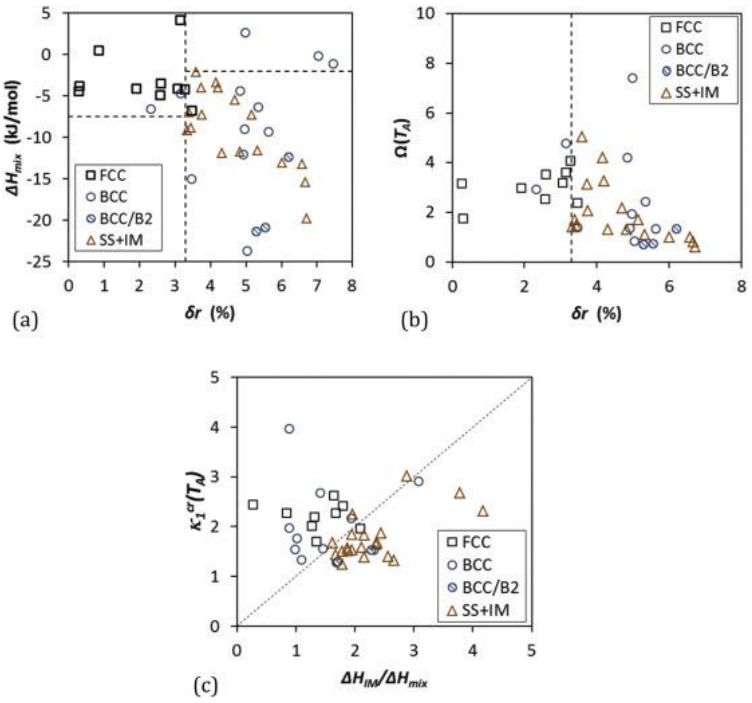

Figure 12. *(a) The* $\Delta H_{mix} - \delta r$, *(b)* $\Omega(T_A) - \delta r$ *and (c)* $\kappa 1^{cr}(T_A) - \Delta H_{IM}/\Delta H_{mix}$ *plots for annealed HEAs with different phase contents after annealing.*

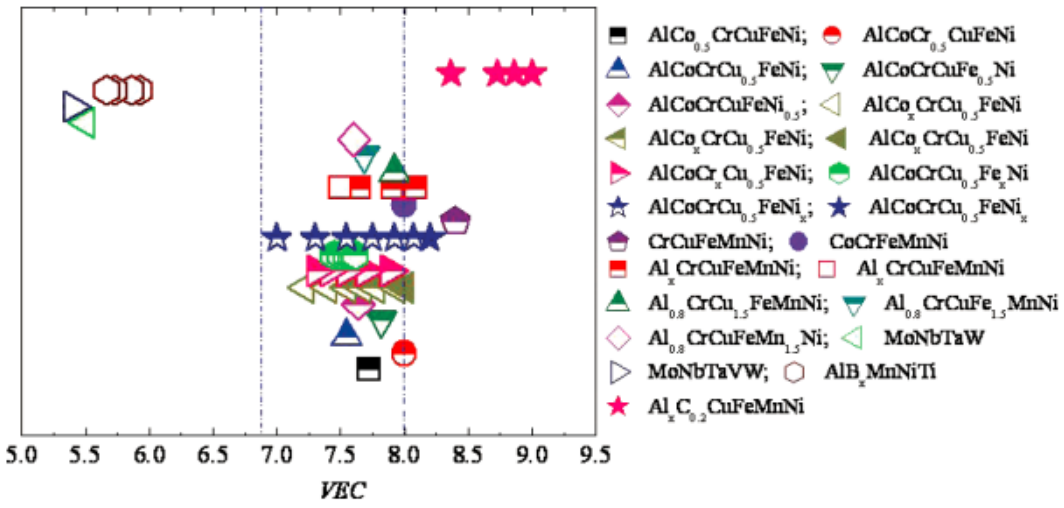

Figure 13. *Relationship between VEC and the fcc, bcc phase stability for more HEA systems* [29]

For a comprehensive analysis Figure 14 gives a clear idea of crystallinity especially for single phase solid solutions, which is a plot of VEC verses ϕ for about 90 casted HEAs, here ϕ represents a new parameter which is defined by Ye et al [25]

$$\emptyset = \frac{S_c - |\Delta H_{mix}|/T_m}{|S_E|} \qquad (2.15)$$

Where S_c is configuration entropy which is equal to ΔS_{mix} in this condition, T_m is alloy's melting point, and S_E is excessive entropy of mixing.

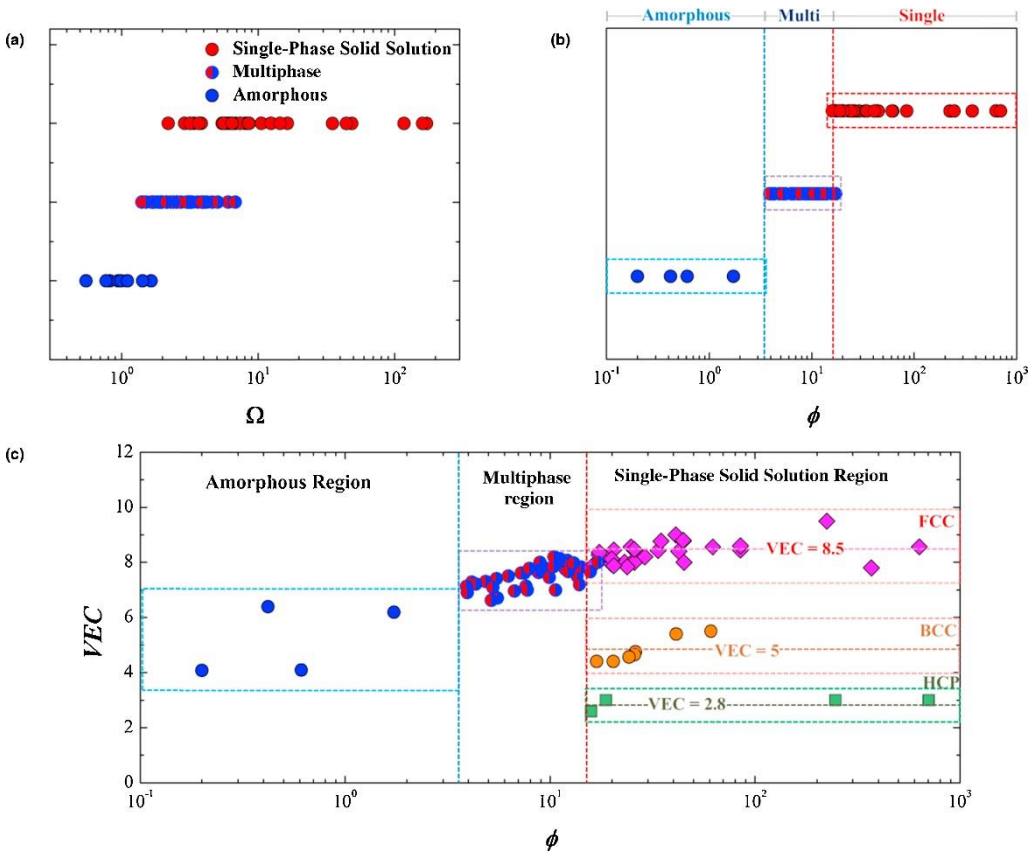

Figure 14. *The plot of (a) the Ω values versus phases and (b) the ϕ values versus phases for the HEAs. (c) The plot of the VEC versus ϕ for different HEAs. The FCC solid solution mainly forms around a VEC of 8.5, BCC around a VEC of 5, and HCP around a VEC of 2.8, each within a narrow band* [30].

From the Figure 14 within the region of single phase solid solution (ϕ *~20*), FCC is around a VEC of 8.5 ± 1.0, BCC around a VEC of 5 ± 0.7 and HCP around a VEC of 2.8 ± 0.2. When HEA falls under ϕ < 20 then there is a clear indication of amorphous phase formation for which VEC is overtaken by the other effects such as atomic size differences.

Additionally, formation of phases at elevated temperatures can be related to Guo's criteria of VEC which defines the presence of σ phases. The alloys located in BCC+FCC region tend to transform the phases at elevated temperatures during annealing treatments. For example, some HEAs have phases that are stable only at intermediate temperatures, such as η phase and σ phase. A study by Tsai et al [31] has shown the stability of σ phase, it says that σ phase is directly related to VEC. Figure 15 shows the relationship between VEC and σ phase.

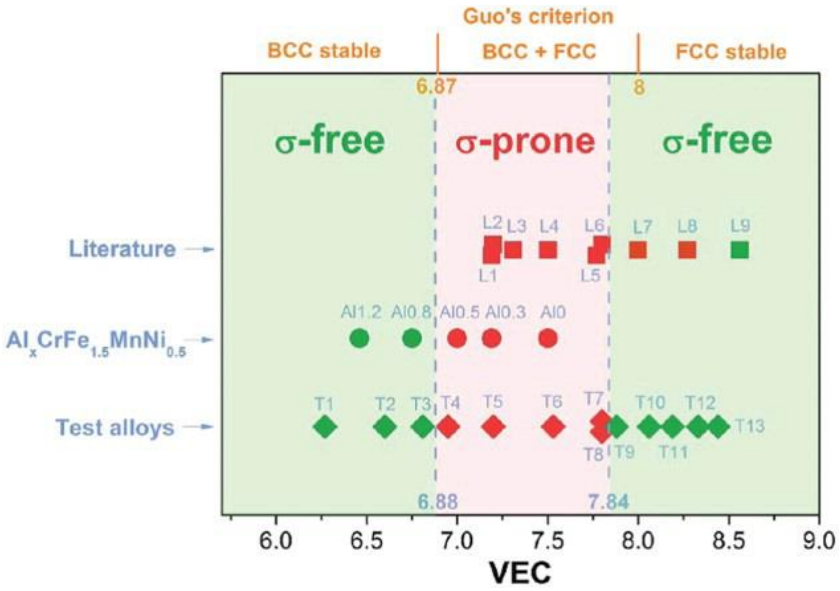

Figure 15. *Relationship between the VEC and the presence of σ phase after aging for a number of HEAs* [9]

2.3.1 Computational Material Modelling of HEAs

Integrated Computational Materials Engineering has been a cutting edge approach in many fields which are considered as one of the design approach of products. Thus the core properties, structures and performances can be predicted from this technique. Since, the emerging HEAs prospectus has an intensive requirement for modelling of different possible configuration, different approaches are made to predict the properties, phases and structures. The atomic structure modelling of a multi-principle elemental alloys was be made by Wang[32] by using the principle maximum entropy.

The possible entropic contributions are mainly of 4 different types. In addition to the total configurational entropy as mentioned in Equation 2.11, there are three more contribution such as electronic entropy (ΔS_{el}), magnetic entropy (ΔS_{Mag}) and vibrational entropy (ΔS_{Vi}). So, the total entropy influencing the atomic structure can be expressed as follows.

$$\Delta S_{total} = \Delta S_{conf} + \Delta S_{el} + \Delta S_{Vi} + \Delta S_{Mag} \tag{2.16}$$

The modelling of HEAs considering the above expression is done using Monte-Carlo simulations [32]. Additionally, *ab initio* methods were approached by Duanchen et al [33] in predicting phase stability of CoCrFeMnNi HEA, this modelling approach also used the total entropy expression (equation 2.17).

Similarly, for the calculation of elastic constants in HEAs using coherent approximations, *ab initio* methods were used by Tian et al [34]. The tool used in this method was based

on Exact Muffin-Tin Orbitals method, in combination with coherent potential approximation. The coherent potential approximation can handle both the chemical and magnetic disorders.

2.4 Processing of HEA

The most pronounced casting techniques of HEAs until the recent updates in this research area are arc melting and induction melting. A schematic diagram is shown in Figure.16 of arc melting furnace. The temperature inside the furnace can reach more than 3000^0C and is controlled by electrical power. Thus the melting elements can be mixed in this furnace at liquid state[15]. The one disadvantage of the furnace is the evaporation of low melting point elements. The description of induction melting furnace is given in chapter 3.1.

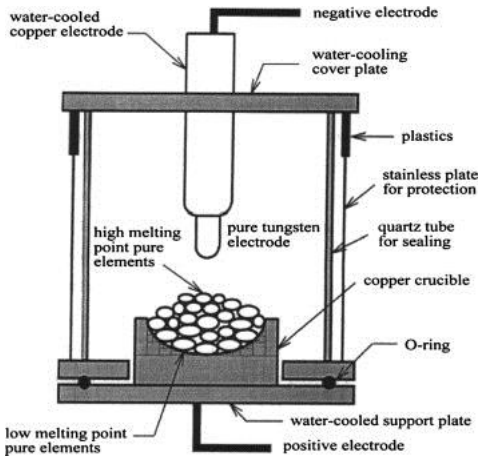

Figure 16. *A schematic diagram of arc melting furnace* [15]

The decomposition of AlCoCrCuFeNi HEAs is found in the study by Singh [35], which says that higher cooling rate endorses single phase, whereas lower cooling rate forms multiple phases as shown in the block diagram Figure 17. This shows that there is a strong influence of cooling rate on the microstructure. Thus HEAs can form a single phase solid solution only at higher cooling rates and the formed high entropy phase is metastable. This infers that a proper annealing treatment is required to define the proper equilibrium state. The annealing at higher temperatures and cooling at lower rate produces multiple phases which decreases the configurational entropy of mixing [15].

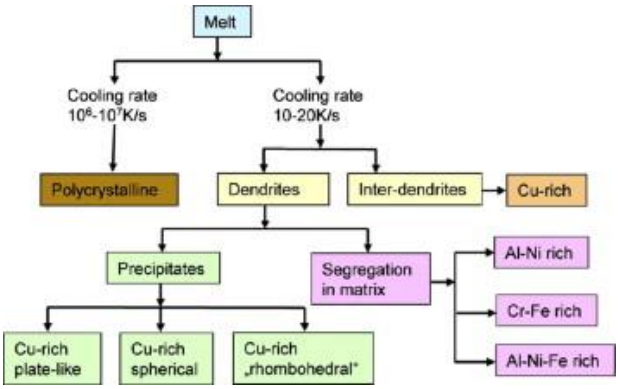

Figure 17. *Block diagram representing phase segregation observed during solidification of AlCoCrCuFeNi HEA by splat quenching (cooling rate 10^6–10^7 K s^{-1}) and casting (cooling rate 10–20 K s^{-1})* [35]

Additionally, there is another processing technique which is knows as Bridgman-Stock Barger method. This method is used to grow single crystals ingots, and involves heating the polycrystalline material above the melting point and cooling slowly from one corner of the container. One of the study by Zhang et al[36], says that the cooling of AlCoCrFeNi alloys by this method showed equi-axed grains. This is due to high temperature gradient and low growth rate velocity. Adding to these casting techniques, Wang [37] has shown the possibility of surface coating of $Ni_xCo_{0.6}Fe_{0.2}Cr_ySi_zAlTi_{0.2}$ HEAs by thermal spraying technique, and it shows that the hardness of coating surface is increased. This is because of some precipitates formed on the surface. The as-casting of the same alloy has not produced the same precipitates [15].

Processing by solid state is also done by mechanical alloying which is known as solid state powder processing. It comprises cold welding, fracturing and recurring cold welding of the powder particles. Various studies have been carried out on synthesizing of HEA powders. One of them is by Varalakshmi et al [38] who reported the nano-crystalline equiatomic HEAs synthesized by mechanical alloying. The powders can then be sintered in hot-isostatic pressing and final heat treatment is done to avoid internal stresses.

The preparation from the gaseous state can be done by sputtering technique, which is a coating of multi-component material. A study by Chang et al [39] has shown that coating of $(AlCrTaTiZr)N_x$ by sputtering has shown that an increase in nitrogen content has caused increase in crystallinity from amorphous phase to a nano-composite to finally a crystalline phase. This has shown a variation in mechanical properties such as creep behaviors, deformation mechanisms and interface adhesions. The increase in nitrogen increased the hardness of the interface bonding as nitrogen formed a very strong covalent bond with silicon and oxygen atoms on the substrates [15].

2.5 Microstructures of HEAs

Consider the XRD analysis of $Al_{0.5}$CoCrCuFeNi from various processing techniques. Figure17 shows that the microstructure is influenced by the cooling rate, and obviously by the addition of different alloying elements. Some of the elements such as copper enhances or stabilizes the formation of FCC phases, aluminum enhances the BCC phase stability and, molybdenum hinders the segregation of copper phase and thus forms BCC and α phases [15]. The kinetics of cooling rate of Al_xCoCrCuFeNi (X = 0.0-3.0) HEAs studied by Tong et al [18] has shown the spinodal decomposition with the increase in aluminum content. The XRD of same alloy $Al_{0.5}$CoCrCuFeNi with different cooling rates or conditions have shown different peaks (as shown in Figure 18). This clearly infers that the phase formation and microstructures are kinetically dependent [15].

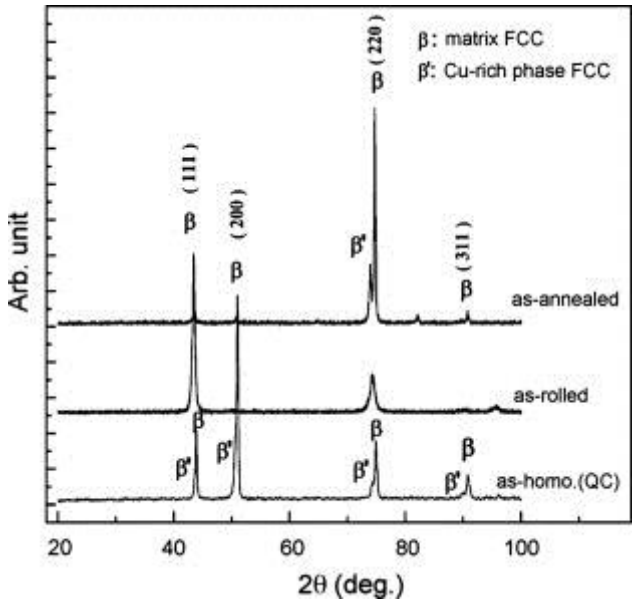

Figure 18. *XRD patterns of $Al_{0.5}$CoCrCuFeNi alloy. QC= Quenching* [40]

The HEAs casted through casting route (as mentioned in chapter 2.4) , comprises of a typical microstructure which includes Dendritic (DR) and Inter-dendritic (IR). DR is comprised of precipitates and nano-structured phases. Considering the example Al_x-CoCrCuFeNi (X = 0.0-3.0) which was studied by Tong et al [41], has shown similar microstructural features. Element like copper has segregated inside the IR region. The increase in aluminum has gradually decreased the solubility of BCC and FCC matrix phases, with lowering temperatures due to weakening effect of the entropy of mixing. Figure 19 shows the sequence of phase formation with increase in aluminum content [1]. There is copper segregation found in IR regions at aluminum (0.0 – 0.5), and also low concentration of aluminum. The DR which is in larger volume fraction, is comprised of all the other principle elements. At this concentration both IR and DR are in simple FCC phases. When the cluminum content has exceeded 0.8 the IR began to decompose into two phases, which formed spinodally decomposed structures. After X = 1.0 the IR showed two spinodally decomposed phases, and gradually when aluminum was increased the

more eutectic IR phases were decreased and spinodally decomposed phases were increased. Vein structures in polycrystalline structure were formed at X = 2.3. The Figure 20 shows the SEM on the formation of new phases with increase in aluminum content [18].

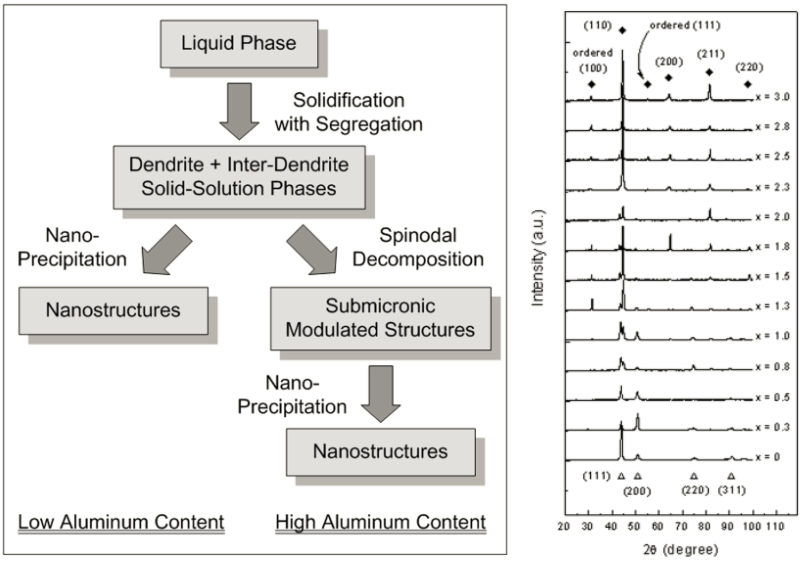

Figure 19. *(a) Different phases formed with change in Aluminum content (b) XRD analyses of $Al_xCoCrCuFeNi$ alloy system* [18].

From the study of differential thermal analysis, microstructural characterization and XRD analysis (fig.19b) of the $Al_xCoCrCuFeNi$ alloys, the phase transitions are listed as shown in the Table 1. The different phase listed are used to construct a phase diagrams which clearly depicts the formation of different phases at different temperatures.

Table 1. *Results from DTA analysis of the $Al_xCoCrCuFeNi$ alloy system showing Phase Transition Temperatures* [18].

Alloy	T_{order} (°C)	T_{sp}^1 (°C)	T_{sp}^2 (°C)	T_m^{Cu} (°C)	T_m^s (°C)	T_m^l (°C)
$Al_{0.0}CoCrCuFeNi$	692	—	—	1135	1339	1389
$Al_{0.5}CoCrCuFeNi$	695	—	—	1153	1279	1362
$Al_{1.0}CoCrCuFeNi$	—	580	660	1117	1170	1330
$Al_{1.5}CoCrCuFeNi$	—	577	648	1086	1259	1355
$Al_{2.0}CoCrCuFeNi$	—	—	—	1077	1303	>1400
$Al_{2.5}CoCrCuFeNi$	—	—	—	1078	1260	>1400
$Al_{3.0}CoCrCuFeNi$	—	585	610	1096	1293	>1400

*T_{order}: ordering temperature, T_{sp}: spinodal decomposition temperature, T_m^{Cu}: melting point of Cu-rich phase, T_m^s: solidus temperature, and T_m^l: liquidus temperature

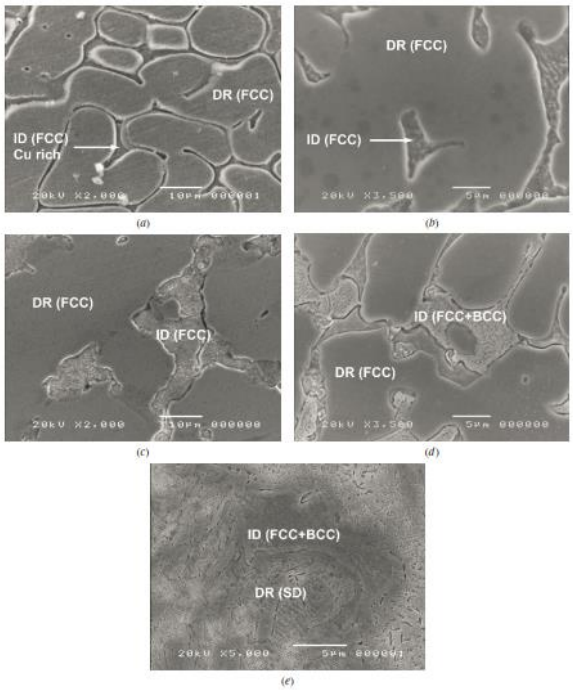

Figure 20. *SEM images of as-cast AlxCoCrCuFeNi alloys with different Al contents (x): (a) 0, (b) 0.3, (c) 0.5, (d) 0.8, and (e) 1.0* [18]

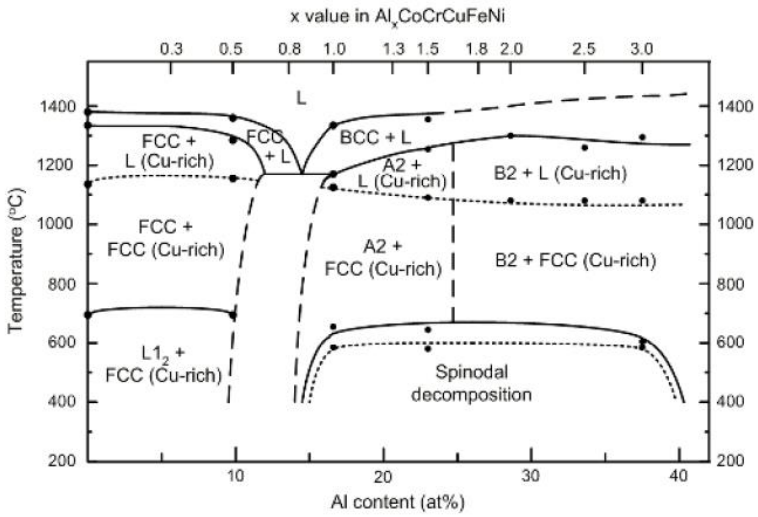

Figure 21. *Predicted phase diagram of Al$_x$CoCrCuFeNi alloy system with different Al contents (x), L = liquid phase* [18].

The Figure 21 shows the phase diagram of Al$_x$CoCrCuFeNi alloy system where the black dotted lines are the phase transition temperatures which are measured by differential thermal analysis with maximum temperature limit of 1400^0C [18].

Consider the microstructures of AlCoCuCrFeNiMo$_x$ system, a study by Zhu et al [42], the casting was done by arc melting. The Figure 22 shows the back scattering SEM images of AlCoCuCrFeNiMo$_x$ alloys system. Their microstructure comprised of DR and ID regions till x = 0.2. The increase in molybdenum content decreases the copper-rich phase

and eutectic structures are evolved. The new phases are defined by A, B, at x=0.4 and C, D at x=0.6-1.0 respectively. A and C are rich in molybdenum content. It was shown that the higher content of molybdenum in $AlCoCuCrFeNiMo_x$ [42] and $AlCoCrFeNiMo_x$ [7] alloy systems form the eutectic structure. In both the alloys an unidentified α-phase, which is rich in molybdenum (a shown in Figure 23) is formed by this eutectic reaction.

For the $AlCoCuCrFeNiMo_x$ the α-phase is formed inside the structures C and D, where structure C has finer α-phase and structure D has α-phase [42].

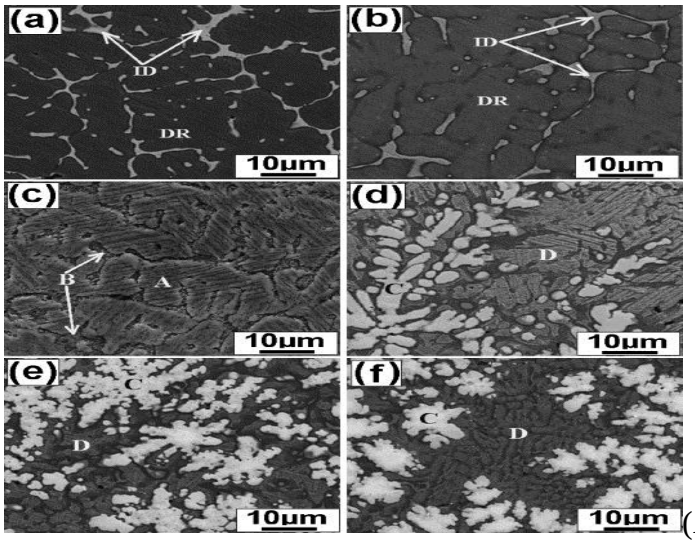

(A)

Figure 22. *Back-scattering SEM images of as-cast $AlCoCrCuFeNiMo_x$ alloys: (a) 0, (b) 0.2, (c) 0.4, (d) 0.6, (e) 0.8 and (f) 1.0* [42].

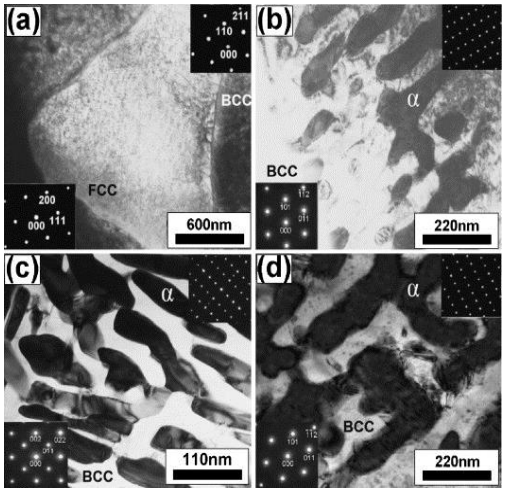

Figure 23. *TEM image (inset pictures are SAED patterns) of as-cast $AlCoCrCuFeNiMo_x$ alloys: (a) 0.2, (b) 0.4, (c) 0.6 (Phase A form fig 22 d), (d) 0.6 (Phase B from fig 22 d)* [42].

Additionally, the XRD analysis also shows the presence of BCC and FCC structures in $AlCoCuCrFeNiMo_x$. The relative intensity of FCC is found lower than that of BCC which

shows the lower fraction of FCC phase. Increase in molybdenum content slowly reduces the FCC peaks and finally at the arrival of α-phase, the FCC peaks totally disappear.

Since the mixing enthalpies of copper and most other elements like Co, Cr, Fe, Ni and Mo are positive (8, 12, 13, 4 and 19 kJ/mol respectively). The copper atom is rejected by grain boundary and thus a copper rich phase is formed inside the IR region. But, the increase in molybdenum content gradually reduces the copper rich phase as shown from the experimental results [42].

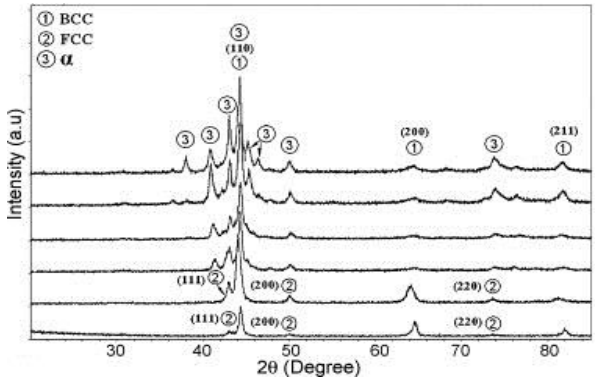

Figure 24. *XRD patterns of as-cast AlCoCuCrFeNiMo*$_x$ *(*x *= 0, 0.2, 0.4, 0.6, 0.8 and 1.0) alloys* [42].

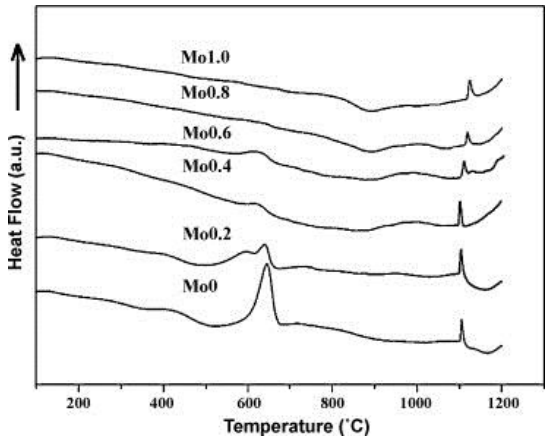

Figure 25. *DSC curves of as-cast AlCoCrCuFeNiMo*$_x$ *(*x *= 0, 0.2, 0.4, 0.6, 0.8 and 1.0) alloys* [42].

Moreover, it was also shown that increase in molybdenum content increases the hardness of alloys. The α-phase which is shown in TEM images has less slip systems than BCC and thus is proved to be brittle. The presence of α-phase was showing an increase in the strength and decrease in the ductility. Additionally, from thermal analysis as shown in Figure 25, the alloy system particularly made itself more reliable for high temperature applications, as the phase changes are restricted to high temperatures.

2.6 Properties

Unlike many other alloys, the recent HEA designs are targeted to meet clear goals. Thus the individual alloying elements are carefully chosen to deliberately introduce new phases, and tailored microstructures. There are many types of HEAs based on their properties, mostly the HEAs studies are focused on a common group of metallic materials such as aluminum, cobalt, chromium, copper, iron and nickel. There are several reported studies about microstructures, crystal structures, phase transformations and mechanical properties of these group HEAs [35], [41], [43], [44]. There are some considerable efforts in enhancement of properties by adding some extra elements which are defined as 'derivatives'.

A very recent study has shown that the design of HEAs has already entered a different stage, in designing as they are designed to target a particular application. Tsai et al [5] has classified the design strategies in three categories such as Application based, Enhancing entropy of conventional alloys and Incorporating second phases.

Application based redesigning is done by selecting different components by considering the desired properties. The examples in this criteria are refractory HEAs (which are targeting high temp applications)[11], [45]–[47], light HEAs (to have high strength and ductility) [48]–[50], HE bulk metallic glass(for high strength and good corrosion resistance) [51]–[53] , high entropy superalloys (a derivative of titanium and could potentially replace superalloys)[54], [55].

The enhancement of configurational entropy of conventional alloys can be done by changing the solute composition. Thus the desired properties may be achieved. Properties can improve by a large scale by incorporating second phases in HEAs in the form of simple phases (BCC, FCC and HCP) or by deliberately introducing complex phases as η-Ni_3Ti phase [5].

2.6.1 Mechanical properties

In a critical review of HEAs by Tsai et al [9], the mechanical properties are dependent mostly on critical factors such as hardness, volume and morphology of the comprising phases. The easiest way in estimating hardness is by evaluating the volume of harder phase (basically it is known that BCC is harder than FCC). The deformation mechanism is a yet a research topic for most of the HEAs. After studies on various HEAs comprised of single FCC phase, it is found that deformation is governed by planar slips type dislocation and therefore at low temperature (cryogenic) high strain rate obviously gives twinning effect. The room temperature high strain rate give rise to dislocation cell structures.

One of the most studied and current thesis test specimen $Al_{0.5}CoCrCuFeNi$ alloy was investigated by cold deformation and annealing by Tsai et al[21]. The deformation twinning is observed by blockage of local slip planes by Widmanstätten precipitates. Thus it could be stated that the dislocation slip and twinning are the main deformation mechanisms [9].

The effect of annealing on the mechanical properties of the AlCoCrCuFeNi alloy system depends on the phase transformation. The different phases formed during annealing such as BCC phase increases hardness and the alloy becomes more brittle. The long time annealing give raise to σ phase which hardens the alloy and significantly reduces the ductility [56], [57]

As mentioned above, the derivatives are the alloys formed with the addition of one or more principle elements from the standard HEA (AlCoCrCuFeNi) alloy system. The addition of titanium element usually leads to the formation of intermetallic phases such as lava phases [39], [58], σ phase [58], η-Ni_3Ti phase [59]. This is because the titanium forms negative mixing enthalpy with rest of the components. These phases strengthen the HEAs i.e. the hardness is significantly increased with a slight increase in titanium content.

Addition of molybdenum to the system enhance the formation of BCC phases and molybdenum-rich σ phase. Since the σ phase is very hard and brittle, the hardness is significantly enhanced. The details are described in the section 2.5. Figure 26 shows the room temperature compressive stress strain curves of as-cast $AlCoCrCuFeNiMo_x$ alloys. The curves show increase in compressive strength with the increase in molybdenum content. The maximum compressive strength is reached at $Mo_{0.5}$ which is 2757 MPa, and the maximum compressive fracture strength is shown by $Mo_{0.3}$ which is 3208 MPa [42].

Effectively, by the addition of alloying elements such as manganese and vanadium to AlCrCoCuFeNi HEA the compressive strength and ultimate strain is decreased. This is shown in the Figure 27 (also shows the influence of titanium addition). The compressive stress-strain curve has shown that the compressive strain has reduced by 24%. This is because the AlCrFeCoNiCuMn alloy has a chromium-rich phase, which has influenced the crack nucleation. The titanium addition shows no strain hardenability, thus the compressive strength and ultimate strain is lower. There is a small amount of strain hardenability in manganese and vanadium rich AlCrCoCuFeNi HEA, which has a little greater strength and ductility [60].

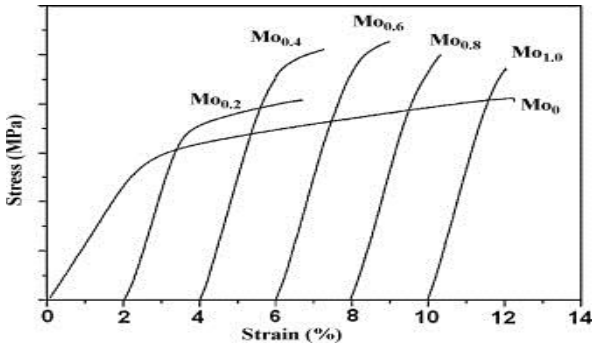

Figure 26. *Compressive Stress-Strain curve of as-cast AlCoCrCuFeNiMo$_x$ where (*x *= 0, 0.2, 0.4, 0.6, 0.8 and 1.0) alloys* [42]

The compressive strength of AlCrFeCoNiCuV HEA is greater than all derivatives because of the presence of modulated plate like structure inside the dendritic region. This modulated plate like structure is comprised of two-phase region which has same lattice constant. This enhances the compatible deformation. The analysis says that a strong binding and high melting point metals such as vanadium are required to increase slip resistance [60].

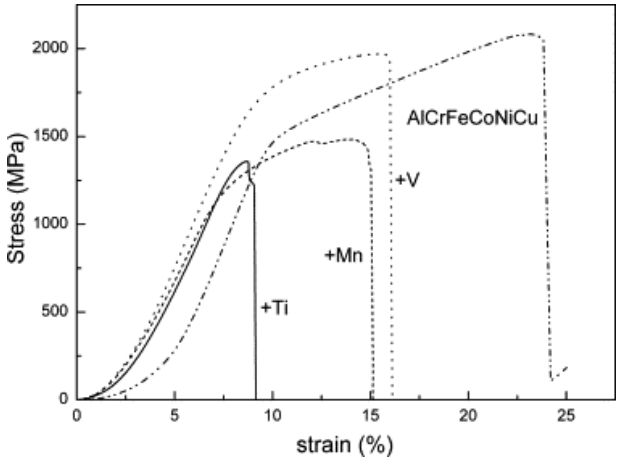

Figure 27. *Compression Stress–strain curves of AlCrCoCuFeNi and its derivatives (Mn, Ti, V)* [60]

The so called 'paradox of strength – ductility' is being called off by some set of HEAs. We all know that increase in strength in conventional alloys leads to loss of ductility and vice versa. Therefore, the endeavor which led to the innovation of HEAs has called off the paradox, which is shown in Figure 28. We know that stacking fault energy (SFE) plays a significant role in the promotion of twinning mechanism. The lower the stacking fault energy the greater is the probability of twinning.

Some of the HEAs like $Ni_{14}Fe_{20}Cr_{26}Co_{20}Mn_{20}$ and $Ni_{14}Fe_{21.5}Cr_{21.5}Co_{21.5}Mn_{21.5}$ have very less SFE like 3.5 mJ/m^2 and 7.7 mJ/m^2 respectively [61], which are even less when compared to 304L steel which has a SFE value of ~7mJ/m^2. The reason behind the increase

in strength and ductility is that the low SFE enables the splitting of dislocations into partials, thus cross slip and climb occurs. Resultantly, a high yield strength can be obtained in theses HEAs with low SFEs. Additionally, the low SFE leads to twinning induced plasticity and thus the ductility increases [30].

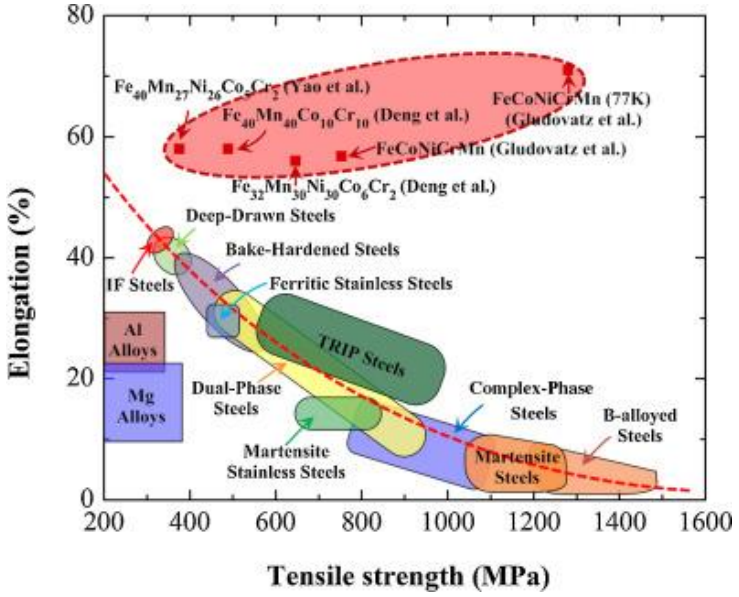

Figure 28. *Strength versus ductility properties for low-SFE HEAs and conventional alloys* [30]

2.6.2 High strain rate compressive deformation behavior of HEAs

There are many publications which focus on compressive deformation of HEAs [6], [15]. The tests conducted were mostly at quasi-static strain rates, under temperature ranging from high temperatures to cryogenic temperatures. [42], [62]–[66]. Tong et al [67] have studied compressive properties of $Al_xCrCoCuFeNi$ up to strain rates of 10^{-1}/s. There is less research focused on high strain rate behaviors. Kumar et al [6] studied dynamic behavior of an $Al_{0.1}CrFeCoNi$ alloy at high strain rates of 1000/s and 2600/s.

The plastic deformation behavior can be explained by slipping and twinning. The slip movement of dislocation is blocked by obstacles such as dislocations, grain boundaries, inclusion or voids. The obstacles are overcome by energy. The source of energy is externally applied stress and/or by internal thermal atomic vibrations. There are mainly two type of obstacles, thermal and athermal. Thermal obstacle can be overcome by only thermal energy, without external stresses. However, athermal obstacles need greater energy to overcome the obstacle, thus stresses are applied externally [68].

Additionally, the twinning also contributes to plastic deformation. In this mechanism the motion of the atoms occurs in a specific direction with in a crystal plane and thus reorients

the atomic positions in a lattice. For example, twinning in FCC leads to the formation of HCP at the twin boundary[69].

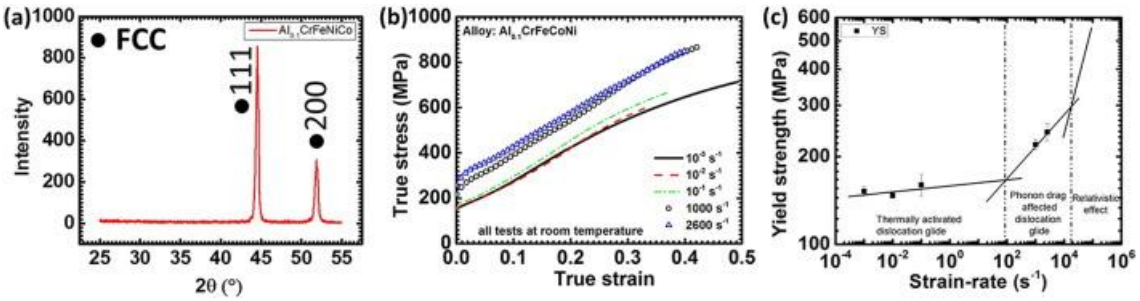

Figure 29. *As-cast $Al_{0.1}$CrFeCoNi alloy (a)XRD patterns showing FCC structure (b) True stress vs. true strain curve (c) Yield strength variation as a function of strain -rate and deformation mechanisms in different regions*[6]

A study by Kumar et al [6] shows the high strain rate compressive deformation behavior of $Al_{0.1}$CrFeCoNi alloy. Figure 29a shows the XRD peaks of $Al_{0.1}$CrFeCoNi alloy as single phase FCC structure. The true stress vs true strain (Figure 29b) shows that the average yield stress is high strain-rate dependent in dynamic conditions (1000/s and 2600/s). Figure 29c shows a plot between yield stress and strain rate on log-log scale. In the plot, the phonon drag effected by dislocation region is the region where the dynamic conditions are tested (10^2 to 10^4/s) [6].

It is known that phonon drag effect phenomenon highly influences the deformation at high strain rates. Thus it should be noted from the Figure 29c that phonon drag effect is the main reason for significant rise in yield stress values. This significant rise is compared to rise of yield stresses at low strain rates (quasi-static conditions). The quasi-static region is the thermally activated dislocation glide region as mentioned in Figure 29c [6]. Additionally, at high strain rates, the deformation is high enough that the heat cannot transfer to the surrounding environment. This cause an excessive increase in the heat of the metal. The heat could potentially form shear bands by melting the slip planes. These shear bands are called as adiabatic shear bands [70].

After a detailed examination of the microstructures of high strain rate compressed $Al_{0.1}$CrFeCoNi alloy samples, the twinning plastic deformation mechanism was seen. Since CrFeCoNi HEA have low stacking fault energy[61] and addition of aluminum can decrease the stacking fault energy, it is assumed that $Al_{0.1}$CrFeCoNi alloy has low stacking fault energy. Figure 30 shows the scanning electron microscopy (SEM) and electron back scattered diffraction (EBSD) images at different conditions of $Al_{0.1}$CrFeCoNi alloy. Both the deformed samples (quasi-static and dynamic) showed abundant twinning induced plastic deformation. Higher density of twins in EBSD of high strain rate compressed sample can be seen. This twinning is caused by low stacking fault energy [6].

A study by Tong et al [67] has shown the mechanical behavior of $Al_xCoCrCuFeNi$. The AlCoCrCuFeNi HEA has shown presence of slip bands at low strain rates. The $Al_{0.5}CoCrCuFeNi$ HEA has shown positive work hardenability. The increase in aluminum content had resulted increase in the ratio of BCC to FCC phase. This enhanced the solid solution strengthening. However, there seems not to be a study focused on high strain rate properties of $Al_xCoCrCuFeNi$ HEAs.

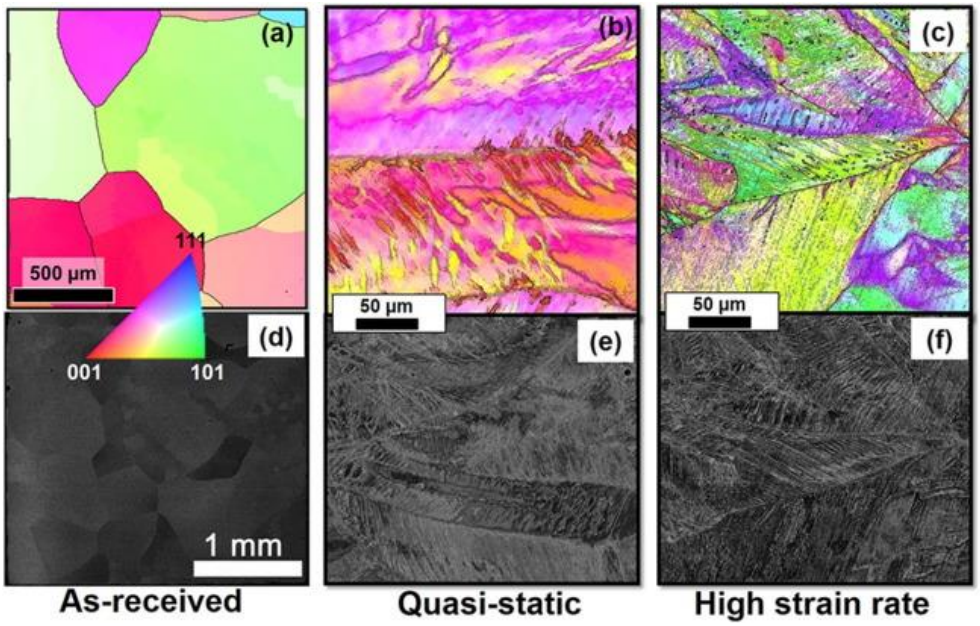

Figure 30. *EBSD images (a)–(c) and SEM (d)–(f) images for as-received (a and d) and deformed samples — quasi-static (10^{-3}/s) (b and e), high strain-rate (~ 2600/s) (c and f)* [6].

2.6.3 Oxidation and Corrosion properties

There are many publications which are in relation with HEA oxidation behaviors[44], [59], [71]–[73]. These are based on transition metals group (CoCrCuNiFeMn). The oxidation behavior of HEAs is similar to conventional alloys systems like nickel, titanium, manganese, chromium or aluminum based. Considering a study by Daoud [74] about the oxidation behaviors of $Al_{0.5}CoCrCu_{0.5}FeNi_2$, $Al_{1.5}CoCr_2Cu_{0.5}FeNi$, and AlCoCrCuFeNi HEAs at 800 °C and 1000 °C in air, the low aluminum composition gives a combination of NiO, Fe-oxide, Cr_2O_3 and Al_2O_3. At 1000 ^{0}C of the same alloy (low Al content) the Cr_2O_3 is formed above Al_2O_3. The higher concentration of aluminum leads to formation of Al_2O_3 scales over the surfaces at both the temperatures[74]. Similarly, Holcomb [75], studied the oxidation behavior of eight CoCrFeMnNi-based HEAs with different compositions, and also along with other conventional alloys. It was shown that the chromium and manganese containing HEAs formed both Cr_2O_3 and manganese oxides preferentially [75].

According to a study by Gorr [76], [77] on NbMoCrTiAl (a refractory HEA) with addition of 1% of Si the oxidation growth kinetics is parabolic in nature. The silicon-less HEA is having linear growth rate and is also porous. Similarly a study by Butler [71], on high temperature oxidation behavior of $Al_{0.3}$CoCrFeNi, $Al_{1.4}$CoCrFeNi, $Al_{2.1}$CoCrFeNi alloys at 1050 ^{0}C formed oxide surfaces with Cr_2O_3 over Al_2O_3 layers. The increase in aluminum content led to enhanced oxidation resistance by formation of external Al_2O_3 layers. This is because of Ni-Al rich B2 phase which is formed near the surfaces. Also parabolic oxidation growth rate is observed [71].

The corrosion properties of some HEAs have been verified both in NaCl and H_2SO_4 [19], [49], [78]–[80]. It is shown that in both of the solutions some of these HEAs show better corrosion properties over 304 SS and 304L SS steels which also have good pitting corrosion [79]. Most of the above cited references are based on CoCrFeNi based HEAs.

Qiu[81] has reported electrochemical properties of a wide range of HEAs in a solution of 0.6 M NaCl solution. The range of electrochemical potentials and pitting potentials are shown in Figure 33 as in comparison with some austenitic stainless steels. Reportedly an arc melted $Al_{0.9}$CoCrFeNi alloy has shown noble corrosion potential and low corrosion current density, while possessing simple FCC + B2 phases [81]. In the Figure 31 CoCrFeNi (SPS* = spark plasma sintering) was held at 1000°C for 5 min, while CoCrFeNi (SPS) was firstly held at 500°C for 5 min and then sintered at 1000°C for another 5 min.

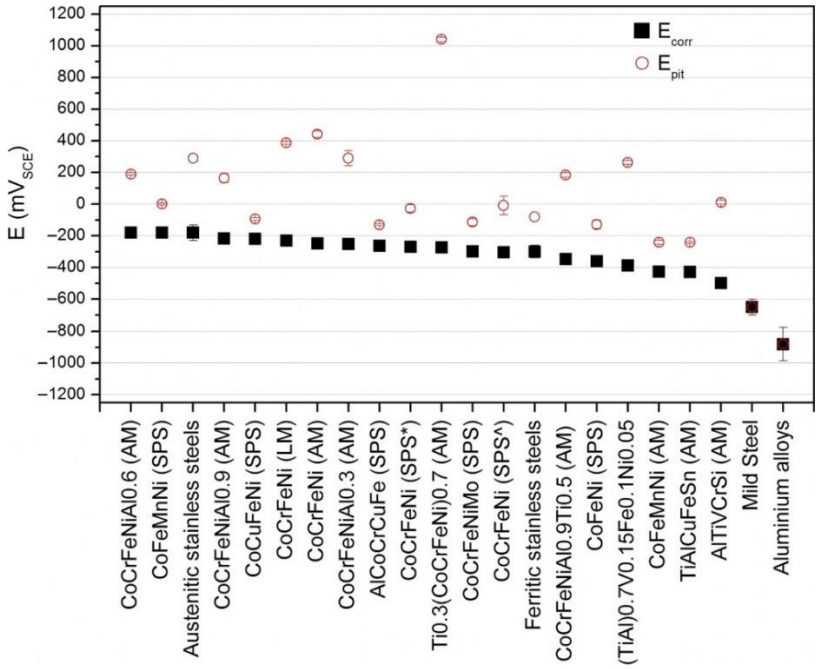

Figure 31. *HEA Corrosion potential (*E_{corr} *in* mV_{SCE}*) and pitting potential (*E_{pit} *in* mV_{SCE}*) in inactive 0.6M NaCl at 25°C.*

All the above tested HEAs have shown spontaneous passivity in 0.6 M NaCl. In a general view chromium addition improves the corrosion resistance [81].

3. EXPERIMENTAL METHODS

3.1 Materials

The experimental materials used in this work are three different HEAs, with chemical compositions as shown in Table 2.

Table 2. *Chemical composition of investigated HEAs (at. %)*

Alloy code	Empherical formula	Al	Co	Cr	Cu	Fe	Ni	Mo
HEA 1- Ref	$Al_{0,5}CoCrCuFeNi$	9.09	18.18	18.18	18.18	18.18	18.18	0
HEA 1	$Al_{0,5}CoCrCuFeNi$	9.09	18.18	18.18	18.18	18.18	18.18	0
HEA 2	$Al_{0,5}CoCrCuFeNiMo_{0,25}$	8.69	17.39	17.39	17.39	17.39	17.39	4.35

HEA – Ref is a reference sample with nominal composition of $Al_{0.5}CoCrCuFeNi$ (in atomic proportion). The sample was provided by high entropy alloy research group, Chalmers University of Technology. It was prepared by arc-melting a mixture of the constituent elements with purity better than 99.9% in a Ti-gettered (titanium-gettered) high-purity argon atmosphere. The repeated melting was carried out at least five times to improve the chemical homogeneity of the alloy. The molten alloy was then suction-cast into a rectangular copper mold measuring 15mm x 3mm x 90mm.

HEA 1 and HEA 2 are samples with nominal compositions $Al_{0.5}CoCrCuFeNi$ and $Al_{0,5}CoCrCuFeNiMo_{0,25}$ respectively. These samples were cast by induction melting in Vacuum Induction melting furnace Model ZG-0.05 L, of crucible weight 20-50 kg, rated power 160kW, MF. The melting of each composition was repeated for two times to increase chemical homogeneity. First the melting was done in open air and then re-melted in vacuum condition. Voltage was 375V, maximum rated temperature was 1700 ^{0}C and the minimum vacuum pressure was 5 mbar. The approximate dimensions of the casting are 60 mm x 85 mm x 350 mm. The total weight of the input raw material was 20kg per cast.

The casting and material characterization was described in the MSc thesis by Zhiqi [82]. The materials (HEA 1 and HEA 2) were casted two times each by air casting and vacuum casting. Firstly, the materials were cast in open air. In this technique the higher melting point metals were added first. Then the other metals were added in decreasing value of melting points. This is to avoid evaporation. The materials were cast into an ingot and then cooled. Secondly the same ingot is directly taken into the furnace after cooling and then melted in vacuum condition. The induction melted alloys were cast into ingot and was left to cool. The metals used as input are of industrial grade high purity.

3.2 Annealing

The annealing treatments, in other terms homogenization of these experiment materials, are done using high temperature tube furnaces, ENTECH SF6 as shown in Figure 32. The homogenization means, high temperature annealing at $0.8T_m$ to achieve equal distribution of all atoms.

The maximum temperature of the furnace is in the range of 1670 – 1700 ^{0}C. The maximum temperature used for the furnace till now was around 1000 ^{0}C. Since the requirement of temperature is around 1100 ^{0}C, the furnace is calibrated using thermo couple. The thermal profile from the center of the furnace to 10mm in both the direction when the set point was 1100 ^{0}C is shown in Figure 33.

Figure 32. *Tube furnace for annealing treatments*

During the heat treatment, the gap between the furnace and tube is covered with refractory wool.

The samples were prepared accordingly having dimensions 15mm x 15mm x 50 mm approximately. The sample is inserted into a ceramic holder and then pushed to the center of the furnace. The furnace is clamped and purged with argon gas to create inert atmosphere. The pressure inside the tube is 100mm of Hg which is maintained using the pressure regulating valve and a pressure gauge. The furnace is started with a set temperature of 1080 ^{0}C which is the $0.8T_m$ of $Al_{0.5}$CoCrCuFeNi [18]. At this temperature it is expected that the copper phase is not melted as its melting temperature is 1153 ^{0}C. The annealing treatments are planned for 72 hours each. Table 3 shows the samples and their annealing treatments.

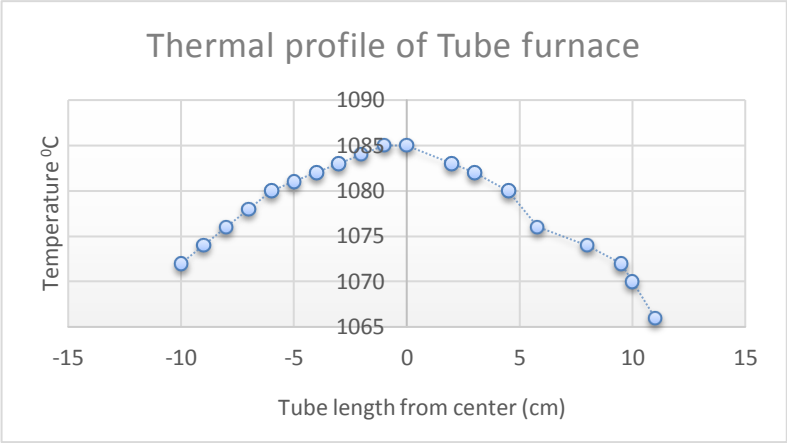

Figure 33. *Calibrated temperature of Tube furnace*

The samples underwent homogenization (annealing treatment) for 72 hours with a ramp up of about 2 ^{0}C/min. After 72 hours of annealing, the samples HEA 1 – A1 and HEA 2 – A1 are left to cool inside the furnace. The samples HEA1-A2 is quenched in the salt bath at 270 ^{0}C, after annealing for 72 hours. During the heat treatment of HEA 2 – A2, the furnace was shutdown forcibly at 60 hrs., because of the false reading of temperature gauge. Then the sample is quenched in salt bath at 270 ^{0}C. To check the actual temperature at the center of furnace, thermo-couple was used. The reading was around 1020 ^{0}C. The quenching sequence of HEA 2 - A2 was not as accurate as HEA 1 - A2 due to emergency situation.

Table 3. *Annealing treatments of test materials*

Material Code	Empherical formula	Temperature (^{0}C)	Time (Hours)	Cooling
HEA 1 – A1	$Al_{0.5}CoCrCuFeNi$	1080	72	Furnace normalizing
HEA 1 – A2	$Al_{0.5}CoCrCuFeNi$	1080	72	Quenching
HEA 2 – A1	$Al_{0,5}CoCrCuFeNiMo_{0,25}$	1080	72	Furnace normalizing
HEA 2 – A2	$Al_{0,5}CoCrCuFeNiMo_{0,25}$	1080	60*	Quenching

3.3 Microstructural Characterization

The optical microscope as shown in Figure 34a, Leica DM 2500, Leica microsystems CMS GmbH, Germany, is used for microscopic analysis of the polished epoxy-resin samples. The polar light emitted from polarizator differentiates the phases and interfaces. The optical zoom is limited to 100x. A field emission scanning electron microscope (FESEM), Zeiss ULTRA Plus (as shown in Figure 34b) with an acceleration voltage of 20kV is used. This is equipped with both secondary electron (SE) and back scattered electron (BSE) images were capturer, to visualize the phases and topographical features. Additionally,

the same FESEM is used for elemental mapping which is equipped with energy dispersive spectroscope (EDS).

The samples are machined into very small dimensions by the cutting machine. These samples are molded using epoxy resin. For a smooth surface profile, the samples are sequentially polished down to 0.1 µm grit alumina suspension finish. The etchant used is V2A with specifications as shown in Table 4.

Table 4. *Etching agent composition and specifications*

Etchant	Composition	Temperature	Time
V2A	100 ml water + 100 ml Hydrochloric acid +100 ml Nitric acid	50 - 60 ^{0}C	5-6 Sec

The etched samples are analyzed under optical microscope. For the field emission scanning electron microscope (FESEM) analysis, the samples are polished and not etched, but are carbon coated for conduction.

3.4 X-ray Diffraction

X-ray diffraction is used to identify the crystal structure of different phases in the HEAs. This technique also allows us to evaluate lattice parameter 'd' (inter atomic distance). The incident electron beams are diffracted by each atom, and are amplified by each other. Thus they form diffraction peaks at angles where Bragg's law is satisfied as shown in the Equation 3.1.

$$2dsin\theta = n\lambda \tag{3.1}$$

Where θ is incident angle, n is integer and λ is wavelength of X-ray beam. The lattice strain effect of HEAs leads to lattice distortion, this intrinsic lattice distortion decreases the intensities in the peaks. This intensity decrease is not because of plastic strain or amorphous phases [23].

The samples were cut and polished for XRD measurements. An X-ray diffractometer Panalytic Empyrean Multipurpose Diffractometer as shown in Figure 35 was used. The radiation conditions are 45 kV, 40 mA and Cu Kα radiation 1.5405 Å, with the 2θ scanning range from 20^0 to 120^0. The step size 2θ is of 0.0260^0 and total scan time of 25 seconds.

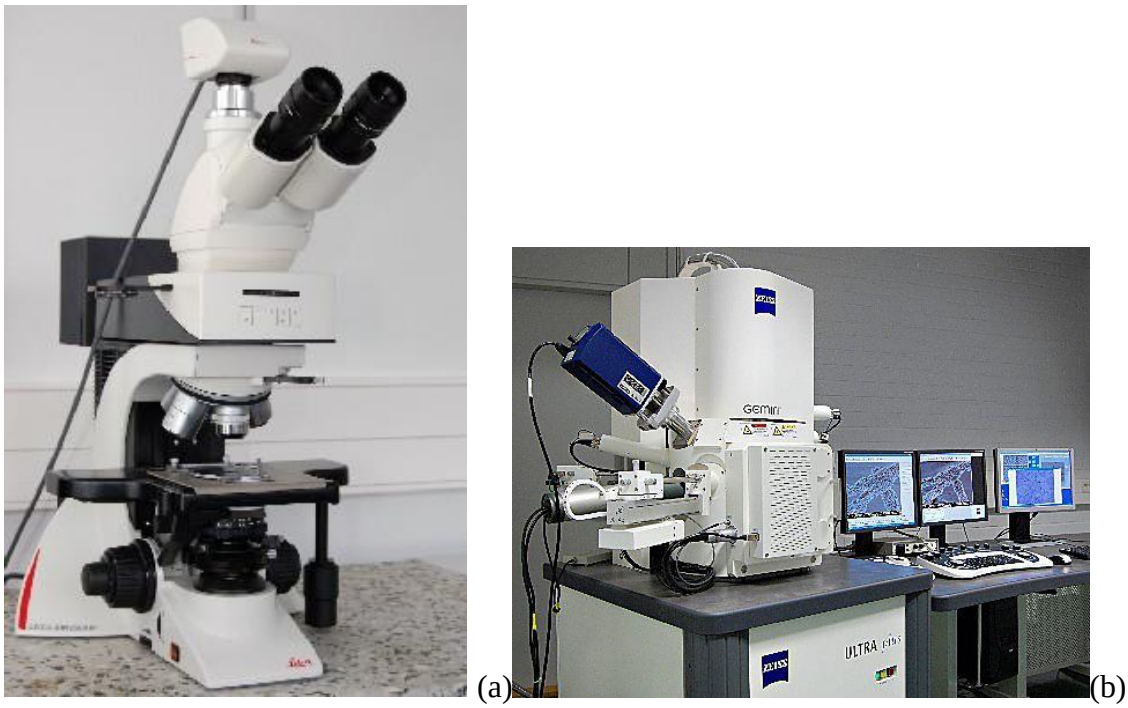

Figure 34. *(a) Optical microscope and (b) Field emission scanning electron microscope (FESEM) used for microscopic characterization*

Figure 35. *XRD (The Panalytical Empyrean Multipurpose Diffractometer)*

3.5 Hardness testing

The hardness of the experimental materials was tested using Vickers hardness tester Duramin – A300 hardness testing system as shown in Figure 36. The measurements were taken under a load of 3 kg-f (kilogram force) with the indentation time of 15 seconds.

Figure 36. *Hardness testing machine*

The Vickers hardness consists of indentation of the test material using diamond indenter. The angle of the pyramid is 136^0 between opposite faces. The load varies from 1- 100 kg-f. Vickers hardness is represented by HV. The value is determined by the Equation 3.2

$$HV = \frac{F}{A} = \frac{1.854\ F}{D^2} \tag{3.2}$$

Where F is applied force or load, A is area of cross section, and D is the average of the diagonals from the indentation. Table 5 gives a clear idea about the analysis of different test samples.

Table 5. *Vickers hardness testing*

Material Code	Empherical formula	Treatment	Force kg-f	Time (sec)	Number of imprints
HEA 1 - Reference	$Al_{0.5}CoCrCuFeNi$	Arc melting	3	15	7
HEA 1 - Vacuum	$Al_{0.5}CoCrCuFeNi$	Vacuum induction melting	3	15	7
HEA 1 - A1	$Al_{0.5}CoCrCuFeNi$	Annealing and normalizing	3	15	7
HEA 1 - A2	$Al_{0.5}CoCrCuFeNi$	Annealing and quenching	3	15	7
HEA 2 - Vacuum	$Al_{0,5}CoCrCuFeNiMo_{0,25}$	Vacuum induction melting	3	15	7
HEA 2 - A1	$Al_{0,5}CoCrCuFeNiMo_{0,25}$	Annealing and normalizing	3	15	7
HEA 2 - A2	$Al_{0,5}CoCrCuFeNiMo_{0,25}$	Annealing and quenching	3	15	7

3.6 High strain rate testing

High strain rate testing is done using Hopkinson split bar (HSB) technique. In this technique a specimen with uniform cross section and parallel surfaces is placed in between two long slender rods. These rods are called as incident bar and transmitted bar. The elastic loading conditions are used to measure stress-strain curve of the metallic materials. The technique can be used to test different loading conditions such as compression, tensile and torsion. This technique is used to determine high strain rate properties in the range of $10^2 – 10^4$ s^{-1}. This test can be performed at room temperature, cryogenic and high temperatures. The Figure 37 shows a schematic illustration of HSB system at Tampere University of Technology, Department of Material Science [83].

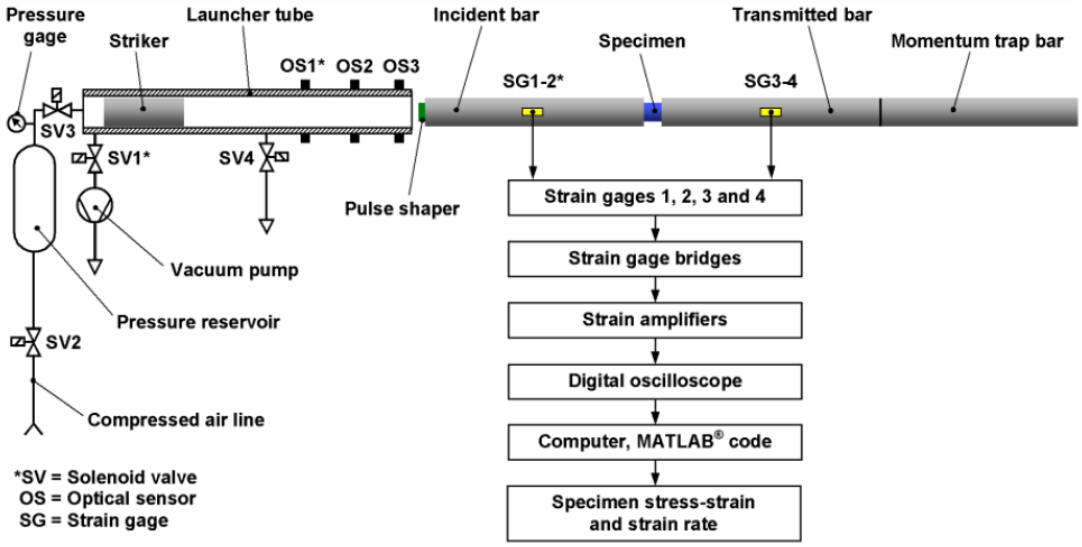

Figure 37. *Schematic illustration of Hopkinson split bar system as used in Tampere University of technology - Department of Material science* [83].

The specimen is placed in between the incident bar and transmitted bar. A small bar which is called the striker bar, is used to strike the incident bar as per pre calculated load provided by the pressure reservoir. When the striker bar strikes the incident bar, a stress wave is created into the incident bar, and the stress wave is partially reflected and partially transmitted to the surface of the specimen. The bar next to transmitted bar, called momentum bar is used to trap the residual transmission waves. This resists the residual stress pulse reflecting back to the transmitted bar [83]. The bars used in this specimen are made of high strength structural alloys maraging steel or a nickel alloy, which are in the elastic region during the test [84]. There are two strain gauges, each on incident and transmitted bar, which measures the transmission and reflected waves. These waves are used to evaluate the elastic strain displacement [83].

According to Gray et al [84], length and diameter of bars are directly dependent on the test criteria, such as maximum strain rate and strain levels. To readily separate incident

and reflected waves for data analysis, each bar should exceed the length to diameter ratio of ~20. The maximum strain rate can be achieved, with increase in the length to diameter ratio.

The HSB samples were cut using water jet cutting machine to the dimensions as mentioned in the Table 6. The sample dimensions were changed according to strain rates. The samples were cylindrical in shape.

Table 6. *Samples tested using HSB tests (L/D is length/diameter)*

Sample Code	Empherical formula	L/D (medium strain rate)	L/D (high strain rate)
HEA1 Reference	$Al_{0.5}CoCrCuFeNi$	3mm/3mm	3mm/3mm
HEA1 air	$Al_{0.5}CoCrCuFeNi$	8mm/8mm	6mm/6mm
HEA1 Vacuum	$Al_{0.5}CoCrCuFeNi$	8mm/8mm	6mm/6mm
HEA2 Air	$Al_{0,5}CoCrCuFeNiMo_{0,25}$	8mm/8mm	6mm/6mm
HEA2 Vacuum	$Al_{0,5}CoCrCuFeNiMo_{0,25}$	8mm/8mm	6mm/6mm

The test system consists of three high strength maraging steel bars (incident, transmitter and momentum bar). The diameter of bars is around 22mm and the length is 1200 mm or 1800mm. The striker bars are also of same diameter, but two different striker bars of 200mm and 400mm length are used as per the strain rates. The impact between the striker and incident bar is provided by the air gun. The air gun is comprised of a pressure container which provides pressure to the gun. The striker bar is launched through launcher tube. The vacuum pump retracts the striker rod and loads once again. There are also optical sensors to measure the velocity of the striker. The strain gauges attached to incident and transmitted bar collect the signals and send them to the oscilloscope. The function starting from pressurizing, shooting, and reading the data from oscilloscope is programmed [85].

Only the as-casted samples are used for HSB tests (as per the available resources and time), the test is carried out at room temperature. The strain rates of each sample is varied.

3.7 Corrosion testing

The electro-chemical behavior of all HEA2 (molybdenum rich), HEA1 reference sample and TWIP (twinning induced plasticity) steel are studied. The sample with a thickness of 500 mm were machined by the sample cutting machine and polished over 600-grit finish. Finally, the samples were rinsed with ethanol and dried. A conventional three-electrode cell in a single compartmental glass cell of 400ml capacity was used. All the potentials of corrosion testing were recorded with respect to silver chloride electrode as a reference electrode at 25 ^{0}C. The experimental setup is shown in Figure 38.

The silver chloride was connected via a Luggin capillary, the tip being very close to the surface of the working electrode to minimize the potential drop. Samples were immersed in the solution for 2 hours at open circuit preceding polarization. The potentio-dynamic scan was initiated at about -0.5V versus OCP (Open circuit potential), followed by scanning towards the final potential of 2.0 V, at a rate of 1 mV/s. A computerized Potentiostat model G750 series, and a Grammy Chem analyst from Grammy frame works were employed in the polarization tests.

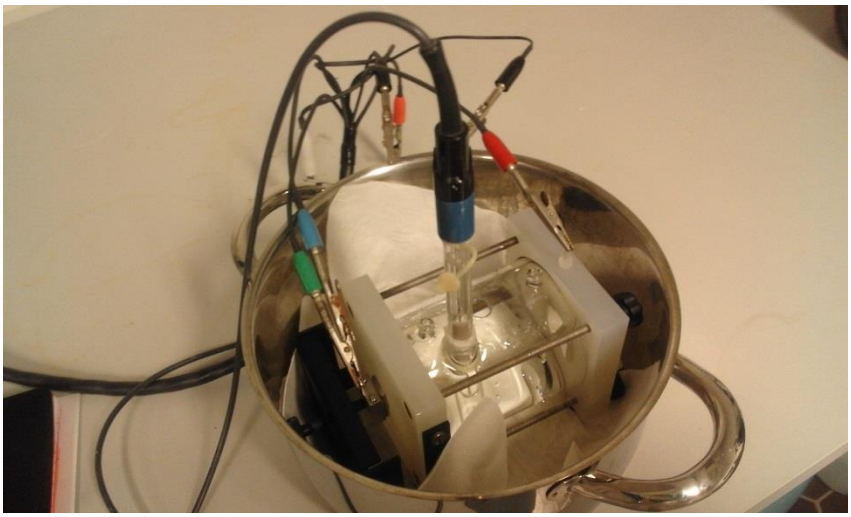

Figure 38. *Corrosion experimental setup of three electrodes cylindrical cell*

A TWIP (twinning induced plasticity steel) with composition as mentioned in Table 7 is used as a reference material for the comparison of corrosion properties. The 5% HNO_3 corrosion testing of TWIP steel was carried out by Hamada et al [86] to check the possibility of TWIP steel used to make storage vessels and pipes for HNO_3 processing media.

Table 7. *TWIP steel chemical composition*

Steel sample	C	Mn	Al	Cr	Si	Ni	Fe
TWIP - Steel	0.2725	30	4.53	4.14	0.433	0.06	60.57

The experimental conditions are varied with respect to tests done by done by Hamada et al [86]. The experimental time is increased from 60 minutes to 2 hours.

4. RESULTS AND DISCUSSION

4.1 Materials and Phase prediction

The thermodynamic parameters of the experimental HEAs are evaluated based on Equations 2.9, 2.10, 2.11 and 2.14. These values predict the phases and solid solution stability based on the theoretical prediction as explained in section 2.3.

Table 8. *Thermodynamic parameters of experimental HEAs*

Alloy Code	Empherical formula	VEC	Melting point T_m (Deg Celsius)	ΔH_{mix} (kJmol^{-1})	ΔS_{mix} (JK^{-1} mol^{-1})	Ω	δ%
HEA 1	$Al_{0.5}CoCrCuFeNi$	8.27	1410	-1.52	14.70	16.30	3.96
HEA 2	$Al_{0.5}CoCrCuFeNiMo_{0.25}$	8.17	1463	-1.32	15.50	16.70	4.50

The melting point (T_m) is defined by the rule of mixtures, evaluating the following equation. The effective melting point of HEA1 is approximately 1410 ^{0}C. The thermal analysis of $Al_{0.5}CoCrCuFeNi$ [18] shows that the liquidus temperature of $Al_{0.5}CoCrCuFeNi$ is nearly 1362 ^{0}C, which is within the variance of 50 ^{0}C due to formation of copper-rich phase which softens the whole alloy at 1153 ^{0}C. Similarly, the newly casted $Al_{0.5}CoCrCuFeNiMo_{0.25}$ has a melting temperature of 1463 ^{0}C by the mixing rule. Thus the thermal analysis is required to define the true melting point of the material.

Similarly, other parameters such as, VEC, Ω and δ% evaluated as given in Table 8 can be used to predict the phases. Comparing the values of δ and Ω of both the alloys with Figure 11 says that both the alloys forms solid solutions. The VEC values predict that, both the alloys form multiphase solid solutions. The different phases formed are known through the microstructural characterization which is explained in further discussions.

4.2 Microstructural characterization

The microstructural analysis is comprising of two individual techniques, the samples are molded into epoxy resin, polished and etched in V2A at 50-60^{0}C as mentioned in chapter 3.3.

Additionally, SEM + EDS analysis are carried out by the sample preparation similar to optical microscopy, but there is no etching. Instead the same is ultrasonically cleansed in ethanol and then desiccated for 1 day.

4.2.1 Optical Microscopy

The images are taken through Leica DM 2500 optical microscope. The list of samples analyzed are presented in the following order as shown in Table 9.

Table 9. *List of samples and their treatments*

Material Code	Empherical formula	Treatment
HEA - Reference	$Al_{0.5}CoCrCuFeNi$	Arc melting
HEA 1 - Vacuum	$Al_{0.5}CoCrCuFeNi$	Vacuum induction melting
HEA 1 - A1	$Al_{0.5}CoCrCuFeNi$	Annealing and normalizing
HEA 1 - A2	$Al_{0.5}CoCrCuFeNi$	Annealing and quenching
HEA 2 - Vacuum	$Al_{0,5}CoCrCuFeNiMo_{0,25}$	Vacuum induction melting
HEA 2 - A1	$Al_{0,5}CoCrCuFeNiMo_{0,25}$	Annealing and normalizing
HEA 2 - A2	$Al_{0,5}CoCrCuFeNiMo_{0,25}$	Annealing and quenching

The micrographs were taken with different magnifications. The scale bar shows the magnification of the images. The optical micrographs of HEA – reference material are shown in the Figure 39. Since the etching agent is V2A at nearly 60 ^{0}C, we can see the over etched spots.

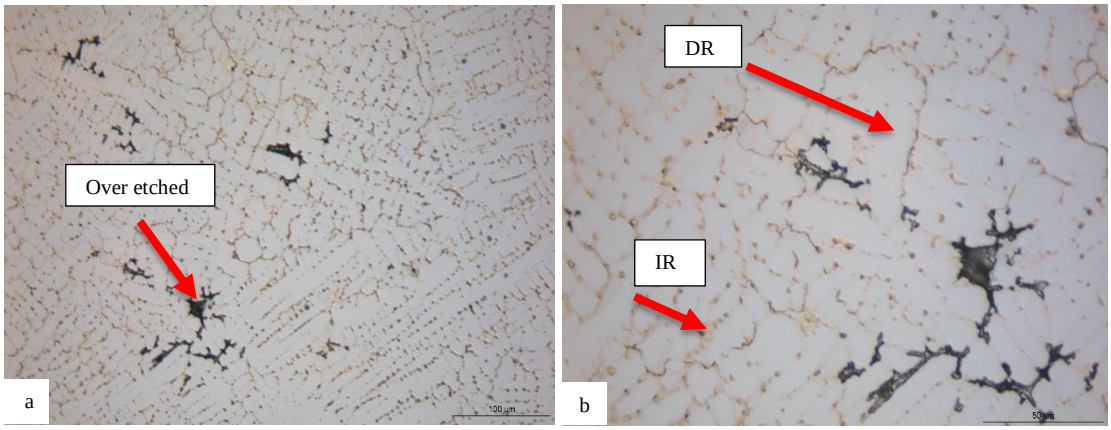

Figure 39. *HEA – reference micrograph with scales (a) 100µm and (b) 50µm*

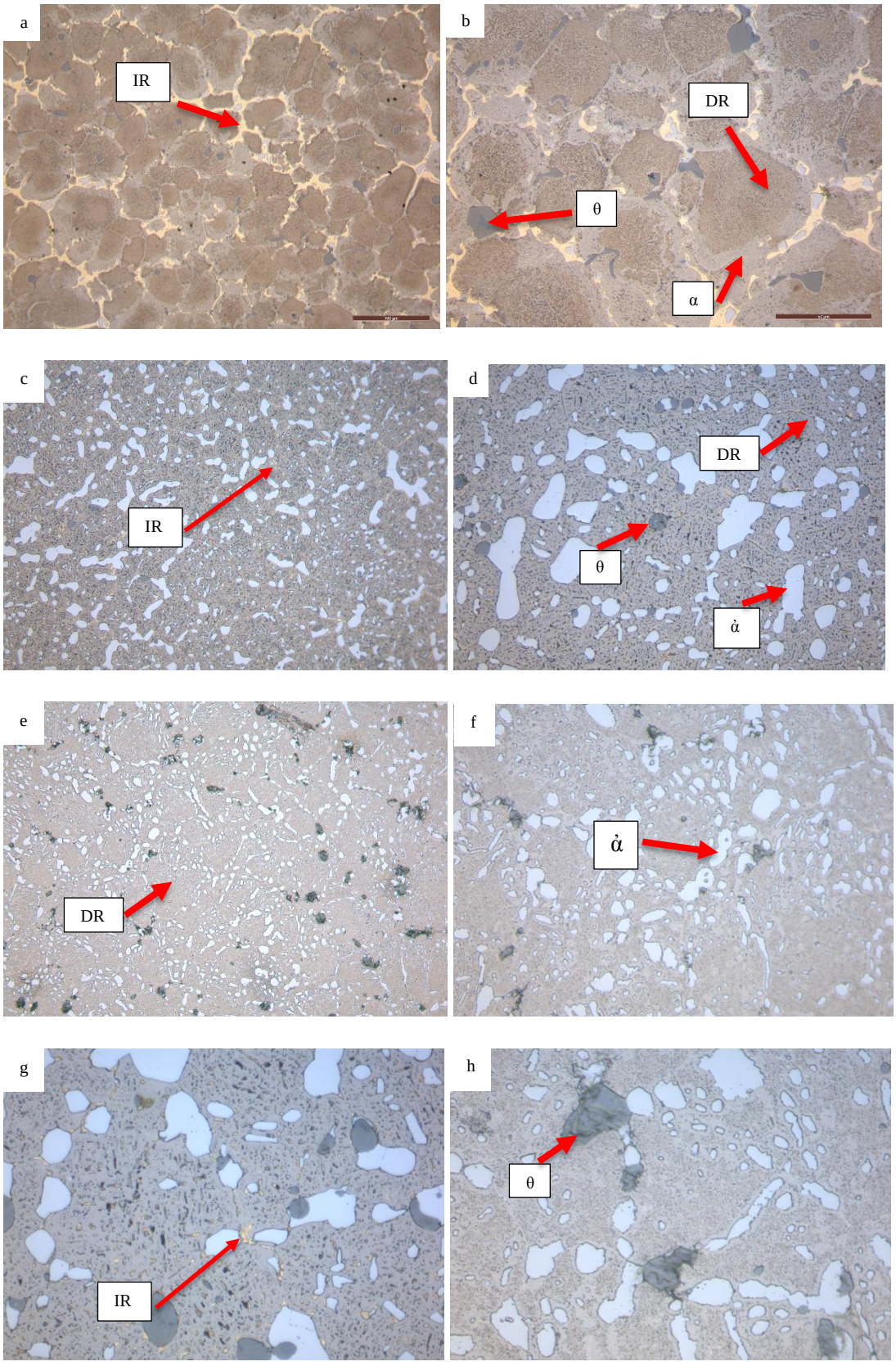

Figure 40. *Optical micrographs of HEA 1 Vacuum scale (a) 100µm (b) 50µm; HEA 1 A1 (c) 100µm (d) 50µm (g) 20µm; HEA 1 A2 (e) 100µm (f) 50µm (h) 20µm.*

The Figure 39 shows that the microstructure of HEA – reference sample is dendritic. There are mainly two regions inside the microstructure, the Figure 39b shows marked regions the IR (inter dendritic) and DR (dendritic region). The micrographs are similar to the microstructures as mentioned in Murthy et al [1]. Since the composition is already analyzed by many researchers [18], [57], the IR region can be regarded as copper rich phase and DR region is defined as the matrix phase which has less copper content. The etching agent we used is V2A which was found to be very strong, and had eroded some part of the surface. According to Figure 39a, the dark spots are over etched spots, which is the copper phase. Additionally, the polishing also leads to surface erosion since the hardness of phases are varied. When practicing with other samples, the etching exposure is reduced to control the over etching.

The HEA1 has the same composition as HEA- reference sample. Melting was done in the induction furnace. The cast is initially done in open atmosphere and the ingot is re-melted in vacuum condition. The vacuum casted sample's optical micrographs are shown in the Figure 40 a, b. The vacuum casted samples are homogenized by annealing treatment. The optical micrographs of two different types of annealing treatments are shown in Figures 40c - h.

The Figure 40 shows that the microstructure of HEA 1 is completely different when compared to HEA 1 – reference sample. The vacuum casted sample microstructures (Figure 38a, b) are comprised of IR and DR regions similar to the HEA- reference microstructure, but surprisingly two new phases θ and α are also observed. When the HEA1 A1 is annealed for 3 days, the two different treatments (normal cooling and quenching) show the disappearance of IR region which is comprised of copper.

The quenched sample (HEA1 A2) has no IR phase visible. The new phase which is formed after annealing and quenching is named as ȧ-phase (which is expected to have similar composition as α phase). The slower cooling rates after annealing (as shown in Fig. 40c, d, g) shows matrix phase or DR with some dark spots which are suspected to be distribution of θ-phase in the matrix.

The quenching after annealing (HEA1 A2) have shown different phases similar to HEA1 A1. The major change in the HEA1 A2 is, the IR totally disappeared. The θ-phase is not distributed over matrix, but is segregated. The ȧ phase is also distributed with smaller sizes. The elemental mapping through EDS of all the phases can give us a clear idea of the phase compositions.

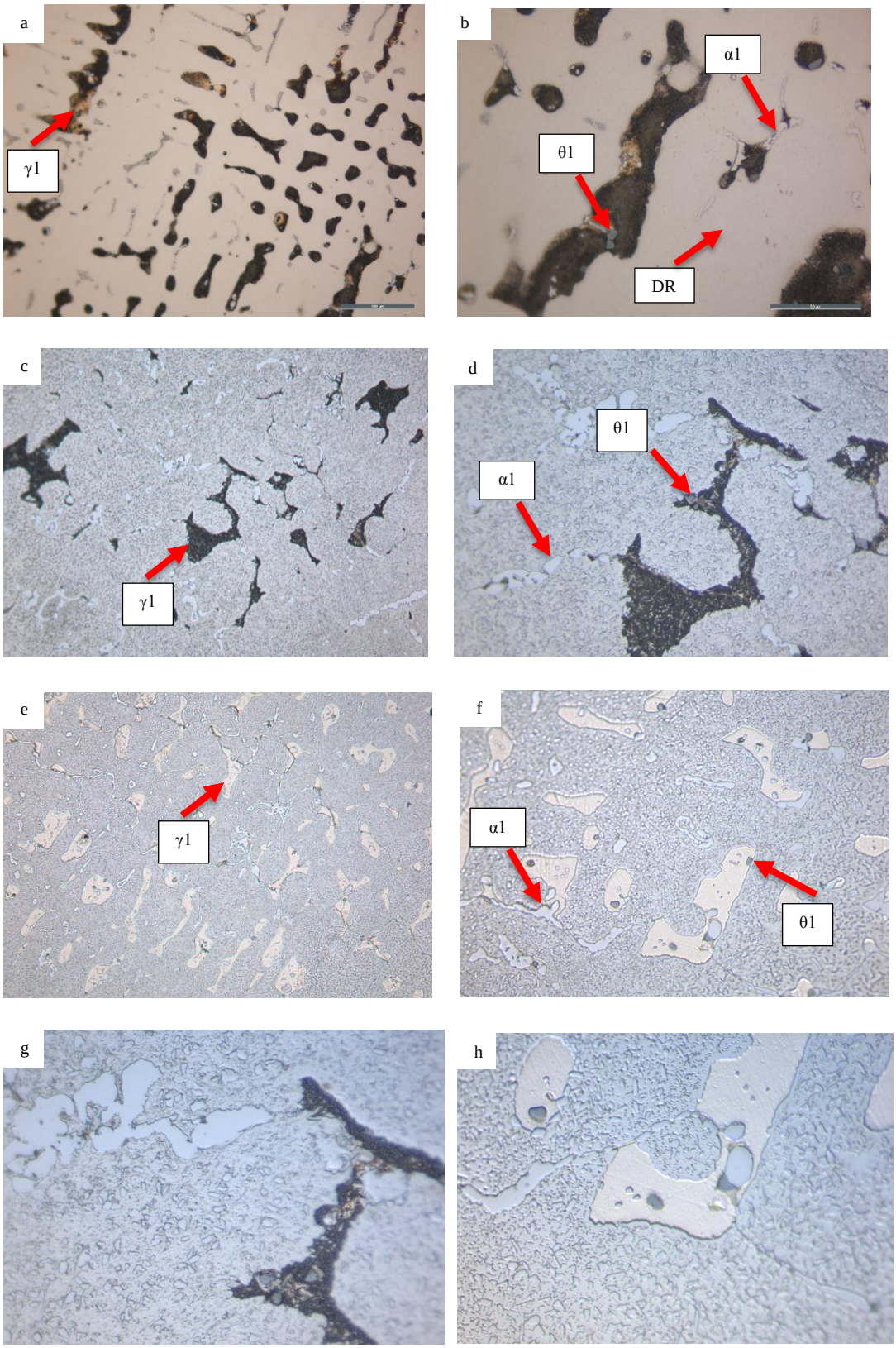

Figure 41. *Optical micrographs of HEA 2 vacuum scale (a) 100µm (b) 50µm; HEA 1 A1 (c) 100µm (d) 50µm (g) 20µm; HEA 1 A2 (e) 100µm (f) 50µm (h) 20µm.*

The HEA 2 sample is casted under similar conditions as HEA 1, but there is some addition of molybdenum. The samples analyzed are shown in Figure 41. The optical micrographs of vacuum casted samples are shown in Figure 41 a, b. The images of annealed and normalized samples (HEA 2 A1) are shown in Figure 41 c, d, g. The annealed and quenched samples (HEA 2 A2) are shown in 41 e, f, h.

The Figure 41 shows that the microstructure has two different phases or IR regions and a DR region. The two different visible phases are defined as γ1 and α1 phases. There is also a dark region which resembles the precipitate similar to HEA 1. This precipitate is defined as θ1. Considering the Figure 41a and 41b of the vacuum casted sample (HEA2 – vacuum), the dendritic region or matrix phase is very uniform. In the annealed samples both have distributed phases inside the matrix.

The current alloys can be compared with the analysis of similar HEA ($AlCoCrCuFeNiMo_x$) studied by Zhu et al[42]. This HEA ($AlCoCrCuFeNiMo_x$) has shown similar microstructural features. However, the images shown in the study are back scattered electron SEM images. The phases of HEA2 can therefore be predicted with SEM images and EDS analysis.

4.2.2 Scanning Electron Microscopy and EDS analysis

The FESEM (Field emission scanning electron microscopy) micrographs of HEAs as listed in Table 8 are taken through FESEM (Zeiss ULTRA Plus). Similar micrographs are analyzed with EDS in confined area for the elemental distribution analysis, which is same area as the SEM images.

The Figure 42 shows the SEM secondary electron signal image of HEA – reference sample and elemental maps of the comprising elements. Table 10 shows elemental compositions of different phases present in the alloy. SEM micrographs shows a similar structure as seen in optical micrograph. The microstructure comprises of IR and DR. The IR region is dominated by copper and also has a high percentage of aluminum. The microstructure and elemental analysis is almost matching the analysis as studied by Gones et al [87], with the same alloy composition. The formation of copper phase is because, copper has greater difference in enthalpy of mixing (ΔH_{mix} value) with other elements and lowest ΔH_{mix} value with aluminum which is -1 kJ/mol [88]. Nickel has almost similar difference in ΔH_{mix} with all other elements. This causes it to distribute uniformly throughout the structure. There is no precipitate found in the microstructure. Both the phases are FCC as per the studies [87].

Similarly, Figures 43, 44 and 45 show the SEM back scattered micrographs of HEA1 – vacuum cast, HEA1 A1 and HEA1 A2 samples respectively. The SEM micrographs show the presence of 4 different phases, which are also marked in the optical micrographs of HEA1 (Figure 40). The EDS analysis of all samples showed difference in distribution of

elements. This distribution gave a clear idea about the compositions of different phases. The most interesting thing to notice is that new phases are formed due to inclusion of some new elements in such as sulphur, silicon and oxygen. The θ-phase is comprised of chromium and sulphur in larger content. This phase looks more like an amorphous phase based on the surface morphology when seen in secondary electron images (a topographical view).

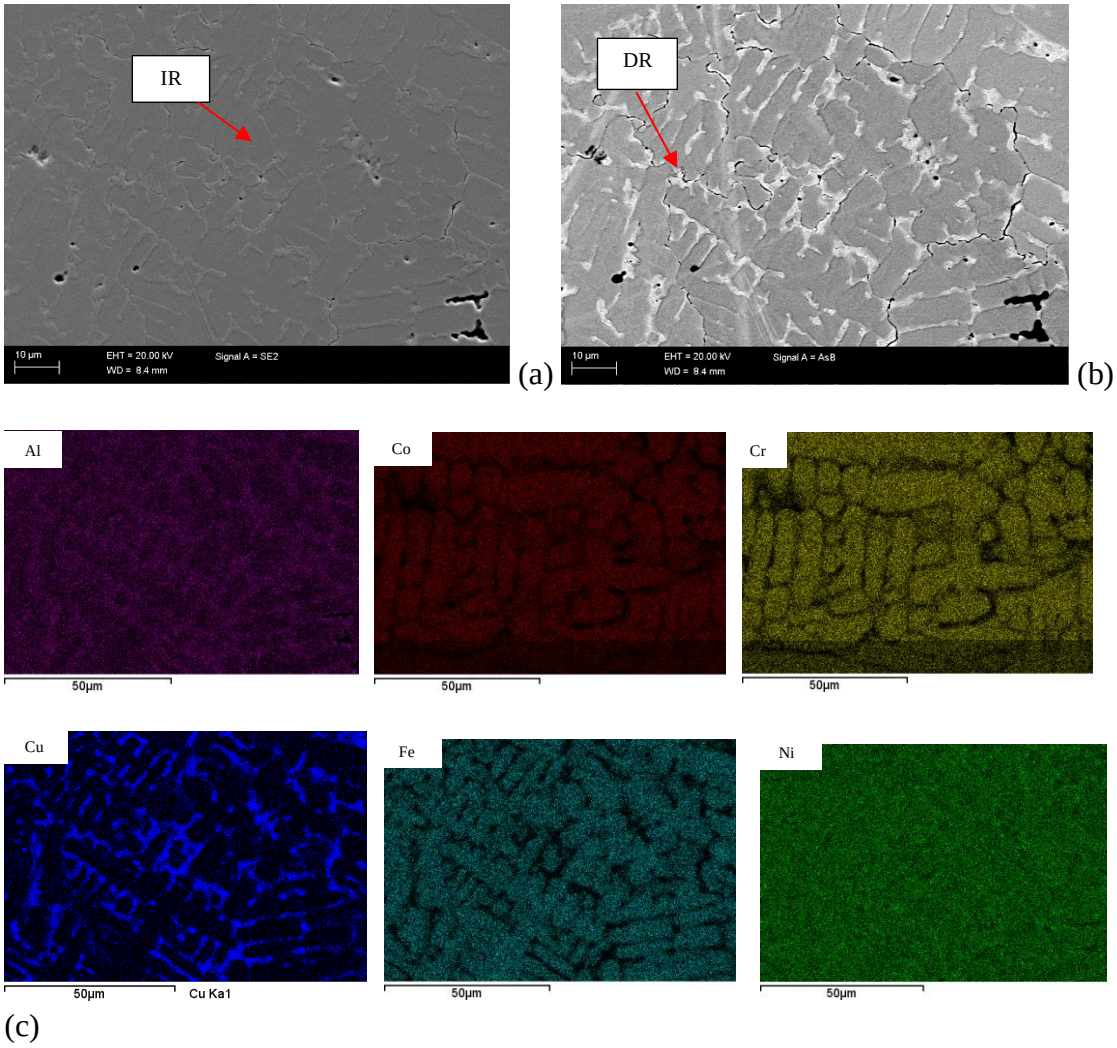

Figure 42. *(a) FESEM micrographs of HEA – reference sample (a) secondary electron, (b) back scattered, and (c)EDS analysis of individual element.*

Table 10. *Phase compositions in atomic % of HEA - reference determined using EDS.*

HEA REF	***Al***	***Cr***	***Fe***	***Co***	***Ni***	***Cu***
IR	13	7	7	6	13	50
DR	6	21	20	29	15	8
Total area*	9	19	18	18	18	17

* EDS analysis total area of the SEM micrographs (Figure 42 a)

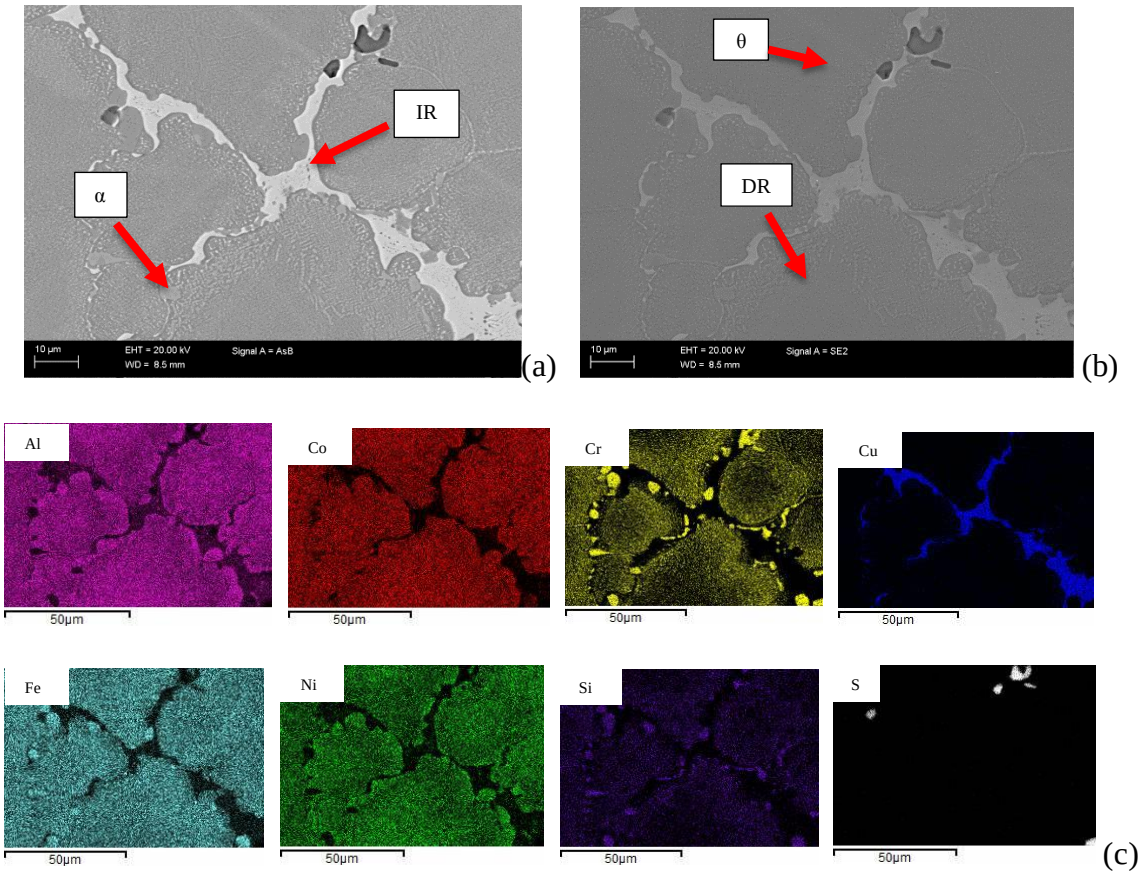

Figure 43. *FESEM micrographs of HEA 1– vacuum sample (a) back scattered, (b) secondary electron, (c) EDS analysis of individual elements.*

Table 11. *Phase compositions in atomic % of HEA 1 - Vacuum determined using EDS.*

HEA 1 Vacuum	***Al***	***Cr***	***Fe***	***Co***	***Ni***	***Cu***	***Si***	***S***
IR	21	1	2	3	6	65	0	0
DR	33	10	12	17	15	9	3	0
α	6	47	23	9	3	2	10	0
θ	0	45	0	0	0	0	0	53
Total area*	26	17	12	14	12	15	4	0

* EDS analysis total area of the SEM micrographs (Figure 43 a)

From the phase compositions it is observed that oxygen is also present in minor compositions in IR, DR and α or ȁ phases. The α and ȁ phases have similar compositions, however they look different when observed in optical micrograph. The α or ȁ phase is comprised of chromium, iron and silicon as major components. This can form a different crystal lattice which can possibly be detected using X-ray diffraction. The remaining IR is rich in copper, similar to HEA - reference. The DR has all elements with atomic % similar to HEA – reference. Thus the phases are expected to be FCC. However, the aluminum % is increased in DR and IR when compared to HEA- reference. Further XRD analysis can clearly explain the different crystal structures possible.

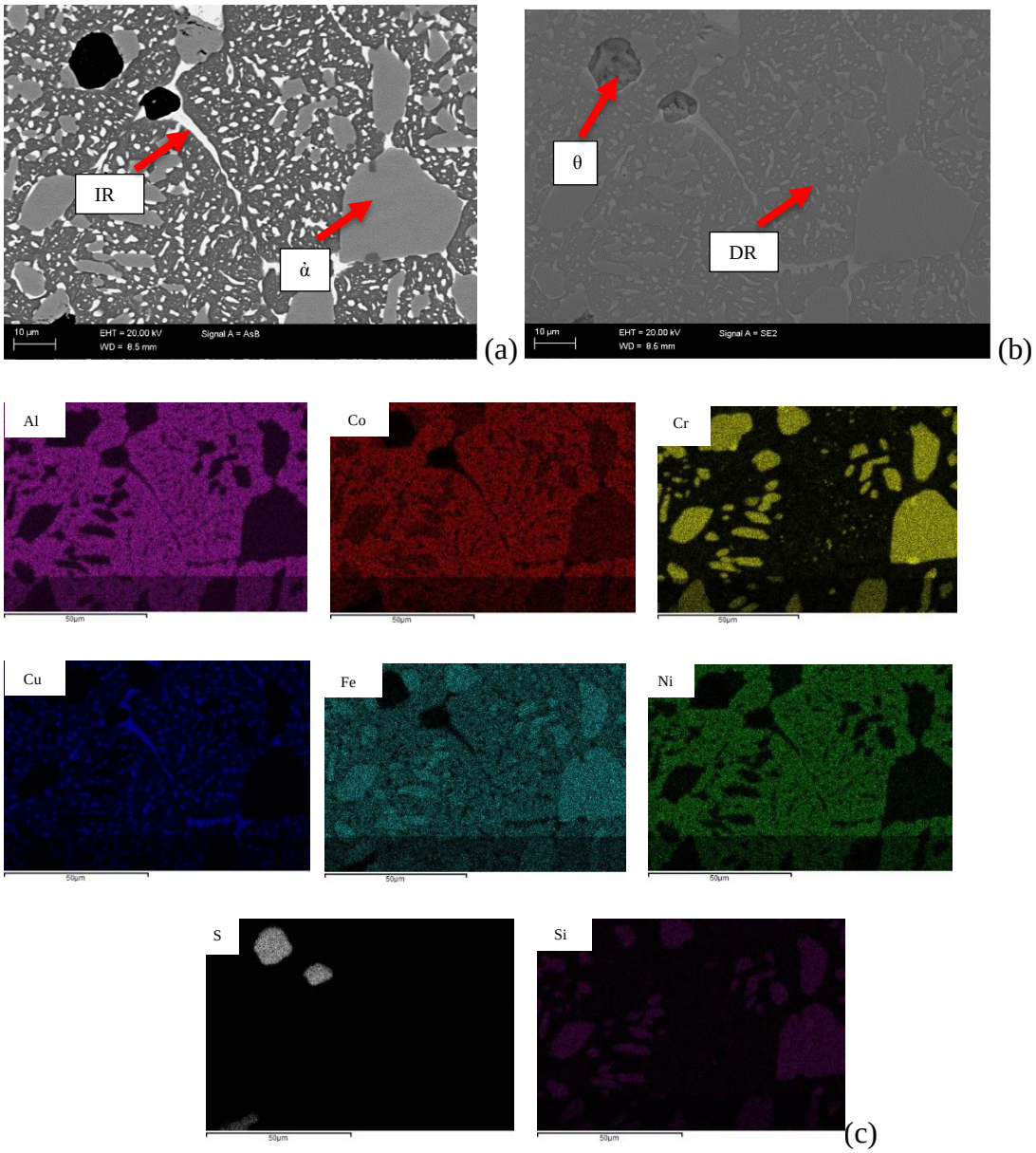

Figure 44. *FESEM micrographs of HEA 1– A1 sample (a) back scattered, (b) secondary electron, and (c) EDS analysis of individual elements.*

Table 12. *Phase compositions in atomic % of HEA 1- A2 determined using EDS.*

HEA 1 A1	***Al***	***Cr***	***Fe***	***Co***	***Ni***	***Cu***	***Si***	***S***
IR	16	0	1	3	2.2	75	0	0
DR	39	4	11	18	17	9	1	0
α̇	2	53	20	9	1	0	13	0
θ	0	43	0	0	0	0	0	53
SEM image area Total*	26	16	11	13	11	14	4	2

* EDS analysis total area of the SEM micrographs (Figure 44 a)

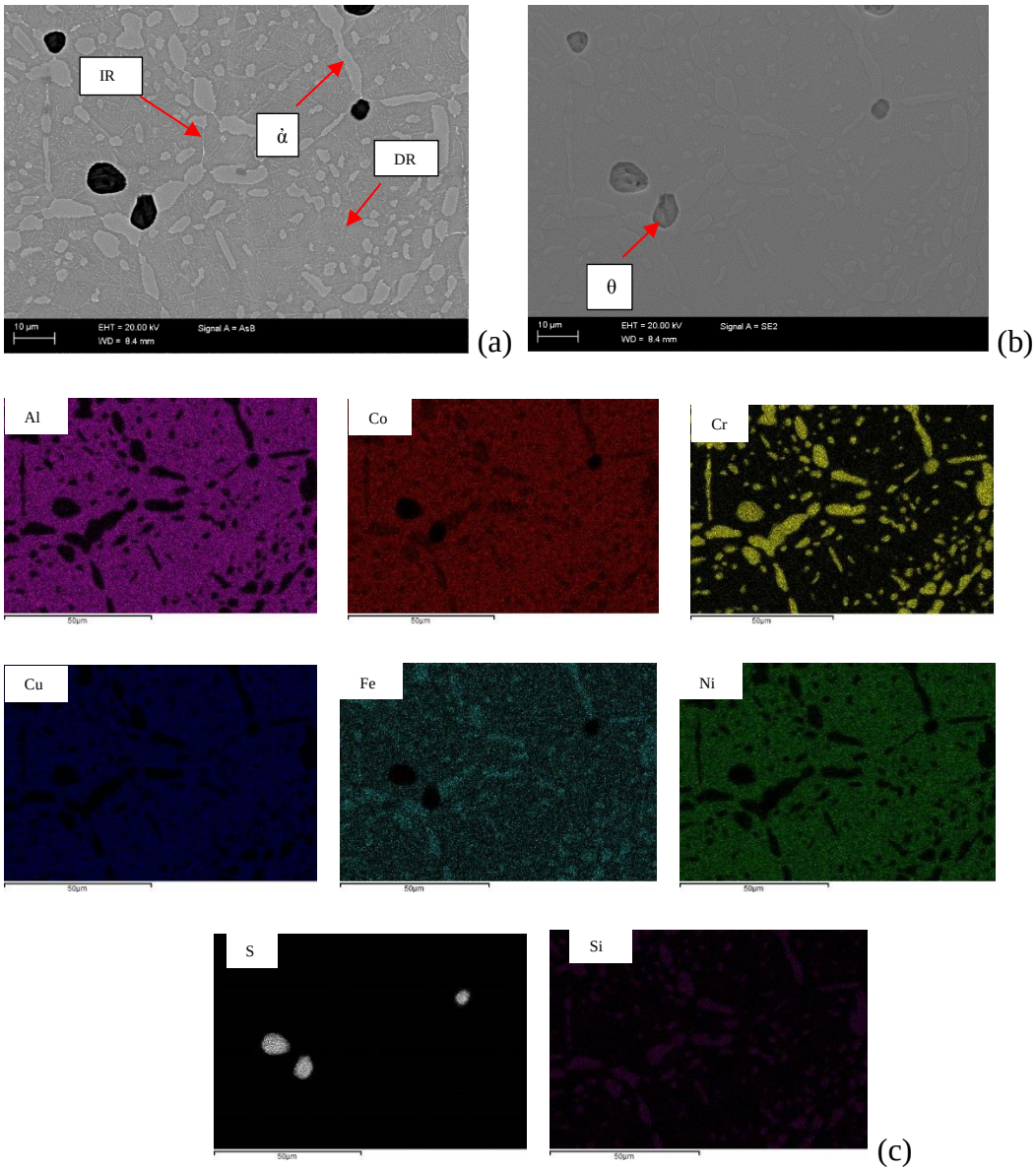

Figure 45. *FESEM micrographs of HEA 1– A2 sample (a) back scattered, (b) secondary electron, and (c) EDS analysis of individual elements.*

Table 13. *Phase compositions in atomic % of HEA 1- A2 determined using EDS.*

HEA 1 A2	AL	CR	FE	CO	NI	CU	SI	S
IR	24	25	14.	13	10	9	4	0
DR	33	6	10	16	15	17	2	0
α̇	2	53	20	10	1	0	13	0
Θ	1	42	0	0	0	0	0	53
AREA TOTAL *	27	14	12	14	13	14	4	0

* EDS analysis total area of the SEM micrographs (Figure 45 a)

The α phase before annealing doesn't have a phase boundary, but is very close to or almost mixed with IR phase. The annealing treatment showed that α phase (similar to ȧ phase) from HEA1-vacuum has started to stabilize. After quenching the ȧ phase (chromium rich) is stabilized with boundaries as shown in SEM back scattered images. The difference can be easily seen in three EDS maps of chromium (Figures 43c, 44c and 45c) which is yellow in color.

The annealing treatment started distribution of all the major component elements, but chromium is segregating at θ and α or ȧ phases. Copper is distributed in HEA1 A2 throughout the matrix, which shows that copper phase is not stable at the higher temperatures. This is clearly shown in the copper elemental map from Figure 45c and also chemical composition of copper rich phase IR (as shown in Table 12). The copper rich phase is formed when the cooling is done slowly like in HEA1 A1.

Considering these additional phases, it can be concluded that the alloy was casted with miscalculation of input (increase in aluminum content) and contamination. These contaminations may be mixed from raw material, furnace lining or mold lining. This contamination and increase in aluminum content has a major impact in the phase formation. The mechanical properties like hardness and ductility can be known by hardness and compression testing, which is explained in Chapter 4.4 and 4.5.

The Figures 46, 47, 48 show the SEM micrographs and EDS analysis of HEA2 – vacuum, HEA2- A1 and HEA2 – A2 samples respectively. The SEM micrographs show the presence of 4 different phases, which are marked in the optical micrographs of HEA2 (Figure 41). The EDS analysis of every treatment shows a small difference in distribution of elements. This distribution gives a clear idea about the compositions of different phases. The elemental mapping has shown the presence of inclusions or impurities which were mixed during casting. Impurities such as sulphur, silicon, and traces of titanium, manganese and zirconium are found. These elements are probably from the refractory lining inside the furnace or casting mold. Additionally, there is oxygen found, which is approximately 1%. This is because the first casting done was in open air (normally HEAs are casted in vacuum conditions to avoid air or oxygen inclusions).

The FESEM micrographs of HEA2 shows the presence of two main phases α1 and γ1. The brightest phase which is seen in backscattered image in all the Figures 46a, 47a, and 48a is the α1-phase, and a little darker phase which is marked in same figures is γ1-phase. We also found a dark precipitate – θ1, which is sulphur rich. This θ1-phase is similar as θ-phase in HEA1.

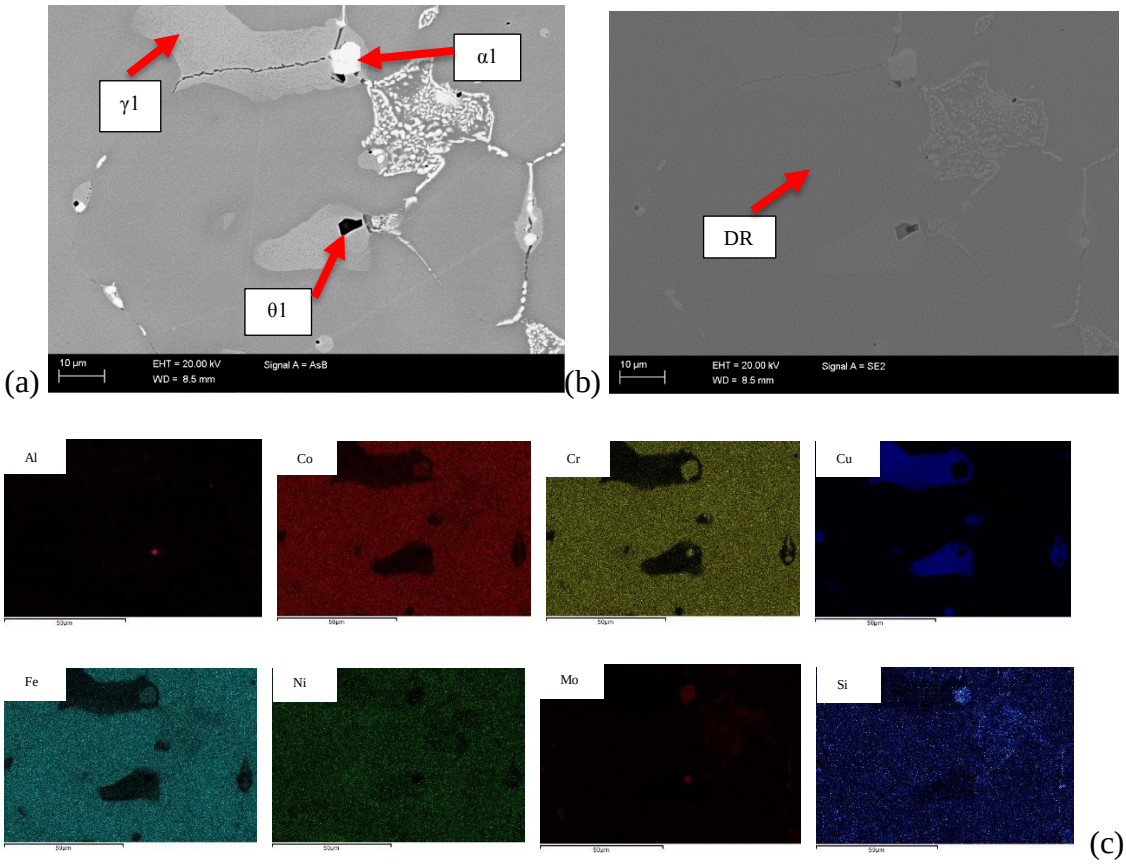

Figure 46. *FESEM micrographs of HEA 2– vacuum sample (a) back scattered, (b) secondary electron, and (c) EDS analysis of individual elements.*

Table 14. *Phase compositions in atomic % of HEA 2- vacuum determined using EDS.*

HEA 2 Vacuum	***Al***	***Cr***	***Fe***	***Co***	***Ni***	***Cu***	***Si***	***Mo***	***S***	***Zr***	***Mn***
DR	5	20	25	19	16	8	1	5	0	0	0
γ1	13	1	4	3	13	64	0	0	0	0	0
α1	1	23	16	14	7	2	7	27	0	0	0
θ1	4	25	0	0	1	6	0	0	46	4	15
Total	7	17	20	16	15	15	1	5	0	0	0

* EDS analysis total area of the SEM micrographs (Figure 44 a)

The EDS analysis of HEA2-vacuum sample shows that the molybdenum and copper atoms are concentrated only in certain areas which turned to be α1 and γ1 phases respectively. Similar to HEA 1 alloy the nickel atoms are distributed throughout the phases except α1-phase. The aluminum is distributed throughout the area, but mostly concentrated in θ1- phase.

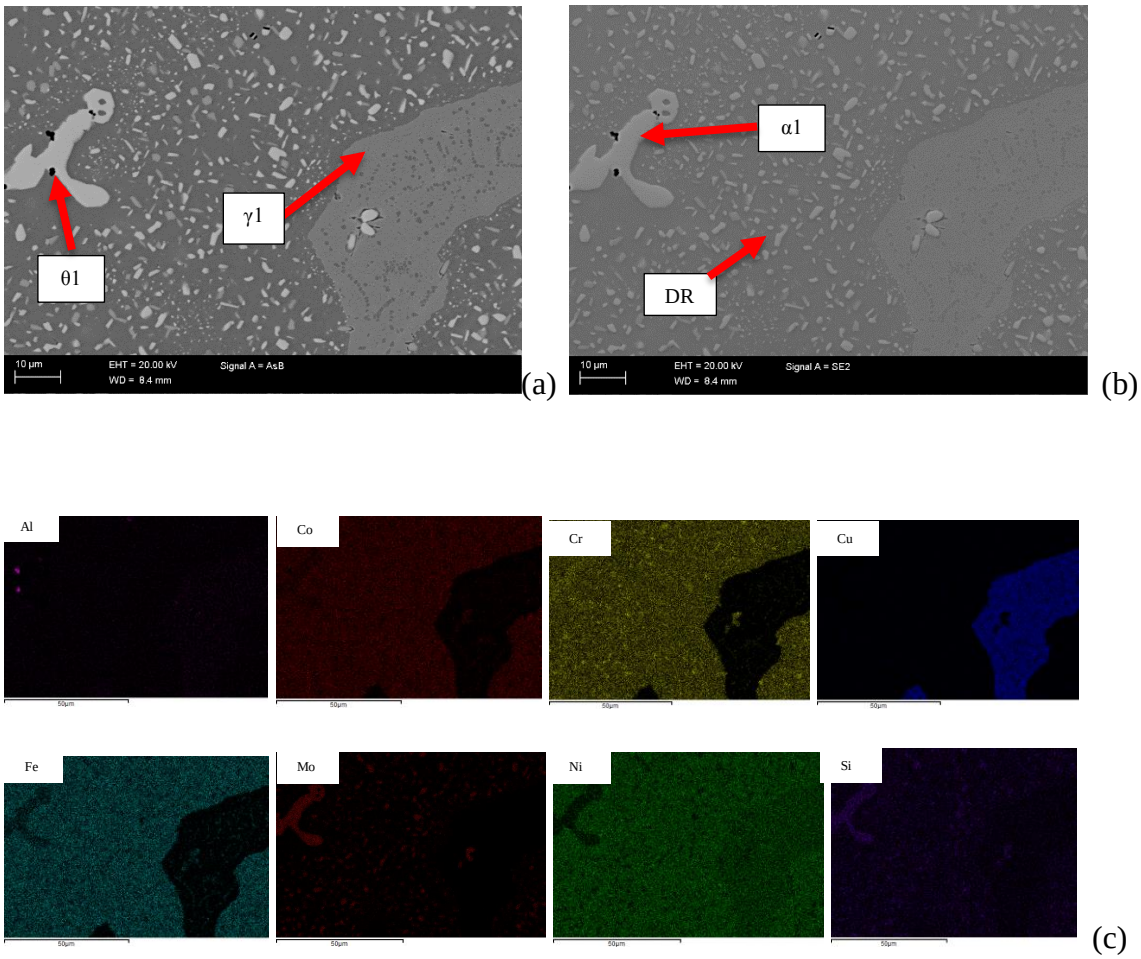

Figure 47. *FESEM micrographs of HEA 2– A1 (a) back scattered, (b) secondary electron, and (c) EDS analysis of individual elements.*

Table 15. *Phase compositions in atomic % of HEA 2- A1 determined using EDS.*

HEA2 - A1	***Al***	***Cr***	***Fe***	***Co***	***Ni***	***Cu***	***Si***	***Mo***	***S***
DR	6	19	25	19	18	8	1	3	0
γ1	12	1	3	3	14	65	0	0	0
α1	1	25	18	16	6	0	6	25	0
θ1	30	11	7	5	5	6	0	4	10
Total	6	17	22	16	16	15	1	5	0

* EDS analysis total area of the SEM micrographs (Figure 45 a)

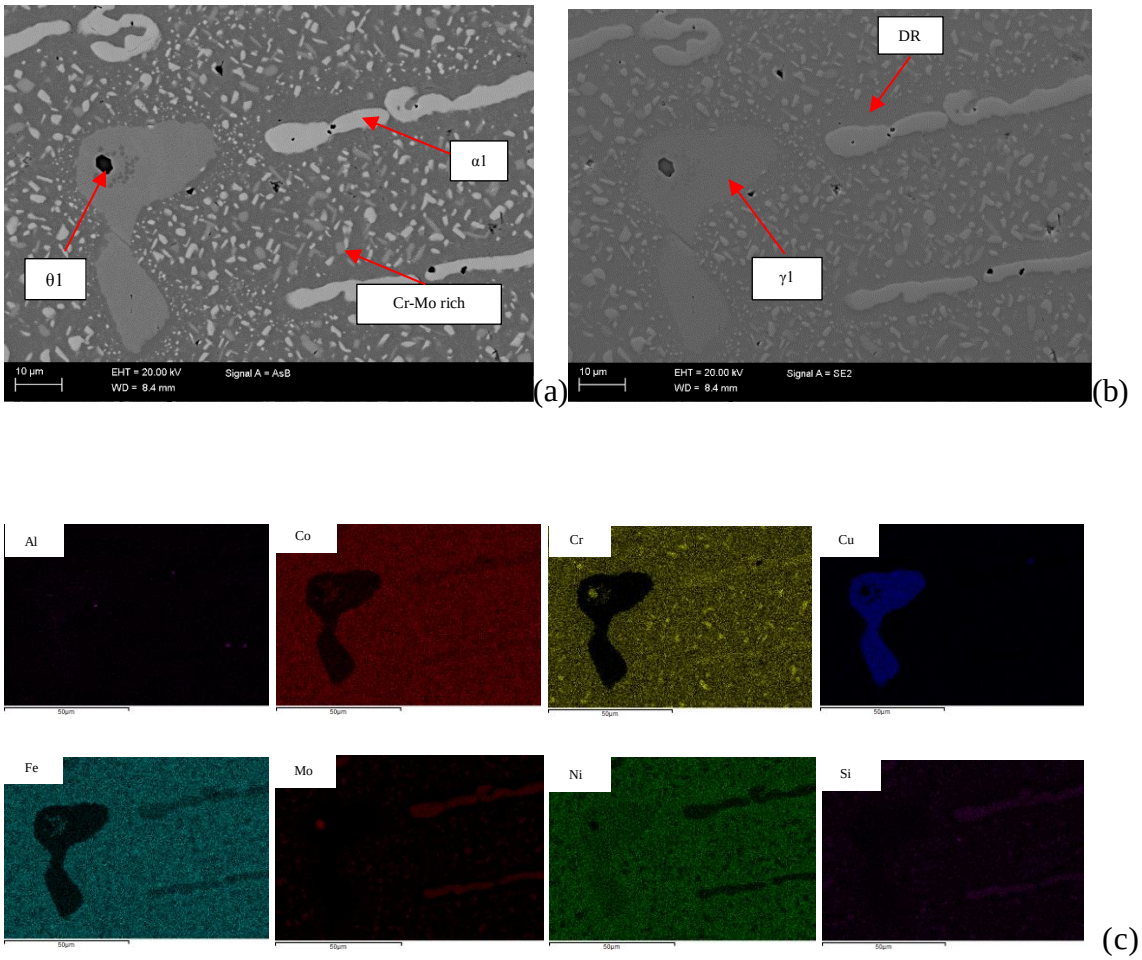

Figure 48. *FESEM micrographs of HEA 2– A2 (a) back scattered, (b) secondary electron, and (c) EDS analysis of individual elements.*

Table 16. *Phase compositions in atomic % of HEA 2- A2 determined using EDS.*

HEA 2 A2	*Al*	*Cr*	*Fe*	*Co*	*Ni*	*Cu*	*Si*	*Mo*	*S*	*Zr*	*Mn*
DR	7	18	25	19	19	13	0	2	0	0	0
γ1	11	1	3	3	13	65	0	0	0	0	0
α1	5	30	21	19	7	0	7	30	0	0	0
Cr- Mo rich	1	36	21	17	6	0	3	12	0	0	0
θ1	2	28	0	0	0	2	0	0	58	5	21
Image Area Total	6	20	24	19	17	11	2	7	0	0	0

* EDS analysis total area of the SEM micrographs (Figure 46 a)

Comparing the SEM micrographs of HEA2-vacuum and HEA2-A1, it is seen that in HEA2-A1 the matrix phase is changed and the stability of α1-phase is increased. Also the % atomic composition (table 14) and elemental map show that silicon concentration is increased in α1-phase. The repulsion is shown between the α1-phase and nickel. The γ1-phase is comprised mostly of copper, and a small percentage of nickel and aluminum. Molybdenum is completely absent in the γ1 phase. Iron is mostly concentrated in the matrix.

The SEM micrographs of HEA2 – A2 shows more stabilization of α1-phase. The backscattered image (Figure 48a) shows smaller white blocky shaped phases in the matrix. The elemental map of chromium shows high concentrations in these white blocky shapes. The spot analysis shows that these white blockys are rich in molybdenum and chromium having almost equivalent composition to α1-phase. Additionally, as compared to HEA2-vacuum and HEA2 –A1, the nickel element is distributed throughout the area, but had a repulsion with α1-phase.

The presence of sulphur and molybdenum elements shows same EDS maps, but can be easily differentiated. The sulphur rich phase (θ1) is darker in backscattered image and the molybdenum rich phase (α1) is the brightest. The brightness in the images is directly proportional to atomic mass, which is a property of an element. The sulphur concentration is similar to molybdenum concentration in elemental mapping as shown in Figure 49a and b. The energy peaks in the EDS spectrum superimpose on each other as shown in Figure 47c. The k_α peak of sulphur superimposes or overlaps with the peak of L_α of molybdenum.

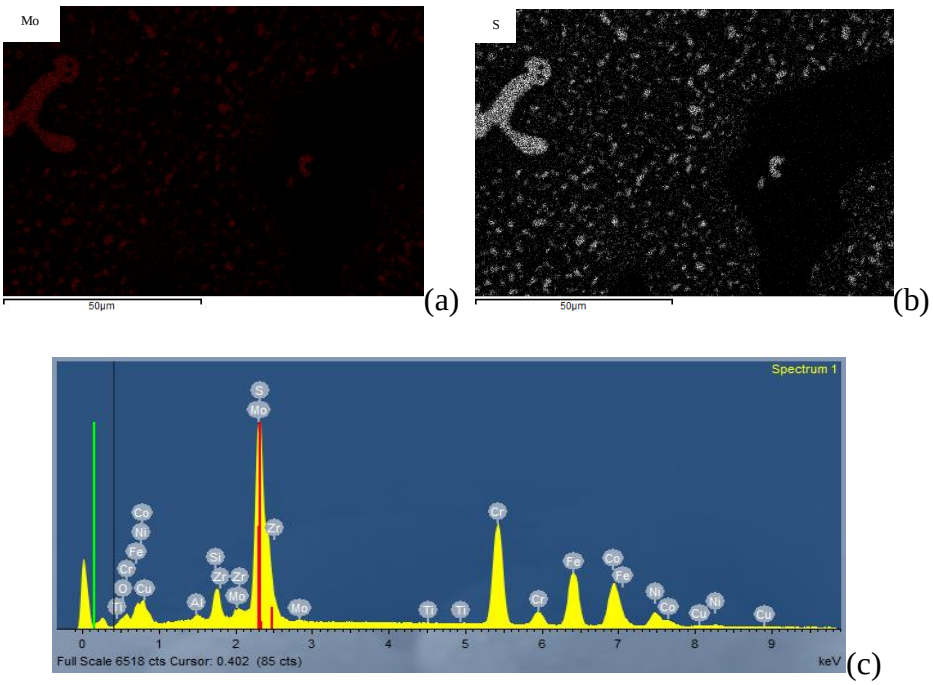

Figure 49. *(a)EDS maps of molybdenum for HEA2-A1, (b) EDS map of sulphur for HEA2 A1, (c)EDS spectrum of HEA 2 A1, showing the L_α peak and K_α peak of molybdenum and sulphur respectively*

According to Zhu et al [42], the HEA AlCoCrCuFeNiMo_x (x = 0, 0.2, 0.4, 0.6) forms two phases that are copper rich phase and molybdenum rich phase. Since the HEA 2 composition is comprising of similar elements, the phases are predicted to be similar. The formation of two different phases is due to mixing enthalpies between the elements. For example, the copper has mixing enthalpies of -1, 6, 12, 13, 4 and 19 kJ/mol with alumi-

num, cobalt, chromium, iron, nickel and molybdenum respectively. Due to this huge positive enthalpies, the atoms repulse from copper. Only aluminum is attracted by copper rich phase (γ1). This is shown in the Table 13, 14, and 15 that γ1 phase has more aluminum concentration. Similarly, the molybdenum rich phase (α1) inhibits the segregation of copper due to large difference in the mixing enthalpy.

The presence of impurities such as manganese and titanium could influence the phase formations in both the HEAs. The molybdenum rich phase (α1) which is seen inside the matrix, also has chromium. The presence of manganese forms a chromium rich phase. A study by Wang et al [60] says that presence of manganese could form chromium rich phase as strips. This chromium rich phase increases the melting point and hardness of the material. The addition of titanium forms two eutectic phases, one of which has aluminum, titanium, cobalt and nickel. The other phase is rich with chromium and iron. Considering the mixing enthalpies of manganese and titanium[88] with the other elements of HEA 1 and HEA 2, the formation of phases can be explained.

The HEA1 EDS analysis shows the presence of chromium rich phase (α or α̇) with iron and silicon. This might be due to increase in aluminum content or the combined effect of titanium and manganese inclusions. Similarly, the HEA2 also has a different phase formed which is comprised of chromium, iron and silicon. This phase is also rich with molybdenum and is particularly formed in the matrix (white spots as shown in Figure 48a). This phase is in the form of small globular or blocky shaped zones. The elemental mapping of these blocky shaped zones are also shown in Table 16.

The summary of the proposal says that, the formation of different phases is because of enthalpy effect on the individual elements. The minor contribution of impurities and increase in aluminum content has totally changed the structure of the HEA 1 alloy. The presence of the molybdenum in HEA2 had primarily allowed formation of α1- phase which is comprised of chromium, silicon and iron. The impurities had less effect on this phase formation. However, the HEA2-A2 sample showed the formation of blocky shaped strips inside the matrix which may be due to the influence of impurities.

The increase in the aluminum in the HEA1 sample also showed the formation of chromium-rich phase (α or α̇). This formation of chromium rich phase simply inhibits the copper rich phase formation. A further XRD analysis may give idea about the structures for which the presence of phases could be known.

4.3 XRD analysis

The X-ray diffraction (XRD) analysis gives an idea about the crystal structure of phases. The Figures 50, 51 and 52 are the XRD patterns of HEA-reference, HEA 1 and HEA 2 respectively. The peaks have over lapped with the standard patterns using Highscore Plus software.

The Figure 50 shows XRD pattern of HEA-reference alloy. The XRD pattern shows that all the high intensity peaks are assigned towards FCC structure. The EDS analysis of the same alloy as shown in Figure 50 shows the presence of overlapping IR and DR. Detailed examination of the peaks shows that there are two separate contributions to the peaks, thus the resultant peaks are as shown in the pattern. The similar material is studied by Jones et al[87], which had shown the same patterns. This proves the presence of both IR and DR phases, which has FCC structure.

The XRD pattern of HEA1 which was casted with same composition of HEA-reference alloy, has different peaks. The peaks are complicated and the pattern is comprised of many peaks as shown in Figure 51. The EDS analysis as described above have shown that the annealing treatment had varied the elemental distribution and thus phases. The same behavior is shown from the XRD patterns. The IR region which is a copper rich phase is annihilated during heat treatment (HEA 1 A2). This is shown clearly in the Figure 51. The XRD pattern of HEA1-vacuum and HEA 1 A1 had copper rich phase (IR). HEA1 A2 doesn't have similar peaks. This shows that the copper phase is not stable at higher annealing temperature for this alloy composition.

The new phase α (chromium, iron and silicon rich) is seen in the pattern unlike HEA-reference alloy. This new phase is the reason for many peaks in the XRD pattern. The α phase became more stable, since the peak intensity is increased with annealing treatment.

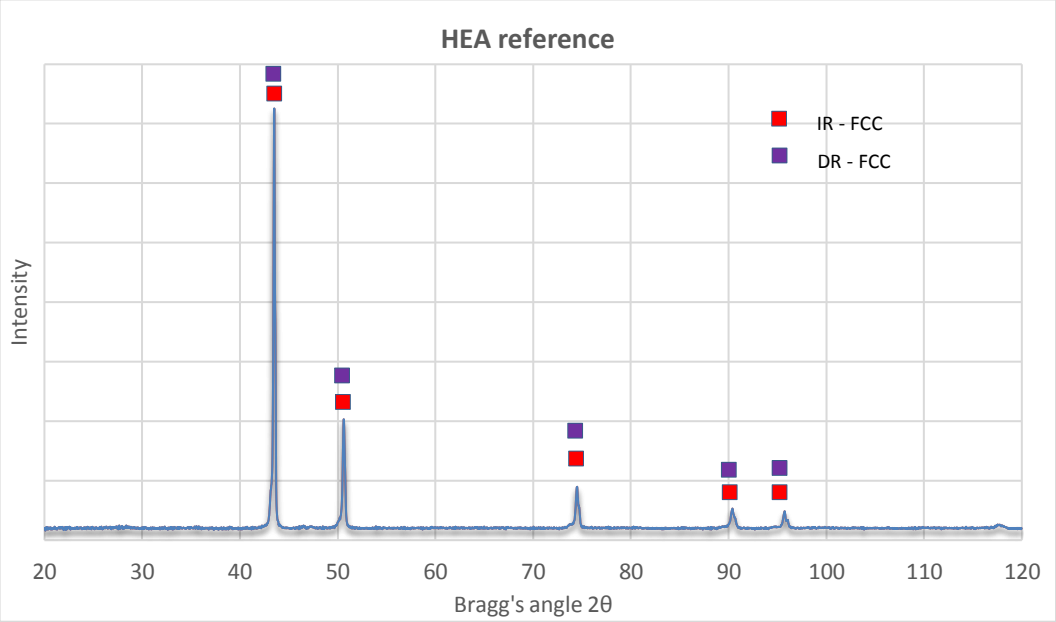

Figure 50. *XRD patterns of HEA reference.*

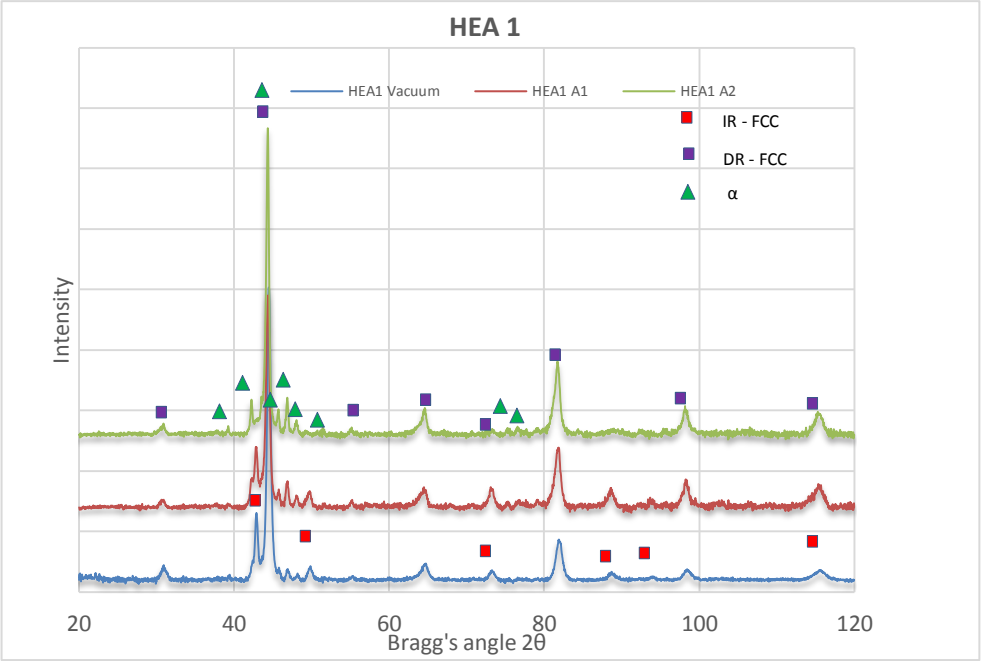

Figure 51. *XRD patterns of HEA1.*

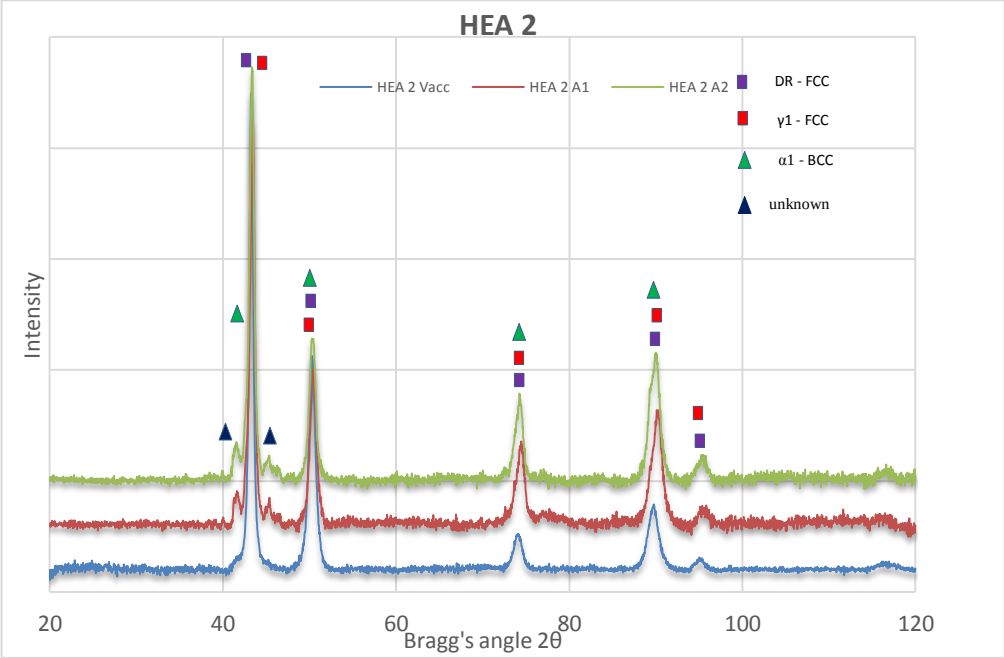

Figure 52. *XRD patterns of HEA2.*

The XRD pattern of HEA 2 as shown in Figure 52 is comprised of DR, γ1 and α1 phases. These peaks show similarity with the XRD patterns shown in a study by Zhu et al [42]. This study on AlCrCoCuFeNiMo$_x$ alloy shows the formation of peaks with FCC and BCC phases at the same positions (as shown in the Figure 24).

The EDS analysis of HEA 2 shows the presence of molybdenum rich (α1) phase. The same peaks are found when analyzed using Highscore Plus software. The α1 phase is expected to be BCC considering the analysis of the study by Zhu et al [42] . Additionally,

we can see the peaks of an unknown phase in the patterns of HEA2 A1 and HEA2 A2. These peaks are not identified using the analysis software, which is why they are named as unknown peaks. However, it is seen in the EDS analysis and SEM micrographs (Figure 47 and 48), that the matrix phase is filled with a chromium rich phase strips. It can be inferred that the presence of white strips in matrix is the reason for these new peaks.

The peaks of the α-phase in HEA 1, match mostly with a pattern of chromium-cobalt-silicon phase, which is a sigma phase formed in nickel based super alloy. The EDS map shows that α-phase is rich in chromium-iron-silicon and a small percent of cobalt. The sigma phase, which is most matched with these XRD peaks of HEA1 is tetragonal crystal structure of P42/mnm space group. Additionally, a study on criterion for sigma phase formation in chromium containing alloy by Tsai et al [89], says that sigma phase can be formed if the VEC value is between 6.88 and 7.84, but the composition of α phase is comprised of silicon which is not mentioned in this criterion. Thus the α phase structure cannot be concluded from the pattern match and EDS analysis. Most importantly the θ-phase (sulphur rich) was not visible in any of the patterns, which indicates that the θ-phase is amorphous with no proper crystal structure.

A study by Zhuang et al [90] shows that, influence of silicon had almost no impact on inhibition of copper phase in AlCuCoNiFeSi alloy. Which implies that silicon is least influenced in annihilation of copper rich phase in HEA1. However, the small percentage of silicon which is present in HEA2 does not mix with copper phase, instead is mostly mixed with the molybdenum phase.

A study by Wang et al[60] say that presence of titanium and manganese leads to the formation of chromium rich phase . A study by Jones et al [87] on $Al_{0.5}CoCrCuFeNi$ has shown the formation of sigma precipitates which are rich in chromium, iron and nickel. The chromium rich phase which is a complex structure is confirmed by XRD and EDS analysis in HEA1 A1 and HEA1 A2 samples.

A study by Dong et al [91] has shown the presence of sigma phase in $AlCrFeNiMo_{0.2}$ HEA which is rich in chromium, iron and molybdenum. The XRD and EDS analysis confirms a similar phase match to the blocky shapes inside the matrix of HEA2A2. However, the crystal structure was not studied.

Thus we can conclude that, the HEA1 α-phase may have been formed due to increase in aluminum content, but this phase was not influenced by these trace elements (titanium and manganese). The HEA2- chromium rich phase blockys inside the matrix may be due to mixing enthalpy effect. The crystal structures can't be confirmed because of the silicon inclusions in the respective phases. TEM analysis is required to know the crystal structure of the same phases. Additionally, a thermo-dynamical analysis of these alloy should be done, considering the influence of impurities like sulphur, titanium and manganese and also by considering the influence of increase in aluminum percent.

4.4 Hardness testing

Vickers hardness was measured for each specimen as mentioned in Table 5. Seven measurements are made from each sample and the average of these seven results is considered as final hardness. The measurement was done using pyramid indenter. The measurement location was chosen to cover all the phases. The results of these measurements are shown in the Figure 53.

The hardness of the HEAs tested are dependent on the compositions, inclusions and heat treatments. The hardness of HEA-reference is 195HV. A nearly same result is seen in a study of same material by Tong et al [18]. However, the HEA1 which is induction casted has very high hardness. The HEA1-vacuum, HEA1 A1 and HEA1 A2 shows an increasing trend in hardness. This is because of the presence of chromium rich phases as explain in Chapters 4.2.2 and 4.3. The quenching has increased the hardness to a large value (690HV).

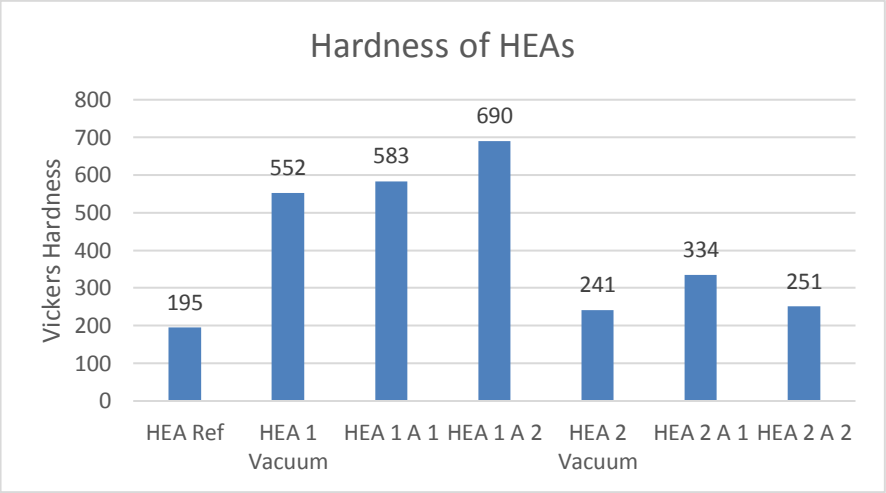

Figure 53. *Vickers hardness (in HV 3) of HEAs.*

The Hardness of HEA 2 is greater than HEA1-reference material cause of molybdenum concentration. A study by Zhu et al [42] shows that increase in the percentage of molybdenum of $AlCoCrCuFeNiMo_x$ (x = 0.2-1.0) increased the hardness. Similarly, the addition of molybdenum had increased the hardness over reference material composition. This is because of formation of BCC molybdenum rich phase. Unexpectedly, the hardness is HEA2-A2 decreased even though the sample is quenched after annealing. However, the HEA2-A2 was suddenly quenched after malfunctioning of furnace, which may have led to this decrease in hardness. A thorough investigation on phases may be required to know about reason for the decrease in hardness values.

4.5 High strain rate testing

The HSB (Hopkinson split bar) tests were conducted at different strain rates for each sample. The list of high strain rate testing is shown in the Table 17. Considering the HSB tests, the testing procedure is very sensitive and a minor deviation in the dimensions can lead to a false result. The surfaces of the samples are supposed to be smooth and parallel.

The Figure 54, 55, 56, 57 and 58 shows the true stress vs strain curves of HEA-ref, HEA1-air casted, HEA1-vacuum casted, HEA2-air casted and HEA2-vacuum casted samples respectively. The closer view of Figure 54 shows a different yield behavior. The elastic region is not clearly visible. This could mean that the sample is so ductile or the cross sectional surface is not uniform. In reality the cross sectional surfaces of the cylindrical samples are not uniform, but the deviation is so small that it should not be visible in the results.

Table 17. *HSB tests for different samples.*

Sample Code	Strain rate (1/s)
HEA ref - 1	1500
HEA ref - 2	3500
HEA1 Air -1	1200
HEA1 Vacuum-1	550
HEA2 Vacuum-1	900
HEA2 Air-1	600
HEA2 Air-2	2500
HEA2 Air -3	3200
HEA2 Vacuum-1	600
HEA2 Vacuum-2	2500
HEA2 Vacuum-3	3300

The sample dimensions of the HEA-reference are 3mm diameter/3mm thickness. We know that HEA1 reference sample is comprised of FCC structures, the deformation after the strain rates 1500/s and 3500/s is plastic. The samples are compressed to very small thickness. Similarly, the Figures 55 shows the true stress vs true strain curve of HEA 1 air casted sample. Only one sample is tested because, the sample was brittle and had fractured at 1200/s strain rate. This says that it couldn't accept the load. Thus the curve is linear till fracture point and then is dropped to zero.

The Figures 55 and 56 shows the brittle behavior of the HEA1 after the high strain rate testing. The HEA1 vacuum cast sample had fracture at 900/s strain rate. Thus it was not tested further at higher strain rates. However, it had accepted a strain rate of 550/s without any plastic deformation.

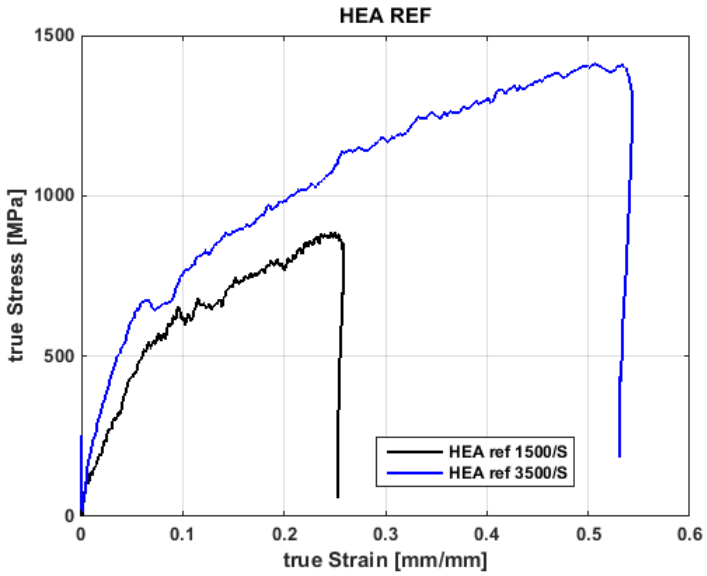

Figure 54. *True stress vs. true strain curve if HEA reference samples.*

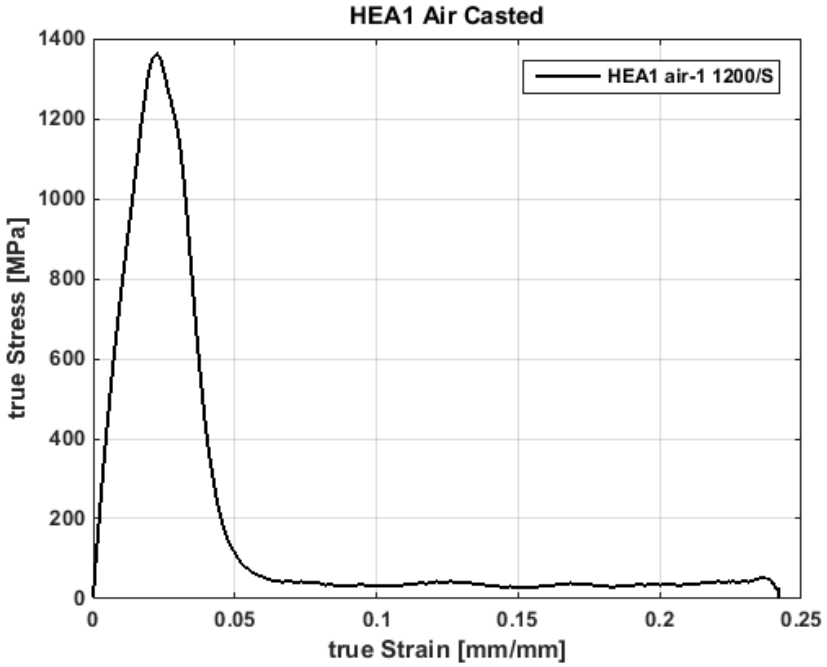

Figure 55. *True stress vs. true strain curve if HEA1 air casted samples.*

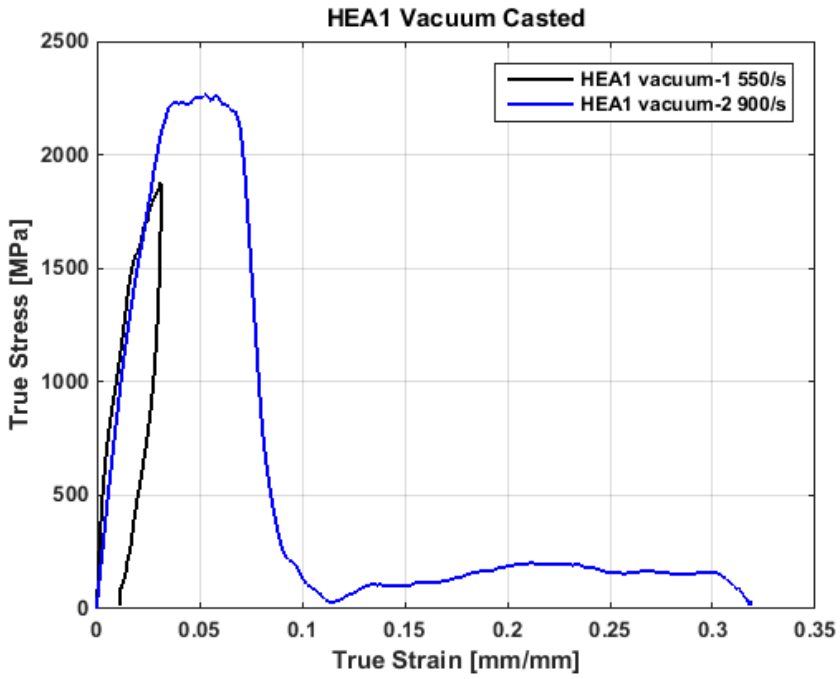

Figure 56. *True stress vs. true strain curve of HEA1 vacuum casted samples.*

The microstructural analysis and XRD has shown the formation of hard phases and amorphous phases which cannot be plastically deformed. Thus it is worthwhile to say that the HEA1 turned out to be brittle material. The sample dimensions used for both these materials is 8mm diameter / 8mm thickness.

Similarly, the Figures 57 and 58 shows the true stress vs true strain behavior of HEA 2 alloy at different casting stages. The sample dimensions used for these test at strain rates 600 and 2500/s are 8mm/8mm solid cylindrical samples. The dimensions at 3300 or 3200/s are reduced to 6mm/6mm. The true stress and true strain behavior looks like a ductile material for both air and vacuum casted samples. From microstructural analysis it is also found that the HEA 2 is comprised of FCC phase. This FCC phase can lead to plastic deformation. But the same material also is comprised of a little amount of amorphous phase and in addition to the hard molybdenum rich phase (BCC). These phases in combine could probably show a different deformation behavior.

Figure 57 and 58 shows that the yield strength of HEA 2 is increased when compared to HEA-reference material. This is because of the addition of molybdenum, and thus formation of BCC phase. A study by Zhu et al[42] on $AlCrCoCuFeNiMo_x$ says that the increase in molybdenum concentration increases the hardness values.

The Figure 59 shows all the true stress vs true strain curves of HEA 2 air casted and vacuum casted samples. At higher strain rates 2500 and 3300/s, the HEA 2 air casted sample shows a similar yield stress level compared to HEA 2 vacuum casted sample. This shows that the phases present in HEA2 air and vacuum casts are similar.

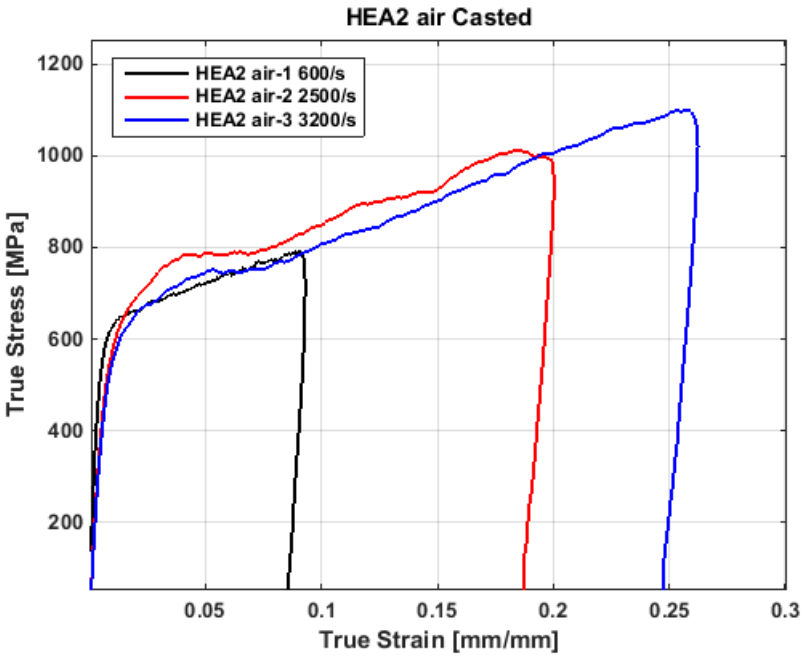

Figure 57. *True stress vs. true strain curve of HEA2 air casted samples.*

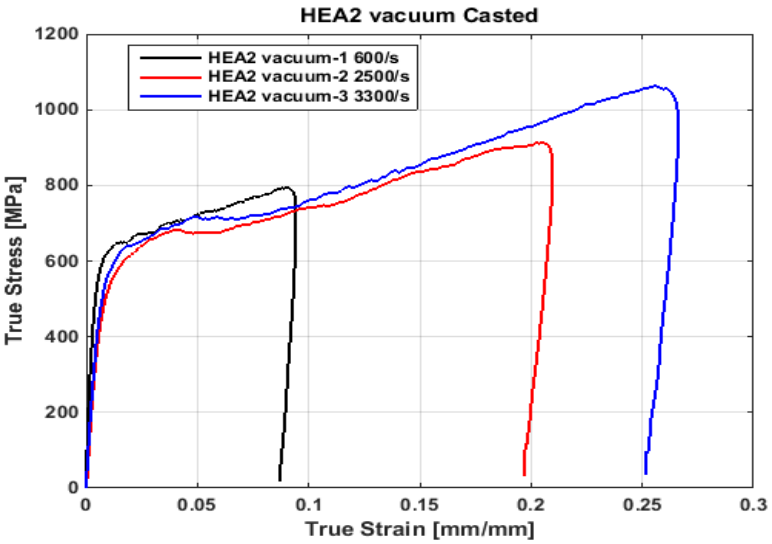

Figure 58. *True stress vs. true strain curve of HEA2 vacuum casted samples.*

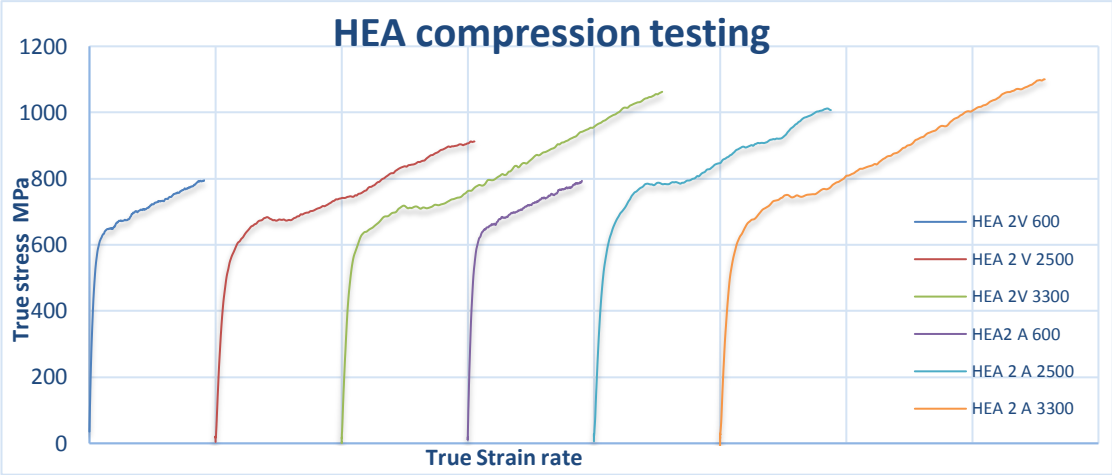

Figure 59. *True stress vs. true strain curve of all HEA2 samples.*

Table 18. *Yield strength, maximum compression load and maximum plastic strain*

Sample code (strain rates)	Yield strength MPa	Maximum compression load	Maximum strain %
HEA2 V 600	563	795	9.4
HEA 2 V 2500	526	913	21.0
HEA 2V 3300	NA	1063	26.5
HEA 2A 600	541	793	9.3
HEA 2 A 2500	506	1012	20.0
HEA 2A 3200	510	1100	26.2
HEA ref 1500	NA	888	25.9
HEA ref 3500	NA	1412	54.4
HEA 1 A 1200	NA	1361	2.3
HEA1 V 550	NA	1875	3.0
HEA1 V 900	NA	2263	5.2

Interestingly, the HEA reference sample is deformed and the thickness is reduced without affecting the shape. Whereas, the HEA 2 samples were deformed in elliptical shapes after the compression tests. This creates a special interest to know about the behavior. The sample before and after compression testing as shown the Figure. 60. The optical micrographs and SEM micrographs are shown in Figure 61 and 62 respectively.

The test samples are showing a peculiar behavior in deformation. That is the FCC or copper phase is deformed plastically and the BCC phase or molybdenum rich phase is broken into finer parts. This kind of deformation mechanism is very interesting, where only a small percentage (1%) of change in BCC stabilizers like aluminum and molybdenum can change the phase stabilities and thus the deformation mechanisms. The increase in copper content (FCC stabilizer) can increase the ductility. This mechanism also explains about the increase in elongation and tensile strength values as mention in Figure 28.

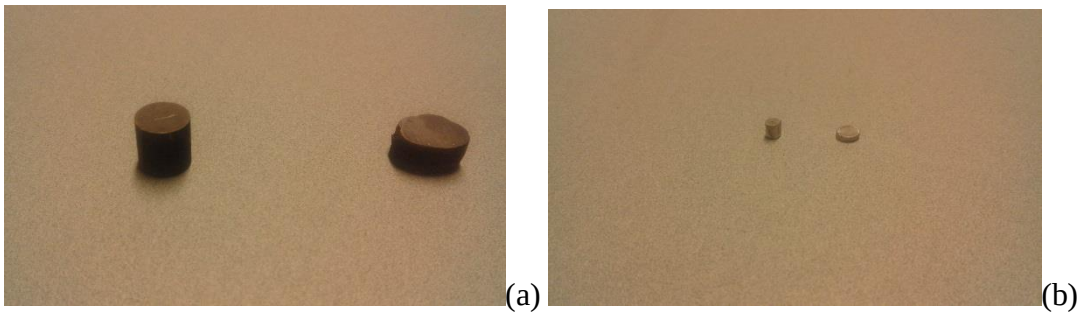

Figure 60. *(a) HEA 2 Air casted sample before and after 3300, (b)HEA Ref sample before and after 1200/s sample*

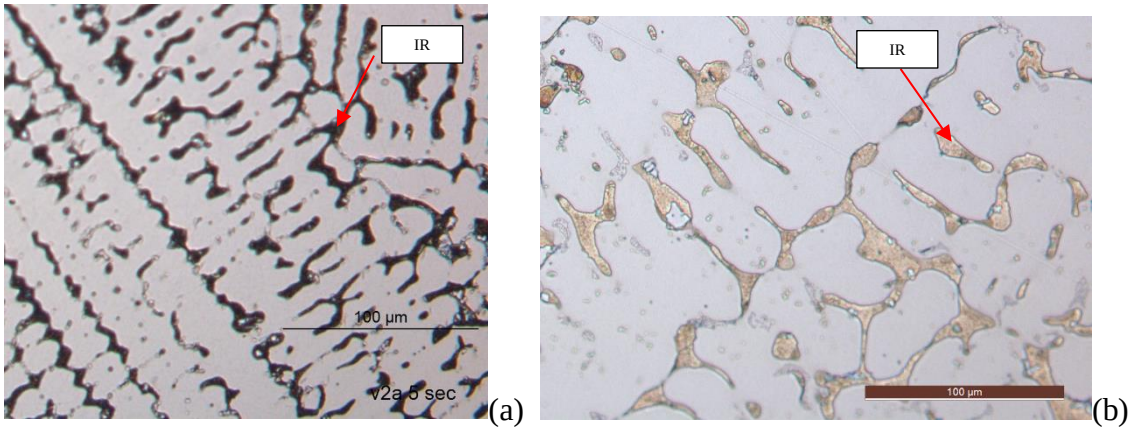

Figure 61. *HEA2 Air casting micrographs (a) before compression, (b) after strain rate of 800/s (IR – inter dendritic region);*

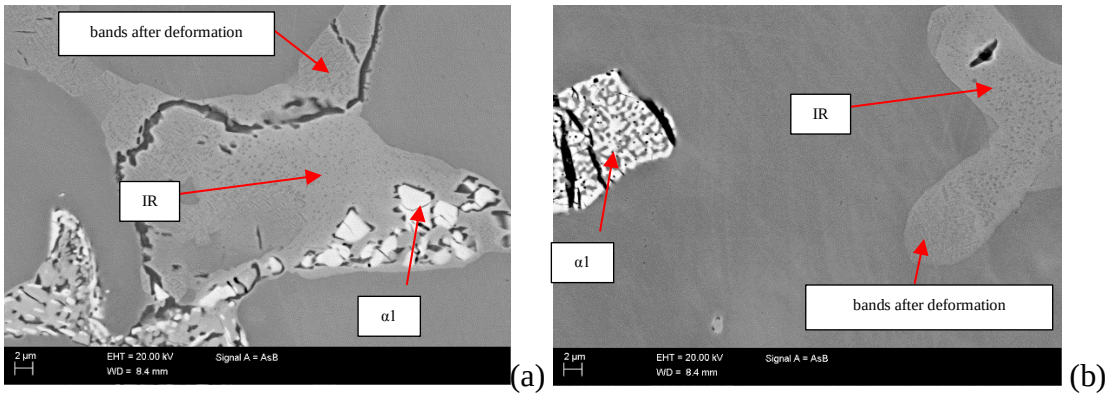

Figure 62. *Back scattered SEM micrographs of (a) HEA 2 Air casting after 800/s and (b) HEA 2 vacuum casting after 3300/s*

The Figure 61 shows the difference between the optical micrographs in the IR. The copper phase is deformed. The molybdenum phase is clearly visible in optical micrographs. The Figure 62 shows the back scattered images of HEA 2 air casted and HEA 2 vacuum casted samples, which are tested at 800/s and 3300/s strain rates. The α1- phase is broken, as the cracks are visible. Whereas, the IR has some visible bands. These bands may be classified

as adiabatic, twinning or any bands formed due to plastic deformation. A TEM analysis may be required to define the bands present, since these bands are in nanometer scale which can't be easily classified through FESEM.

It is known that the high strain rate deformation is highly influenced by phonon drag effect phenomenon. The yield strength values from the evaluated results are found inconclusive due to unexpected decrease. This may be due to presence of both the phases, where the deformation mechanism seemed complex.

A study by Kumar et al [6] on $Al_{0.1}$CrFeCoNi HEA shows twinning induced plastic deformation after similar high strain rate testing. This is because the $Al_{0.1}$CrFeCoNi HEA is of FCC crystal structure. Additionally, the stacking fault energy is lower in this high entropy alloy. The FCC and low stacking fault energy make the alloy a perfect combination for twinning induced plastic deformation. However, the HEA2 which is tested now has both BCC and FCC. Thus from previous studies it is assumed that the twins may be formed provided the availability of similar phases.

Additionally, it could also be assumed that there is a possibility of adiabatic shear bands formed in BCC and FCC region due to internal heat generated during high strain rates.

4.6 Corrosion testing

The HEA2 sample is tested to know the corrosion properties in the 5% HNO3 atmosphere. The potentio-dynamic corrosion data scanners collected the parameters such as E_{corr} (corrosion potential) and I_{corr} (corrosion current density), using the Tafel slope extrapolation. The results of the extrapolation are given in the Table 19

The polarization curves of a metal or alloy indicate the corrosion behavior of material inside a test media. The presence of the passivation can be determined easily from the polarization curves, whether it is self-passive or anodic dissolution is required to induce passivation.

Table 19. *Electrochemical parameters evaluated using Tafel slope extrapolation.*

Alloy - Code	E_{corr} (mV)	I_{corr} (mA/cm2)
HEA reference	13.9	0.119
HEA2 Air	86.9	0.566
HEA2 Vacuum	64.7	0.0781
HEA 2 A 1	71.4	0.365
HEA 2 A 2	30.4	0.107
TWIP	-248	1.42

The Figure 63 shows the polarization of curves of different materials tested. The TWIP steel is used as a reference material for the comparison about corrosion properties. It is clear that all the HEAs are showing good passivation regime (P marked inside the Figure

63) and TWIP steel had doesn't have any passive regime. TWIP steel can hardly be passive, because the anodic dissolution happened to maintain the passivity.

The scanning range of all HEA2 alloys started between -430mV to -450mV and is extended to +1000mV. Whereas, the scanning potential for TWIP steel started from -710mV and ended at +749mV. The initial passivation potential of all HEAs started around +200mV. The HEA2 A2 sample gives most stable passivation out of all the alloys. The TWIP steel is passivated only after the anodic dissolution occurred. That is the solution is neutralized by the dissolution of TWIP steel. The passivation layer formation can be seen in HEA2 alloy as shown in Figure 64a and the Figure 64b shows the anodic dissolution of TWIP steel after corrosion test.

Thus it is proved that the corrosion resistivity of HEAs is greater than TWIP steel, in the 5% aqueous nitric acid media. Thus, it could be concluded that, the current test specimens of HEAs shows a better corrosion resistance by passive layer formation. However the results of Hamada[86] on testing of the same alloy in the same 5% nitric acid media have given good passivation. This difference might because of differences in testing condition.

The study by Qiu et al [81] shows that HEAs have far better corrosion resistance properties than the conventional alloys or any special grade alloys. This is because the HEAs which are comprised of aluminum and chromium form oxide layers (passivation) in any acidic or corrosive environments.

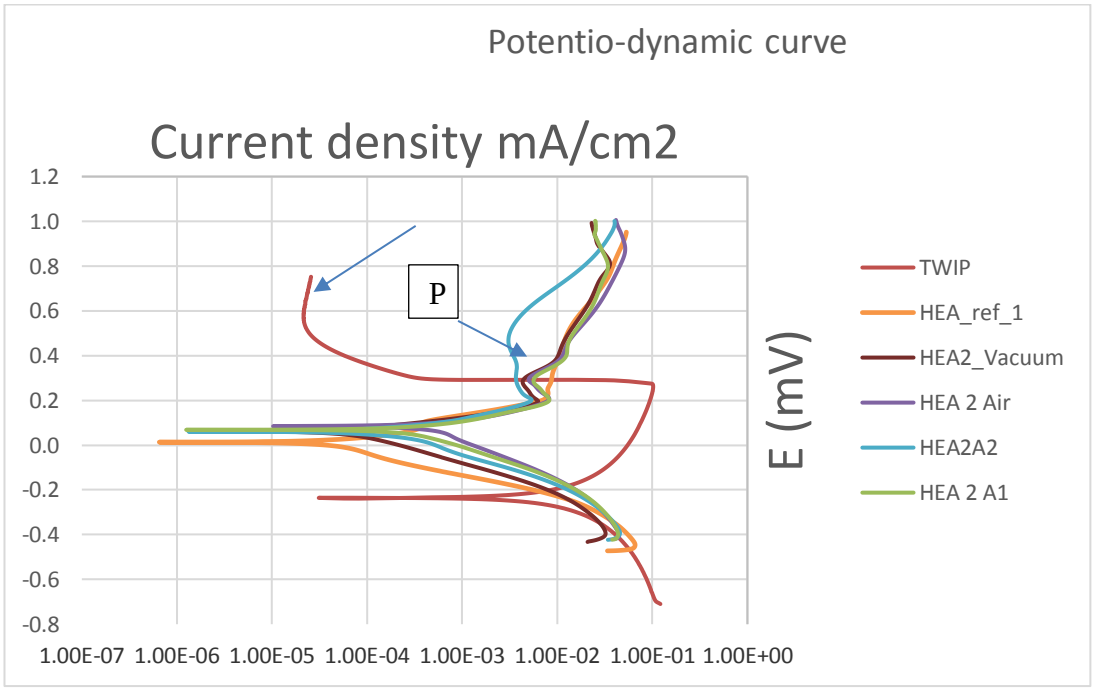

Figure 63. *Potentio-dynamic curve of all tested alloys*

(a)


(b)

Figure 64. *Sample after corrosion testing (a) HEA2 A2 – passive layer formation (b) TWIP steel dissolution*

5. CONCLUSION

Annealing treatments (homogenization for 72 hours) are done to the HEAs and further extensive characterization was done using optical microscope, SEM, EDS and X-ray diffraction techniques. The hardness measurements were made after every treatment. The mechanical behavior at high strain rates were tested using HSB testing machine, ranging from 600/s to 3600/s. Finally, corrosion tests were conducted to the HEA2, HEA-reference and a TWIP steel sample.

The results of annealing were mostly unexpected. The phase stability has taken a shift from the phases present in the as-cast HEA1 to new phases after annealing of HEA1. This may be due to the increase in aluminum content by miscalculation during cast. The impurities like sulphur, silicon, titanium, manganese and zirconium also may have affected the phase changes. The influence of impurities had not effected the phases in HEA2, but might have influenced the mechanical properties. However, based on the data available through the characterization techniques, it is hard to conclude the influence of each impurity element.

The microstructural characterization reveals the presence of chromium rich hard phase in HEA1 and traces in the matrix of HEA2. The chromium rich phase in HEA2 also contains molybdenum which has composition similar to molybdenum rich phase. These hard phases are most stabilized after annealing. This chromium phase matches in XRD patterns with sigma phases found in nickel based super alloys.

The hardness tests show the increase in hardness after the heat treatments. The HEA2 sample had less hardness after quenching than the same sample after cooling inside the furnace. The reason for the decrease in hardness is yet to be known.

The high strain rate tests for HEA1 only prove that the material is brittle. The HEA reference was plastically deformed due to the presence of FCC phases. It is found that HEA2 has deformed in a different mechanism, that is only FCC structure copper rich phase has deformed with bands formation. Specifically, cracks are found in BCC structure (molybdenum rich). This type of deformation is identified after inspection through optical microscopy and SEM. However, the deformation mechanism can’t be concluded until there is further investigation using TEM.

The corrosion test in 5% concentrated nitric acid electrolyte reveals the noble corrosion resistant properties of these HEAs. The TWIP steel underwent dissolution into electrolyte and faced a considerable amount of volume loss. All the HEA tested samples formed a passive layer over surface which stopped further dissolution of the alloy.

Finally, it is very clear that thermodynamic factors enthalpy and entropy play important role in the phase formation. The annealing treatments only have shown the stability of equilibrium phases by providing the excitation energy, after exposing to the high temperature. However, the enthalpy factor is dominating entropy factor by forming multiple phases.

6. FURTHER EXPERIMETAL PLANS AND RESEARCH QUESTIONS

The HEAs have given a clear definition of thermodynamics and their role. The best example is the current thesis, which says how a minor change in composition could greatly impact the phase formations. The results of the current thesis have given ideas to lot of topics for the further research.

Since the HEA 2 (with molybdenum derivative) is showing good ductile properties, and phase stability of FCC and BCC, it can be further tested to know the properties after thermo-mechanical treatments.

- TEM analysis should be done to know more about the phases formed in the HEAs especially about molybdenum rich phase.
  - To know more about bands formed in copper rich phase after compression tests.
  - Stacking fault energy could be calculated for the as-cast and annealed HEAs, if twins are found after dynamic and quasi static tests.
- Thermodynamic modelling of SFE of HEAs can be done if it is found that these HEAs are having low stacking fault energy.
- The wear resistant and fatigue properties could be tested using the HEA2 alloy.
- Thermal analysis of the HEA2 alloy to be performed at different cooling rates.
  - These tests classify the phase stability at different temperature.
  - The high temperature XRD can be done to define the structures of different phases formed.
- Dilatometer experiments can be conducted to define the co-efficient of thermal expansion.
- Using the results from thermal analysis and high temperature XRD, a material modelling can be made with the HEA2 composition.
  - This model could predict the phase stability at different temperatures.
  - A model could also be made which shows the influence of impurities on the phase formations.

The formation of new hard chromium rich phase in HEA1 has raised some important questions about the current alloy. The questions are about the presence of various impurities and the casting practices.

- Proper casting practices can improve the quality of the cast.

7. REFERENCES

[1] B. S. Murty, J. W. Yeh, and S. Ranganathan, *High Entropy Alloys*. Elsevier, 2014.

[2] Y. F. Ye, Q. Wang, J. Lu, C. T. Liu, and Y. Yang, "High-entropy alloy : challenges and prospects," vol. 00, no. 00, 2015.

[3] J. W. Yeh, S. K. Chen, S. J. Lin, J. Y. Gan, T. S. Chin, T. T. Shun, C. H. Tsau, and S. Y. Chang, "Nanostructured high-entropy alloys with multiple principal elements: Novel alloy design concepts and outcomes," *Adv. Eng. Mater.*, vol. 6, no. 5, pp. 299–303+274, 2004.

[4] Mukhopadhyay N.K, "High entropy alloys: a renaissance in physical metallurgy," *Curr. Opin. Solid State Mater. Sci.*, vol. 109, no. 4, pp. 665–667, 2015.

[5] M.-H. Tsai, "Three Strategies for the Design of Advanced High-Entropy Alloys," *Entropy*, vol. 18, no. 7, p. 252, 2016.

[6] N. Kumar, Q. Ying, X. Nie, R. S. Mishra, Z. Tang, P. K. Liaw, R. E. Brennan, K. J. Doherty, and K. C. Cho, "High strain-rate compressive deformation behavior of the Al0.1CrFeCoNi high entropy alloy," *Mater. Des.*, vol. 86, pp. 598–602, 2015.

[7] J. M. Zhu, H. M. Fu, H. F. Zhang, A. M. Wang, H. Li, and Z. Q. Hu, "Microstructures and compressive properties of multicomponent AlCoCrFeNiMox alloys," *Mater. Sci. Eng. A*, vol. 527, no. 26, pp. 6975–6979, 2010.

[8] S. Ranganathan, "Alloyed pleasures: multimetallic cocktails," *Curr. Sci.*, vol. 85, pp. 1404–1406.

[9] M.-H. Tsai and J.-W. Yeh, "High-Entropy Alloys: A Critical Review," *Mater. Res. Lett.*, vol. 2, no. 3, pp. 107–123, 2014.

[10] D. R. Gaskell, *Introduction to the thermodynamics of materials*, Fourth Edi. Washington, D.C: Taylor & Francis group, 2003.

[11] O. N. Senkov, J. D. Miller, D. B. Miracle, and C. Woodward, "Accelerated exploration of multi-principal element alloys for structural applications," *Calphad Comput. Coupling Phase Diagrams Thermochem.*, vol. 50, pp. 32–48, 2015.

[12] B. Cantor, "Multicomponent and high entropy alloys," *Entropy*, vol. 16, no. 9, pp. 4749–4768, 2014.

[13] D. B. Miracle, J. D. Miller, O. N. Senkov, C. Woodward, M. D. Uchic, and J. Tiley, "Exploration and development of high entropy alloys for structural applications," *Entropy*, vol. 16, no. 1, pp. 494–525, 2014.

[14] G. P. Tiwari, "Modification of Richard's rule and correlation between entropy of fusion and allotropic behaviour," *Met. Sci.*, vol. 12, no. 7, pp. 317–320, Jul. 1978.

[15] Y. Zhang, T. T. Zuo, Z. Tang, M. C. Gao, K. A. Dahmen, P. K. Liaw, and Z. P. Lu, "Microstructures and properties of high-entropy alloys," *Prog. Mater. Sci.*, vol. 61, no. October 2013, pp. 1–93, 2014.

[16] J. W. Yeh, "Physical Metallurgy of High-Entropy Alloys," *Jom*, vol. 67, no. 10, pp. 2254–2261, 2015.

[17] M.-R. Chen, S.-J. Lin, J.-W. Yeh, S.-K. Chen, Y.-S. Huang, and C.-P. Tu, "Microstructure and Properties of Al0.5CoCrCuFeNiTix (x=0–2.0) High-Entropy Alloys," *Mater. Trans.*, vol. 47, no. 5, pp. 1395–1401, 2006.

[18] C.-J. Tong, Y.-L. Chen, J.-W. Yeh, S.-J. Lin, S.-K. Chen, T.-T. Shun, C.-H. Tsau, and S.-Y. Chang, "Microstructure characterization of Al x CoCrCuFeNi high-entropy alloy system with multiprincipal elements," *Metall. Mater. Trans. A*, vol. 36, no. 4, pp. 881–893, 2005.

[19] Y. J. Hsu, W. C. Chiang, and J. K. Wu, "Corrosion behavior of FeCoNiCrCux high-entropy alloys in 3.5% sodium chloride solution," *Mater. Chem. Phys.*, vol. 92, no. 1, pp. 112–117, 2005.

[20] E. J. Pickering and N. G. Jones, "High-entropy alloys: a critical assessment of their founding principles and future prospects," *Int. Mater. Rev.*, vol. 6608, no. May, pp. 1–20, 2016.

[21] C. W. Tsai, Y. L. Chen, M. H. Tsai, J. W. Yeh, T. T. Shun, and S. K. Chen, "Deformation and annealing behaviors of high-entropy alloy Al0.5CoCrCuFeNi," *J. Alloys Compd.*, vol. 486, no. 1–2, pp. 427–435, 2009.

[22] K. Y. Tsai, M. H. Tsai, and J. W. Yeh, "Sluggish diffusion in Co-Cr-Fe-Mn-Ni high-entropy alloys," *Acta Mater.*, vol. 61, no. 13, pp. 4887–4897, 2013.

[23] J.-W. Yeh, S.-Y. Chang, Y.-D. Hong, S.-K. Chen, and S.-J. Lin, "Anomalous decrease in X-ray diffraction intensities of Cu–Ni–Al–Co–Cr–Fe–Si alloy systems with multi-principal elements," *Mater. Chem. Phys.*, vol. 103, no. 1, pp. 41–46, May 2007.

[24] G. A. Mansoori, N. F. Carnahan, K. E. Starling, and T. W. Leland Jr., "Equilibrium Thermodynamic Properties of the Mixture of Hard Spheres," *J. Chem. Phys.*, vol. 54, no. 4, p. 1523, 1971.

[25] Y. F. Ye, Q. Wang, J. Lu, C. T. Liu, and Y. Yang, "Design of high entropy alloys: A single-parameter thermodynamic rule," *Scr. Mater.*, vol. 104, pp. 53–55, Jul. 2015.

[26] Y. Zhang, Y. J. Zhou, J. P. Lin, G. L. Chen, and P. K. Liaw, "Solid-solution phase formation rules for multi-component alloys," *Adv. Eng. Mater.*, vol. 10, no. 6, pp. 534–538, 2008.

[27] X. Yang and Y. Zhang, "Prediction of high-entropy stabilized solid-solution in multi-component alloys," *Mater. Chem. Phys.*, vol. 132, no. 2–3, pp. 233–238, 2012.

[28] O. N. Senkov and D. B. Miracle, “A new thermodynamic parameter to predict formation of solid solution or intermetallic phases in high entropy alloys,” *J. Alloys Compd.*, vol. 658, pp. 603–607, 2016.

[29] S. Guo, C. Ng, J. Lu, and C. T. Liu, “Effect of valence electron concentration on stability of fcc or bcc phase in high entropy alloys,” *J. Appl. Phys.*, vol. 109, no. 10, 2011.

[30] Y. F. Ye, Q. Wang, J. Lu, C. T. Liu, and Y. Yang, “High-entropy alloy: challenges and prospects,” *Mater. Today*, vol. 19, no. 6, pp. 349–362, Jul. 2016.

[31] M.-H. Tsai, K.-C. Chang, J.-H. Li, R.-C. Tsai, and A.-H. Cheng, “A second criterion for sigma phase formation in high-entropy alloys,” *Mater. Res. Lett.*, vol. 3831, no. April, pp. 1–6, 2015.

[32] S. Wang, “Atomic structure modeling of multi-principal-element alloys by the principle of maximum entropy,” *Entropy*, vol. 15, no. 12, pp. 5536–5548, 2013.

[33] D. Ma, B. Grabowski, F. Körmann, J. Neugebauer, and D. Raabe, “Ab initio thermodynamics of the CoCrFeMnNi high entropy alloy: Importance of entropy contributions beyond the configurational one,” *Acta Mater.*, vol. 100, pp. 90–97, 2015.

[34] F. Tian, L. K. Varga, J. Shen, and L. Vitos, “Calculating elastic constants in high-entropy alloys using the coherent potential approximation: Current issues and errors,” *Comput. Mater. Sci.*, vol. 111, pp. 350–358, 2016.

[35] S. Singh, N. Wanderka, B. S. Murty, U. Glatzel, and J. Banhart, “Decomposition in multi-component AlCoCrCuFeNi high-entropy alloy,” *Acta Mater.*, vol. 59, no. 1, pp. 182–190, 2011.

[36] Y. Zhang, S. G. Ma, and J. W. Qiao, “Morphology transition from dendrites to equiaxed grains for AlCoCrFeNi high-entropy alloys by copper mold casting and bridgman solidification,” in *Metallurgical and Materials Transactions A: Physical Metallurgy and Materials Science*, 2012, vol. 43, no. 8, pp. 2625–2630.

[37] L. M. Wang, C. C. Chen, J. W. Yeh, and S. T. Ke, “The microstructure and strengthening mechanism of thermal spray coating NixCo0.6Fe0.2CrySizAlTi0.2 high-entropy alloys,” *Mater. Chem. Phys.*, vol. 126, no. 3, pp. 880–885, 2011.

[38] S. Varalakshmi, M. Kamaraj, and B. S. Murty, “Formation and stability of equiatomic and nonequiatomic nanocrystalline CuNiCoZnAlTi high-entropy alloys by mechanical alloying,” *Metall. Mater. Trans. A Phys. Metall. Mater. Sci.*, vol. 41, no. 10, pp. 2703–2709, 2010.

[39] S. Y. Chang, S. Y. Lin, Y. C. Huang, and C. L. Wu, “Mechanical properties, deformation behaviors and interface adhesion of (AlCrTaTiZr)Nx multi-component coatings,” *Surf. Coatings Technol.*, vol. 204, no. 20, pp. 3307–3314, 2010.

[40] C. W. Tsai, M. H. Tsai, J. W. Yeh, and C. C. Yang, “Effect of temperature on mechanical properties of Al0.5CoCrCuFeNi wrought alloy,” *J. Alloys Compd.*,

vol. 490, no. 1–2, pp. 160–165, 2010.

[41] C.-J. Tong, M.-R. Chen, J.-W. Yeh, S.-J. Lin, S.-K. Chen, T.-T. Shun, and S.-Y. Chang, "Mechanical performance of the Al x CoCrCuFeNi high-entropy alloy system with multiprincipal elements," *Metall. Mater. Trans. A*, vol. 36, no. 5, pp. 1263–1271, 2005.

[42] J. M. Zhu, H. F. Zhang, H. M. Fu, A. M. Wang, H. Li, and Z. Q. Hu, "Microstructures and compressive properties of multicomponent AlCoCrCuFeNiMox alloys," *J. Alloys Compd.*, vol. 497, no. 1–2, pp. 52–56, 2010.

[43] S. Praveen, B. S. Murty, and R. S. Kottada, "Alloying behavior in multi-component AlCoCrCuFe and NiCoCrCuFe high entropy alloys," *Mater. Sci. Eng. A*, vol. 534, pp. 83–89, 2012.

[44] T. M. Butler and M. L. Weaver, "Oxidation behavior of arc melted AlCoCrFeNi multi-component high-entropy alloys," *J. Alloys Compd.*, vol. 674, pp. 229–244, 2016.

[45] X. Yang, Y. Zhang, and P. K. Liaw, "Microstructure and compressive properties of NbTiVTaAlx high entropy alloys," *Procedia Eng.*, vol. 36, pp. 292–298, 2012.

[46] O. N. Senkov, J. M. Scott, S. V. Senkova, F. Meisenkothen, D. B. Miracle, and C. F. Woodward, "Microstructure and elevated temperature properties of a refractory TaNbHfZrTi alloy," *J. Mater. Sci.*, vol. 47, no. 9, pp. 4062–4074, 2012.

[47] O. N. Senkov, G. B. Wilks, J. M. Scott, and D. B. Miracle, "Mechanical properties of Nb25Mo25Ta25W25 and V20Nb20Mo20Ta20W20 refractory high entropy alloys," *Intermetallics*, vol. 19, no. 5, pp. 698–706, 2011.

[48] R. Li, J.-C. Gao, and K. Fan, "Microstructure and mechanical properties of MgMnAlZnCu high entropy alloy cooling in three conditions," *Mater. Sci. Forum*, vol. 686, pp. 235–241, 2011.

[49] C. C. Juan, J. W. Yeh, and T. S. Chin, "A novel light high-entropy alloy Al20Be20Fe10Si15Ti35," in *E- MRS Fall Meeting*, 2009.

[50] R. Li, J. Gao, and K. Fa, "Study to microstructure and mechanical properties of Mg containing high entropy alloys," *Mater. Sci. Forum*, vol. 650, pp. 265–271, 2010.

[51] H. F. Li, X. H. Xie, K. Zhao, Y. B. Wang, Y. F. Zheng, W. H. Wang, and L. Qin, "In vitro and in vivo studies on biodegradable CaMgZnSrYb high-entropy bulk metallic glass," *Acta Biomater.*, vol. 9, no. 10, pp. 8561–8573, 2013.

[52] S. Guo, Q. Hu, C. Ng, and C. T. Liu, "More than entropy in high-entropy alloys: Forming solid solutions or amorphous phase," *Intermetallics*, vol. 41, pp. 96–103, 2013.

[53] K. Zhao, X. X. Xia, H. Y. Bai, D. Q. Zhao, and W. H. Wang, "Room temperature homogeneous flow in a bulk metallic glass with low glass transition temperature," *Appl. Phys. Lett.*, vol. 98, no. 14, 2011.

[54] A. C. Yeh, T. K. Tsao, Y. J. Chang, K. C. Chang, J. W. Yeh, M. S. Chiou, S. R. Jian, C. M. Kuo, W. R. Wang, and H. Murakami, "Developing New Type of High Temperature Alloys – High Entropy Superalloys," *Int. J. Metall. Mater. Eng.*, vol. 1, no. 107, pp. 1–4, 2015.

[55] Z. Wang, Y. Huang, J. Wang, and C. T. Liu, "Design of high entropy alloys based on the experience from commercial superalloys," *Philos. Mag. Lett.*, vol. 95, no. May 2015, pp. 1–6, 2015.

[56] M.-H. Tsai, H. Yuan, G. Cheng, W. Xu, W. W. Jian, M.-H. Chuang, C.-C. Juan, A.-C. Yeh, S.-J. Lin, and Y. Zhu, "Significant hardening due to the formation of a sigma phase matrix in a high entropy alloy," *Intermetallics*, vol. 33, pp. 81–86, 2013.

[57] C. Ng, S. Guo, J. Luan, S. Shi, and C. T. Liu, "Entropy-driven phase stability and slow diffusion kinetics in an Al0.5CoCrCuFeNi high entropy alloy," *Intermetallics*, vol. 31, pp. 165–172, 2012.

[58] M.-R. Chen, S.-J. Lin, J.-W. Yeh, S.-K. Chen, Y.-S. Huang, and C.-P. Tu, "Microstructure and Properties of Al0.5CoCrCuFeNiTix (x=0–2.0) High-Entropy Alloys," *Mater. Trans.*, vol. 47, no. 5, pp. 1395–1401, 2006.

[59] M. Chuang, M. Tsai, W. Wang, S. Lin, and J. Yeh, "Microstructure and wear behavior of AlxCo1.5CrFeNi1.5Tiy high-entropy alloys," *Acta Mater.*, vol. 59, no. 16, pp. 6308–6317, 2011.

[60] B. S. Li, Y. P. Wang, M. X. Ren, C. Yang, and H. Z. Fu, "Effects of Mn, Ti and V on the microstructure and properties of AlCrFeCoNiCu high entropy alloy," *Mater. Sci. Eng. A*, vol. 498, no. 1–2, pp. 482–486, 2008.

[61] A. J. Zaddach, C. Niu, C. C. Koch, and D. L. Irving, "Mechanical properties and stacking fault energies of NiFeCrCoMn high-entropy alloy," *JOM*, 2013.

[62] J. M. Zhu, H. M. Fu, H. F. Zhang, A. M. Wang, H. Li, and Z. Q. Hu, "Microstructure and compressive properties of multiprincipal component AlCoCrFeNiCx alloys," *J. Alloys Compd.*, vol. 509, no. 8, pp. 3476–3480, 2011.

[63] J. M. Zhu, H. M. Fu, H. F. Zhang, A. M. Wang, H. Li, and Z. Q. Hu, "Synthesis and properties of multiprincipal component AlCoCrFeNiSix alloys," *Mater. Sci. Eng. A*, vol. 527, no. 27–28, pp. 7210–7214, 2010.

[64] Y. P. Wang, B. S. Li, M. X. Ren, C. Yang, and H. Z. Fu, "Microstructure and compressive properties of AlCrFeCoNi high entropy alloy," *Mater. Sci. Eng. A*, vol. 491, no. 1–2, pp. 154–158, 2008.

[65] S. G. Ma and Y. Zhang, "Effect of Nb addition on the microstructure and properties of AlCoCrFeNi high-entropy alloy," *Mater. Sci. Eng. A*, vol. 532, pp. 480–486, 2012.

[66] Y. J. Zhou, Y. Zhang, Y. L. Wang, and G. L. Chen, "Microstructure and compressive properties of multicomponent Alx(TiVCrMnFeCoNiCu)100-x high-entropy alloys," *Mater. Sci. Eng. A*, vol. 454–455, pp. 260–265, 2007.

[67] C.-J. Tong, Y.-L. Chen, J.-W. Yeh, S.-J. Lin, S.-K. Chen, T.-T. Shun, C.-H. Tsau, and S.-Y. Chang, "Mechanical Performance of the AlxCoCrCuFeNi High-Entropy Alloy System with Multiprincipal Elements," *Metall. Mater. Trans. A*, vol. 36, no. 4, pp. 881–893, 2005.

[68] S. Curtze, "Characterization of the Dynamic Behavior and Microstructure Evolution of High Strength Sheet Steels," 2009.

[69] W. D. Callister, *Materials Science and Engineering*, vol. 29. 2009.

[70] A. Soltani, "Effect of Adiabatic Heating on Strain Induced Phase Transformations in Stainless Steels Master of Science Thesis," 2013.

[71] T. M. Butler and M. L. Weaver, "Influence of Annealing on the Microstructures and Oxidation Behaviors of Al8(CoCrFeNi)92, Al15(CoCrFeNi)85, and Al30(CoCrFeNi)70 High-Entropy Alloys," *Metals (Basel).*, vol. 6, no. 9, p. 222, 2016.

[72] T. M. Butler, J. P. Alfano, R. L. Martens, and M. L. Weaver, "High-Temperature Oxidation Behavior of Al-Co-Cr-Ni-(Fe or Si) Multicomponent High-Entropy Alloys," *JOM*, vol. 67, no. 1, pp. 246–259, 2015.

[73] J. C. Jiang and Y. Luo, "High Temperature Oxidation Behaviour of AlCuTiFeNiCr High-Entropy Alloy," *Adv. Mater. Res.*, vol. 652–654, pp. 1115–1118, 2013.

[74] H. M. Daoud, A. M. Manzoni, R. Völkl, N. Wanderka, and U. Glatzel, "Oxidation Behavior of Al8Co17Cr17Cu8Fe17Ni33, Al23Co15Cr23Cu8Fe15Ni15, and Al17Co17Cr17Cu17Fe17Ni17 Compositionally Complex Alloys (High-Entropy Alloys) at Elevated Temperatures in Air," *Adv. Eng. Mater.*, vol. 17, no. 8, pp. 1134–1141, 2015.

[75] G. R. Holcomb, J. Tylczak, and C. Carney, "Oxidation of CoCrFeMnNi High Entropy Alloys," *JOM*, vol. 67, no. 10, pp. 2326–2339, 2015.

[76] B. Gorr, F. Mueller, H. J. Christ, T. Mueller, H. Chen, A. Kauffmann, and M. Heilmaier, "High temperature oxidation behavior of an equimolar refractory metal-based alloy [Formula presented] with and without Si addition," *J. Alloys Compd.*, vol. 688, pp. 468–477, 2016.

[77] B. Gorr, M. Azim, H.-J. Christ, T. Mueller, D. Schliephake, and M. Heilmaier, "Phase equilibria, microstructure, and high temperature oxidation resistance of novel refractory high-entropy alloys," *J. Alloys Compd.*, vol. 624, pp. 270–278, 2015.

[78] Y. Y. Chen, U. T. Hong, J. W. Yeh, and H. C. Shih, "Selected corrosion behaviors of a Cu0.5NiAlCoCrFeSi bulk glassy alloy in 288 ℃ high-purity water," *Scr. Mater.*, vol. 54, no. 12, pp. 1997–2001, 2006.

[79] Y. Y. Chen, T. Duval, U. D. Hung, J. W. Yeh, and H. C. Shih, "Microstructure and electrochemical properties of high entropy alloys-a comparison with type-304 stainless steel," *Corros. Sci.*, vol. 47, no. 9, pp. 2257–2279, 2005.

[80] C. M. Lin and H. L. Tsai, “Evolution of microstructure, hardness, and corrosion properties of high-entropy Al0.5CoCrFeNi alloy,” *Intermetallics*, vol. 19, no. 3, pp. 288–294, 2011.

[81] Y. Qiu, M. A. Gibson, H. L. Fraser, and N. Birbilis, “Corrosion characteristics of high entropy alloys,” *Mater. Sci. Technol.*, vol. 31, no. 10, pp. 1235–1243, Jul. 2015.

[82] Zhiqi Yao, “Comparison of structures and properties of arc-melted and induction-melted high entropy alloys,” Tampere University of Technology, 2016.

[83] V.-T. Kuokkala, M. Apostol, and M. Hokka, “High and low temperature techniques in Hopkinson Split Bar testing,” *Implast 2010*, p. 9, 2010.

[84] G. Gray, “Classic Split-Hopkinson Pressure Bar Testing.,” *Mater. Park. OH ASM Int. 2000.*, vol. 8, pp. 462–476, 2000.

[85] Ahmad Mardoukhi, “High Temperature High Strain Rate Behavior of Superalloy MA Master ’ s thesis,” *Tampere Univ. Technol.*, no. March, 2013.

[86] A. S. Hamada and L. P. Karjalainen, “Nitric acid resistance of new type Fe-Mn-Al stainless steels,” *Can. Metall. Q.*, vol. Vol. 45, no. No.1, pp. 41–48, 2006.

[87] N. G. Jones, A. Frezza, and H. J. Stone, “Phase equilibria of an Al0.5CrFeCoNiCu high entropy alloy,” *Mater. Sci. Eng. A*, vol. 615, pp. 214–221, 2014.

[88] A. Takeuchi and A. Inoue, “Metallic Glasses By Atomic Size Difference, Heat of Mixing and Period of Constituent Elements and Its Application To Characterization of the Main Alloying Element,” *Mater. Trans.*, vol. 46, no. 12, pp. 2817–2829, 2005.

[89] M.-H. Tsai, K.-Y. Tsai, C.-W. Tsai, C. Lee, C.-C. Juan, and J.-W. Yeh, “Criterion for Sigma Phase Formation in Cr- and V-Containing High-Entropy Alloys,” *Mater. Res. Lett.*, vol. 1, no. May 2014, pp. 207–212, 2013.

[90] Y. X. Zhuang, W. J. Liu, Z. Y. Chen, H. D. Xue, and J. C. He, “Effect of elemental interaction on microstructure and mechanical properties of FeCoNiCuAl alloys,” *Mater. Sci. Eng. A*, vol. 556, pp. 395–399, 2012.

[91] Y. Dong, L. Jiang, H. Jiang, Y. Lu, T. Wang, and T. Li, “Effects of annealing treatment on microstructure and hardness of bulk AlCrFeNiMo0.2 eutectic high-entropy alloy,” *Mater. Des.*, vol. 82, pp. 91–97, 2015.